Computational and theoretical study of electron phase-space holes in kinetic plasma: kinematics, stability and ion coupling

by

Chuteng Zhou
Ingénieur diplômé, CentraleSupélec (2013)
M.Sc., Columbia University (2013)

Submitted to the Department of Nuclear Science and Engineering
in partial fulfillment of the requirements for the degree of
Doctor of Philosophy in Applied Plasma Physics
at the
MASSACHUSETTS INSTITUTE OF TECHNOLOGY
February 2018

Author .....
Department of Nuclear Science and Engineering
February 5, 2018

Certified by .....
Ian H. Hutchinson
Professor of Nuclear Science and Engineering
Thesis Supervisor

Certified by .....
Nuno F. Loureiro
Associate Professor of Nuclear Science and Engineering
Associate Professor of Physics
Thesis Reader

Accepted by .....
Ju Li
Battelle Energy Alliance Professor of Nuclear Science and Engineering
Professor of Materials Science and Engineering
Chairman, Department Committee on Graduate Theses

Computational and theoretical study of electron phase-space holes in kinetic plasma: kinematics, stability and ion coupling

by

Chuteng Zhou

Submitted to the Department of Nuclear Science and Engineering
on February 5, 2018, in partial fulfillment of the
requirements for the degree of
Doctor of Philosophy in Applied Plasma Physics

Abstract

In this thesis, a comprehensive study of Bernstein-Greene-Kruskal (BGK) mode electron holes in a collisionless plasma where strong kinetic effects are important is presented. Kinematic theory based on momentum conservation is derived treating the electron hole as a composite object to study the dynamics of electron holes. A novel 1-D Particle-In-Cell simulation code that can self-consistently track the electron hole motion has been developed for the purpose of this thesis work. Quantitative agreement is achieved between analytic theory and simulation observations. The thesis reports a new kind of instability for electron holes. Slow electron holes traveling slower than a few times the cold ion sound speed in the ion frame are observed to be unstable to the oscillatory velocity instability. A complete theoretical treatment for the instability is presented in this thesis. Numerical simulations yield quantitative agreement with the analytic theory in instability thresholds, frequencies and partially in instability growth rates. It is further shown that an electron hole can form a stable Coupled Hole Soliton (CHS) pair with an ion-acoustic soliton. A stable CHS travels slightly faster than the ion-acoustic velocity in the ion frame and is separated from a typical BGK mode electron hole in the velocity range by a gap, which is set by the oscillatory velocity instability. Transition between the two states is possible in both directions. A CHS exhibits a soliton-like behavior. The thesis sheds light on solving the ambiguity between an electron hole and a soliton. This thesis work also has important implications for interpreting space probes observations.

Thesis Supervisor: Ian H. Hutchinson
Title: Professor of Nuclear Science and Engineering

Thesis Reader: Nuno F. Loureiro
Title: Associate Professor of Nuclear Science and Engineering
Associate Professor of Physics

Acknowledgments

I remember reading the *PhD Grind* by Philip Guo before starting my PhD to prepare for this formidable journey. I thought to myself, what kind of grind will my PhD be? Now here I am, almost five years later, at the edge of finishing my PhD; when I look back, though there have been ups and downs, my overall experience as a PhD student at MIT has been quite enjoyable. I would like to acknowledge the people who have made my PhD experience a memorable intellectual journey.

First, I would like to acknowledge my research adviser Prof. Ian Hutchinson. Ian has always advised and guided me with his extensive knowledge, wisdom and sheer professionalism throughout my PhD. Ian is a great teacher, he approaches the PhD education as an "apprenticeship" (his own word). He provided valuable hands-on training while I was beginning my PhD and then gave me the freedom to perform my own research once I became independent enough. It is a pleasure to collaborate with Ian. He always reports his own progress at our weekly meeting, it is a boost to my own productivity as Ian is constantly challenging me with new ideas. Ian advises with humility, he treats me as an equal and always values what I have to say. Ian holds our scientific work to the highest standards and does not stand the slightest sloppiness. I feel extremely privileged to have Ian as my adviser and mentor during my PhD.

I would like to thank Chris Haakonsen. Chris was a senior PhD student in the group when I first joined. We worked together and shared office. Chris provided guidance and helped with many difficulties I encountered as a junior PhD student. His master-level computer science skills were extremely helpful. His work is the foundation of many results I accomplished in this thesis. Chris is a very sharp individual, I benefited a lot from our discussions about both work and life.

I would like to acknowledge the members of my thesis committee, Prof. Nuno Loureiro and Prof. Jeff Freidberg for the valuable advice on my research and continuous support during my PhD. I would like to acknowledge many other good teachers I have had at MIT, Prof. Anne White, Prof. Dennis Whyte, Prof. Miklos Porkolab, Dr. Paul Bonoli and Prof. Mehran Kardar for their exciting lectures and the key knowledge I received to carry

out my PhD work. I would like to acknowledge Dr. John Wright for his help with Loki and engaging computing clusters on which the thesis work is carried out. I would like to thank Brandon Savage and Lee Berkowitz for their help with IT problems. I would like to acknowledge Valerie Censabella, Jessica Coco, Brandy Baker, Heather Barry and Peter Brenton for the daily administrative support. I would like to acknowledge Dr. Marina Dang for helping me to improve my communication skills.

I would like to acknowledge teachers and supervisors I have had prior to MIT who got me interested in plasma physics: Prof. Mike Mauel, Dr. Özgür Gürcan, Prof. Francesco Volpe, Prof. Andrew Cole. I would like to thank Dr. David Malaspina for the helpful discussions and educating me about space physics.

I am grateful to the sponsors of my PhD and research work: Mr. Ray Rothrock through the Rothrock fellowship, US Department of Energy and National Science Foundation through Grant DE-SC0010491, National Aeronautics and Space Administration through Grant NNX16AG82G.

I would like to acknowledge Lulu Li, Will Boyd, Bob Mumgaard, Zach Hartwig, Ted Golfinopoulos, Ian Faust, John Walk, Mark Chilenski, Harold Barnard and Brandon Sorbom for their help and advice during my PhD. I would like to acknowledge the fellow graduate students at PSFC and NSE: Silvia Espinosa, Juan Ruiz Ruiz, Leigh Ann Kesler, Adam Kuang, Alex Tinguely, Alex Creely, Norman Cao, Libby Tolman, Sameer Abraham, Pablo Rodriguez-Fernandez, Haoran Xu, Xueying Lu, Pablo Ducru, Cong Su, Lun Yu, Yang Yang, Akira Sone, Xuejun Huang, Zhaoyuan Liu for being excellent peers and friends.

I would like to acknowledge other friends in the Boston area: Quntao Zhuang, Zheng Li, Jing Wang, Yinan Wang, Zhicheng Yang, Le Wang, Zhuoxuan Li, Hui Wang, Yongbin Sun, Ziwen Liu, Qingyang Wang, Ryan King, Chiwei Yan, Yiwen Zhu, Youzhi Liang, Ziqin Rong, Jiawei Zhou, Yue Guan, Yuxuan Ye, Qiao Zheng, Xiaofeng Yang, Lele Tang, Jieyu Chen, Tong Tong. Thank you so much for your friendship and support. I would like to acknowledge my friends from high school: Cheng Xu, Shihan Tao and Shangjun Zhang for being good friends to me for such a long time and all the happy time and help

you've given me during my PhD at MIT.

J'aimerais remercier M. Jean Aristide Cavaillès, M. Hervé Riou pour me donner un goût pour les sciences physiques. J'aimerais remercier M. Gil Guibert et M. Michel Cognet pour m'enseigner comment penser en mathématiques et les techniques qui m'ont beaucoup servi pendant ma thèse. J'aimerais remercier spécialement Bruno et Pascale Seznec pour leur amitié et encouragement.

I would like to thank my girlfriend Jiahua for her love and support that is most dear to my heart. I am deeply indebted to my parents for their love and care thoughout my entire life. They have always supported my choice and encouraged me to pursue my dreams. 负笈离家十数载, 父母养育恩难忘.

Contents

List of Figures

Nomenclature

ϵ_0	Vacuum permittivity
μ_0	Vacuum permeability
ω_b	Bounce frequency of deeply trapped electrons: $\sqrt{e\psi/m_e}/L$
Ω_e	Electron cyclotron frequency: $\sqrt{\frac{eB}{m_e}}$
ω_{pe}	Electron plasma frequency: $\sqrt{\frac{ne^2}{\epsilon_0 m_e}}$
ϕ	Electrostatic potential
ψ	The maximum of ϕ
$\tilde{\phi}$	Normalized electrostatic potential: ϕ/ψ
c	Speed of light in vacuum
c_s	Cold ion sound speed: $\sqrt{\frac{T_e}{m_i}}$
h	Planck constant
L	Spatial dimension of an electron hole parallel to the magnetic field direction
M	Mach number of a velocity normalized to c_s
N	Number of particles
T	Temperature in electron-volt

U Electron hole velocity in the plasma or the ion frame

V Volume

$v_{\mathrm{th,e}}$ Electron thermal speed: $\sqrt{\frac{T_e}{m_e}}$

$v_{\mathrm{th,i}}$ Ion thermal speed: $\sqrt{\frac{T_i}{m_i}}$

v_h Electron hole velocity in the rest frame of background electrons

$v_{d,e}$ Drift velocity of bulk electrons in the ion frame

$v_{p,e}$ Marginal passing velocity for electrons: $\sqrt{\frac{e\psi}{m_e}}$

$v_{p,i}$ Marginal passing velocity for ions: $\sqrt{\frac{e\psi}{m_i}}$

Chapter 1

Background

Plasma is the ionized matter that makes up more than 99% [1] of the visible matter in our universe. Understanding plasma is thus crucial for the understanding of our universe. Plasma physics is the branch of physics that studies this particular state of matter. Research in plasma physics is also driven by the numerous industrial applications. To name a few, the entire modern semiconductor industry is made possible by high precision plasma etching tools [2]. Plasma is also widely used in surface treatment [3] and industrial pollution control [4]. Plasma technology based ion thrusters provide a much higher specific impulse alternative to the traditional chemical rockets [5], potentially powering spacecrafts for deep space travel. Plasma wake-field acceleration [6] is expected to create highly-efficient compact particle accelerator in the future. The most sought-after application of plasma physics is nuclear fusion [7], the holy grail of all forms of energy. The extreme physical conditions required by nuclear fusion necessarily demands dealing with matter in form of plasma. Despite great scientific and technological hurdles, mankind has been pursuing controlled nuclear fusion relentlessly for decades. The enormous amount of resources put into fusion research greatly advanced the state of plasma physics in the last decades.

The Sun is the fusion reactor at the center of the Solar System. Fusion energy from the Sun radiates out both in form of electromagnetic radiations and particle fluxes [1]. The extremely hot particles coming out of the solar atmosphere are in form of plasma and

are known as solar wind [1]. The solar wind is blown out into the entire Solar System, forming a giant plasma bubble known as the heliosphere [1]. Near Earth, the dynamics of plasma is strongly controlled by Earth's magnetic field. This region of space is known as Earth's magnetosphere [1]. Earth's magnetosphere is partially responsible for blocking highly energetic harmful cosmic rays [8] from reaching the surface of Earth. Closer to Earth, the upper Earth atmosphere is ionized by radiation and forms the inner edge of the magnetosphere. This plasma layer is known as ionosphere [9]. The ionosphere is very important for telecommunication on Earth as it influences the propagation of electromagnetic waves [9]. Most man-made satellites travel in the magnetosphere, ionosphere or the heliosphere. The study of these plasma bodies near Earth and in the Solar System is a particular branch of physics known as space physics [1]. In addition to better understanding space environment, space physics is particularly important for the operation of satellites and manned flight in space [10]. Many spacecraft have been launched in the last few decades to provide in situ measurements for space physics research. This thesis is at the intersection of plasma physics and space physics.

I Modeling plasma dynamics: kinetic equations

A plasma consists of charged particles. The force felt by a charged particle traveling in the electromagnetic field is the Lorentz force

$$\mathbf{F} = q\left(\mathbf{E} + \mathbf{v} \times \mathbf{B}\right). \tag{1.1}$$

We adopt SI units throughout this thesis. When the particle velocity is much slower than the speed of light and the inter-particle distance is much bigger than the thermal de Broglie wavelength, namely,

$$v \ll c\,,\ \frac{h}{\sqrt{2\pi m T}} \ll \left(\frac{V}{N}\right)^{\frac{1}{3}}, \tag{1.2}$$

the plasma is in the classical limit where relativistic and quantum mechanics effects are negligible [11]. The plasma bodies studied in space physics are mostly in this classical limit [11]. A classical plasma can be described by solving simultaneously Newton's equations of motion and Maxwell's equations for the electromagnetic field. A plasma is a collection of particles interacting with one another through self-consistent electromagnetic interactions, the density of a plasma ranges from for example 10^6 particles per cubic meter in solar wind to 10^{21} particles per cubic meter in a fusion reactor and higher still within stars [7]. In principle, the equations of motion are solved for each particle simultaneously while the Maxwell's equation takes into account more macroscopic quantities such as charge and current density. A mathematical way to describe this particle ensemble needs to be introduced to make the problem more tractable. A complete description of a plasma can be specified given the coordinate $\mathbf{x}_i(t)$ and velocity $\mathbf{v}_i(t)$ of each particle i of species α. We define a function F

$$F_\alpha(\mathbf{x}, \mathbf{v}, t) = \sum_{i=1}^{N_\alpha} \delta(\mathbf{x} - \mathbf{x}_i)\delta(\mathbf{v} - \mathbf{v}_i), \tag{1.3}$$

where subscript α designates particle species. We can thus write down the charge density and current density in the following forms

$$\rho = \sum_\alpha q_\alpha \int F_\alpha(\mathbf{x}, \mathbf{v}, t)\, d\mathbf{v}, \tag{1.4}$$

$$j = \sum_\alpha q_\alpha \int \mathbf{v} F_\alpha(\mathbf{x}, \mathbf{v}, t)\, d\mathbf{v}. \tag{1.5}$$

The electric and magnetic fields due to the plasma particles are given by

$$\nabla \cdot \mathbf{E} = \frac{\sum_{\alpha} q_\alpha \int F_\alpha(\mathbf{x}, \mathbf{v}, t)\, d\mathbf{v}}{\epsilon_0}, \tag{1.6}$$

$$\nabla \cdot \mathbf{B} = 0, \tag{1.7}$$

$$\nabla \times \mathbf{E} = -\frac{\partial \mathbf{B}}{\partial t}, \tag{1.8}$$

$$\nabla \times \mathbf{B} = \mu_0 (\sum_{\alpha} q_\alpha \int \mathbf{v} F_\alpha(\mathbf{x}, \mathbf{v}, t)\, d\mathbf{v} + \epsilon_0 \frac{\partial \mathbf{E}}{\partial t}). \tag{1.9}$$

From the equation of motion and the conservation of particles, we get an equation that governs the evolution of $F_\alpha(\mathbf{x}, \mathbf{v}, t)$

$$\frac{\partial F_\alpha(\mathbf{x}, \mathbf{v}, t)}{\partial t} + \mathbf{v} \cdot \frac{\partial F_\alpha(\mathbf{x}, \mathbf{v}, t)}{\partial \mathbf{x}} + \frac{q_\alpha}{m_\alpha} (\mathbf{E} + \mathbf{v} \times \mathbf{B}) \cdot \frac{\partial F_\alpha(\mathbf{x}, \mathbf{v}, t)}{\partial \mathbf{v}} = 0. \tag{1.10}$$

Equation (1.10) is the Klimontovich-Dupree equation [12] of plasma dynamics. However, it is not particularly useful as $F_\alpha(\mathbf{x}, \mathbf{v}, t)$ is composed of Dirac delta functions, which are distributions in the strict mathematical sense instead of being a classically differentiable statistical function. The common way to remedy this is to introduce a differentiable and non-negative phase-space probability function $\rho_{\alpha,N}(\mathbf{x}_1, ..., \mathbf{x}_N; \mathbf{v}_1, ..., \mathbf{v}_N, t)$ defined as the density of probability at a time t to find particles of species α to have coordinates and velocities of the values $\mathbf{x}_1, \mathbf{x}_2, ..., \mathbf{x}_N; \mathbf{v}_1, \mathbf{v}_2, ..., \mathbf{v}_N$. $\rho_{\alpha,N}$ is a probability density so its integral over the entire $6N$-dimensional phase space is 1. The total amount of information contained in this $6N$-dimensional phase space is much more than what we need to describe the bulk properties of a plasma and $\rho_{\alpha,N}$ as a function of $6N + 1$ arguments is difficult to deal with. We need to simplify this problem even more at the expense of losing some unimportant detailed information. We introduce a one particle density function $f_{\alpha,1}$ given by

$$\begin{aligned} f_{\alpha,1}(\mathbf{x}, \mathbf{v}, t) &= \langle F_\alpha(\mathbf{x}, \mathbf{v}, t) \rangle \\ &= N_\alpha \int \rho_{\alpha,N}(\mathbf{x}_1 = \mathbf{x}, \mathbf{x}_2, ..., \mathbf{x}_N; \mathbf{v}_1 = \mathbf{v}, \mathbf{v}_2, ..., \mathbf{v}_N, t)\, d\mathbf{x}_2 ... d\mathbf{x}_N d\mathbf{v}_2 ... d\mathbf{v}_N. \end{aligned} \tag{1.11}$$

$f_{\alpha,1}(\mathbf{x}, \mathbf{v}, t)$ represents the expectation value of finding any of the N particles of species α at coordinate $\mathbf{x}$ and velocity $\mathbf{v}$. We have assumed that the probability density function is symmetric with respect to permuting the particles. In a similar way, we can define the general s-particle density function $f_{\alpha,s}$ as the follow

$$f_{\alpha,s}(\mathbf{x}_1, \mathbf{v}_1, ..., \mathbf{x}_s, \mathbf{v}_s, t) = \frac{N!}{(N-s)!} \int \prod_{i=s+1}^{N} d\mathbf{x}_i d\mathbf{v}_i \, \rho_{\alpha,N}. \tag{1.12}$$

By averaging the Klimontovich-Dupree equation using the probability density function, one can transform [12] the original equation (1.10) into an infinite chain of statistical equations involving the s-particle density functions $f_{\alpha,s}$ defined above, with $f_{\alpha,s}$ being involved in the equation of $f_{\alpha,s-1}$. It is very difficult to solve this infinite chain of equations. However, it is possible to take advantage of the statistical property of the system to terminate the chain at the first few orders and give an approximation for the higher order terms. In a plasma, the small parameter is often chosen as $g = 1/n\lambda_{\mathrm{De}}^3 \ll 1$, the inverse of the number of particles in the Debye sphere. Debye length $\lambda_{\mathrm{De}} = \sqrt{\epsilon_0 T/nq^2}$ is the characteristic electric field shielding distance in a plasma. A plasma satisfying this property is said to be *weakly-coupled* or *ideal*. The plasma studied in space physics and the fusion plasma are typically ideal plasma with $g < 10^{-5}$. It can be proved in this case that each hierarchy of statistical equation is of order $\mathcal{O}(g)$ smaller than the previous one [12, 13]. To the lowest order, the kinetic equation for the plasma can be written as

$$\left(\frac{\partial}{\partial t} + \mathbf{v} \cdot \nabla_{\mathbf{x}} + \frac{q_\alpha}{m_\alpha} (\mathbf{E} + \mathbf{v} \times \mathbf{B}) \cdot \nabla_{\mathbf{v}} \right) f_\alpha(\mathbf{x}, \mathbf{v}, t) = 0, \tag{1.13}$$

where we have used interchangeably $f_\alpha(\mathbf{x}, \mathbf{v}, t)$ and $f_{\alpha,1}(\mathbf{x}, \mathbf{v}, t)$ to simplify the notation. Equation (1.13) is called the *Vlasov equation* or the *collisionless Boltzmann equation*. Coupled with Maxwell's equations, it describes the behavior of the plasma on a time scale shorter than the typical collision time scale: $\tau_{\mathrm{collective}} \ll \tau_{\mathrm{collision}}$. The Vlasov equation coupled with Maxwell's equations give a complete description of a plasma in the collisionless

regime:

$$\begin{cases} \left(\dfrac{\partial}{\partial t} + \mathbf{v}\cdot\nabla_{\mathbf{x}} + \dfrac{q_\alpha}{m_\alpha}(\mathbf{E}+\mathbf{v}\times\mathbf{B})\cdot\nabla_{\mathbf{v}}\right) f_\alpha(\mathbf{x},\mathbf{v},t) = 0, \\ \nabla\cdot\mathbf{E} = \dfrac{\displaystyle\sum_\alpha q_\alpha \int f_\alpha(\mathbf{x},\mathbf{v},t)\,d\mathbf{v}}{\epsilon_0}, \\ \nabla\cdot\mathbf{B} = 0, \\ \nabla\times\mathbf{E} = -\dfrac{\partial\mathbf{B}}{\partial t}, \\ \nabla\times\mathbf{B} = \mu_0(\displaystyle\sum_\alpha q_\alpha \int \mathbf{v} f_\alpha(\mathbf{x},\mathbf{v},t)\,d\mathbf{v} + \epsilon_0\frac{\partial\mathbf{E}}{\partial t}). \end{cases} \tag{1.14}$$

This approximation corresponds to the mean field approach in statistical mechanics [13], modeling plasma particle dynamics with self-consistent long-range electromagnetic interactions. It is well-adapted for the dilute plasma studied in space physics. The mean free path for both the electrons and the ions are bigger than the Earth radius in the magnetosphere [1]. We are in a highly collisionless regime for the kind of plasma phenomenon we are going to introduce in the next section. The collisional corrections appearing in the higher order kinetic equations are often lumped into a single collision operator $C(f_\alpha, f_\alpha)$ to be placed at the right hand side of Equation (1.13) instead of 0. This hierarchy of kinetic equations is called the *BBGKY hierarchy* [13], named after Bogolyubov, Born, Green, Kirkwood and Yvon. For the purpose of this thesis, we are going to focus on the collisionless mean field model.

The equation system (1.14) can be further simplified for an electrostatic plasma. This approximation gives rise to an equation system called the *Vlasov-Poisson system*

$$\begin{cases} \left(\dfrac{\partial}{\partial t} + \mathbf{v}\cdot\nabla_{\mathbf{x}} - \dfrac{q_\alpha}{m_\alpha}\nabla\phi\cdot\nabla_{\mathbf{v}}\right) f_\alpha(\mathbf{x},\mathbf{v},t) = 0, \\ \nabla^2\phi + \dfrac{\displaystyle\sum_\alpha q_\alpha \int f_\alpha(\mathbf{x},\mathbf{v},t)\,d\mathbf{v}}{\epsilon_0} = 0. \end{cases} \tag{1.15}$$

This is the most simplified kinetic model of a plasma, valid when the interaction between plasma particles is mainly the Coulomb interaction with the electrostatic potential ϕ.

This collisionless model of the plasma offers very rich physics and is of fundamental importance not only in plasma physics but also in other fields such as galactic dynamics. The mathematical similarity of the gravitational field to the electrostatic field leads to an almost identical set of equations for the evolution of mass distribution in galaxies under gravitational interaction [14]. Understanding the quantitative behavior of the Vlasov-Poisson system turns out to be challenging. Arguable the most important feature of such a system is *Landau damping*, the physical mechanism first predicted by physicist Lev Landau [15, 16] through which a wave is damped in such a collisionless system. It was later confirmed in the experiment by Malmberg and Wharton [17]. Entropy is conserved in a Vlasov plasma. The information about the Landau-damped wave does not go away and is stored at a much finer scale in the particle distribution function. The damped wave can be "resurrected" using a well-calculated second excitation. This phenomenon is called the *plasma echo* [18]. The study of Vlasov-Poisson system is also a frontier research topic in Mathematics and Mathematical Physics. The Fields Medal-winning proof of Landau damping in the fully nonlinear perturbative regime given by Villani and Mouhot [19] is a recent breakthrough in this field.

The more macroscopic properties of the plasma can be obtained by taking the moments of the kinetic equations and perform a fluid closure [20]. For example, the macroscopic continuity equation is obtained by taking the zeroth order moment and the macroscopic momentum conservation equation is obtained taking the first order moment. The quantities

$$n_\alpha = \int f_\alpha \, d^3\mathbf{v}, \tag{1.16}$$

$$\mathbf{V} = \frac{1}{n_\alpha} \int \mathbf{v} f_\alpha \, d^3\mathbf{v}, \tag{1.17}$$

are fluid density and flow velocity.

II Computer simulation tools for kinetic plasma

The understanding of plasma physics has been greatly advanced by the use of modern computers. The exponentially growing computing power offers an unprecedented way to study plasma dynamics via computer simulation. This is particularly important for plasma kinetics as the analytic theory is often intractable. This thesis work relies heavily on computing tools to study phenomena in kinetic plasma. In this section, we are going to survey two major computer simulation schemes for a kinetic plasma.

II.1 Vlasov code

We have established in the last section that the collisionless behavior of a plasma is governed by the Vlasov equation. A Vlasov code solves the Vlasov equation by direct numerical integration and treats the phase space as a continuum. The Vlasov equation is a continuity equation. It can be solved by the method of characteristics. The Vlasov equation states that the distribution function f is constant on the characteristics which are the particle orbits

$$\frac{d\mathbf{x}}{dt} = \mathbf{v} \ , \ \frac{d\mathbf{v}}{dt} = \frac{q}{m} \left(\mathbf{E} + \mathbf{v} \times \mathbf{B} \right) . \tag{1.18}$$

The constancy of the distribution function on the orbits implies for a time step Δt that:

$$f(\mathbf{x} + \mathbf{v}\Delta t, \mathbf{v} + \frac{q}{m} \left(\mathbf{E} + \mathbf{v} \times \mathbf{B} \right) \Delta t, t + \Delta t) = f(\mathbf{x}, \mathbf{v}, t). \tag{1.19}$$

From this point, it may seem obvious that the Vlasov system can be solved numerically by following a phase-space fluid parcel and solving self-consistently for the fields. However, the entropy-conserving nature of the Vlasov equation dictates that large scale perturbations will result in finer and finer filamentation of the distribution function in phase-space, eventually causing strong phase-space gradients and numerical instabilities. To overcome this difficulty, a semi-Lagrangian scheme [21] is used where the time-advanced distribution function f is projected onto the neighboring Euler-grid points in both space and velocity.

Time splitting is also used to split the Vlasov equation into two advection equations to make the numerical scheme more efficient. In the one-dimensional electrostatic case, this time splitting scheme can be written as [21]

$$f^*(x,v) = f^n(x - v\Delta t/2, v), \tag{1.20}$$

$$f^{**}(x,v) = f^*(x, v + qE(x)\Delta t/m), \tag{1.21}$$

$$f^{n+1}(x,v) = f^{**}(x - v\Delta t/2, v). \tag{1.22}$$

This time splitting method is a special case of Strang splitting [22]. Fourier filtering or artificial dissipation is often applied to the distribution function f to remove the phase-space filamentation wrinkles from the simulation [23]. This procedure, necessary for the numerical stability of the simulation, introduces numerical dissipation and needs to be implemented carefully not to sacrifice the nonlinear physics.

II.2 Particle-In-Cell (PIC) code

Another popular numerical scheme to simulate kinetic plasma is the Particle-In-Cell (PIC) code [24]. Particle-In-Cell simulation solves the equivalent Klimontovich-Dupree problem with random macroparticles. Typically in a PIC simulation, we solve the first-principles equation of motion for a large number of computing particles indexed from 1 to N

$$\frac{d\mathbf{x}_i}{dt} = \mathbf{v}_i\,,\ \frac{d\mathbf{v}_i}{dt} = \frac{q}{m}(\mathbf{E}(\mathbf{x}_i) + \mathbf{v}_i \times \mathbf{B}(\mathbf{x}_i))\,, 1 \le i \le N. \tag{1.23}$$

However, it is difficult to perform the calculations of the position and the velocity simultaneously to the required accuracy as they are interdependent. The most common numerical method to integrate such a system in the electrostatic regime is the *leap-frog algorithm* [24], where the position and the velocity are integrated separately with half a time-step offset. The schematic of such an algorithm is shown in Figure 1-1. The advantage of such an algorithm is that each integration is done centered in time. A leapfrog scheme is of second order accuracy.

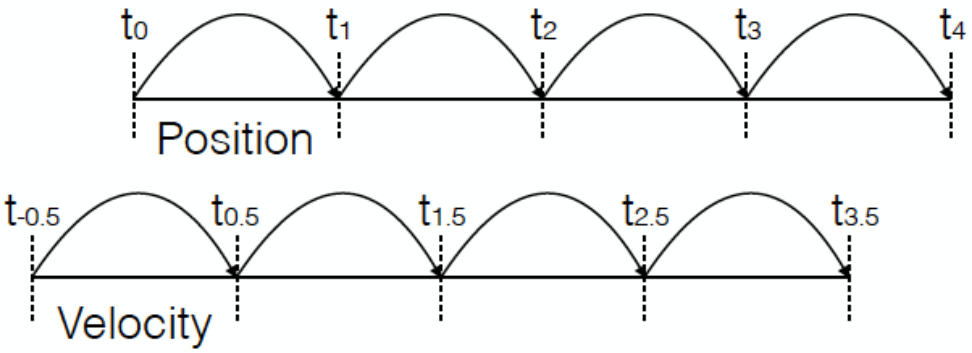

Figure 1-1: Schematic of the leapfrog algorithm.

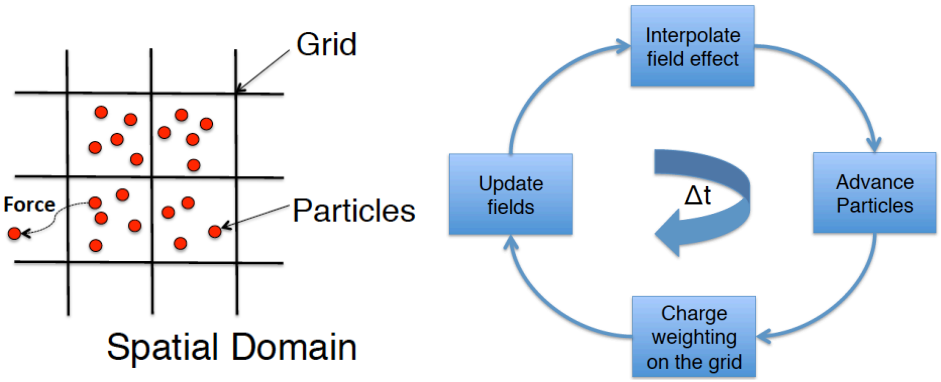

Figure 1-2: Left: Computing particles with spatial "cells" in PIC.
Right: the processes involved in advancing one time step in PIC.

Electric and magnetic fields need to be solved self-consistently while advancing the particles. In a PIC simulation, the fields are solved on a spatial grid. The spatial grid forms the "cells" in which plasma particles reside. The charge and current carried by the plasma particles are interpolated onto the neighboring grid points for solving the fields. These processes and the associated flow chart are shown in Figure 1-2. Because their influence on one another is conveyed by the grid, the computing particles used in PIC simulation are effectively of *finite-size*. Instead of being a point charge, they are more like grid-spacing-sized charged rigid clouds that can move through each other. Hence the particle weighting onto the grid points needs to take into account the finite particle size. A very common particle weighting used in PIC is the *cloud-in-cell* model. In a cloud-in-cell scheme, if a macroparticle i has position x_i, charge q_c and its nearest grid points are X_j

and X_{j+1}, the grid assignment for a cloud-in-cell model in 1-D can be written as

$$q_j = q_c \frac{X_{j+1} - x_i}{\Delta x}, \tag{1.24}$$

$$q_{j+1} = q_c \frac{x_i - X_j}{\Delta x}. \tag{1.25}$$

This weighting produces a triangular particle shape of width $2\Delta x$. The fields are solved on the grid. In the electrostatic case, Poisson's equation can be solved using a standard finite difference scheme. The force weighting on the particles can then be done in a similar way as the charge weighting. As the computing particle moves though the grid, it contributes to density more smoothly than a point charge. This is a crucial point for PIC simulation. In a weakly-coupled plasma, the electric field of a single particle is electrically screened by the presence of many other particles, this phenomenon is called *Debye shielding*. It can be shown [24] that the finite particle size leads to Debye shielding effect so that we can simulate a plasma with much fewer particles than the actual number. One computing particle represents a large number of physical particles and has the same charge-to-mass ratio as a physical particle. The task becomes immediately more manageable as we have seen that the typical number of particles per Debye sphere in the plasma we are interested in is $10^5 - 10^8$. From a Monte-Carlo viewpoint, the computing particles can be regarded as Lagrangian markers embedded randomly in the Vlasov phase-space fluid, interacting through the self-consistent fields. The use of random particles is an efficient way to sample the Vlasov phase-space fluid. Despite the smoothing effect associated with finite particle size, there is still statistical noise associated with particles moving from one cell to the next. If there are N_c particles per cell on average in a PIC simulation, then the variance in the particle number count is given by the counting statistics to be $1/\sqrt{N_c}$. Other things being equal, this noise level can be reduced by using more computing particles. The noise problem plagued the earliest PIC simulations. Limited by available computing power, the earliest PIC practitioners had to settle for rather noisy simulations, which made the quantitative study of some plasma phenomena difficult. This problem has been alleviated by today's more powerful modern computers.

PIC simulation, like other numerical schemes, is susceptible to numerical instabilities. The grid size Δx and the time step Δt need to be chosen to ensure numerical stability. Typically, Δx must not exceed several times the Debye length and Δt needs to be smaller than electron plasma period: $\Delta t < \omega_{pe}^{-1}$. While simulating electromagnetic plasma, the time step also needs to satisfy the Courant-Friedrichs-Lewy condition [24]:

$$\Delta t \leq \Delta x / c, \tag{1.26}$$

where c is the speed of light.

While simulating a kinetic plasma, it is crucial to choose a simulation method that is the most suitable for the problem. Both the Vlasov and the PIC simulations have their advantages and drawbacks. It is important to know their boundaries. Choosing and implementing the right simulation tool is essential to success.

III BGK mode electron holes

In the seminal paper published by Bernstein, Greene and Kruskal [25], the authors described a family of exact nonlinear stationary solutions of the Vlasov-Poisson plasma. In the rest frame of the stationary solution, the particle distribution is a function of the total particle energy. The authors showed by manipulating the particle distribution on the orbits trapped in potential energy troughs, that essentially arbitrary exact nonlinear solutions can be constructed. These nonlinear solutions are commonly called *BGK modes*. There are many different kinds of BGK modes, ranging from solitary solutions to periodic solutions. The most commonly studied ones are electron holes, ion holes and double layers [26]. In this thesis, we are going to focus on electron holes. An electron hole is a localized density deficit of electrons. The positive charge gives rise to a solitary positive potential pulse that in turn traps electrons. This self-consistent trapping is made possible by the reduced phase-space density on trapped electron orbits. An electron hole can be regarded as an electron phase-space vortex. It is coherent and not intermittent by nature.

It is commonly thought that in nature, electron holes are generated by kinetic plasma

instabilities, which are also called micro-instabilities. Essentially, any plasma distribution satisfying the Penrose instability criterion is unstable to electrostatic perturbations. Penrose instability criterion [12] states that for a combined plasma distribution $F_0 = f_e + \frac{m_e}{m_i} f_i$, if F_0 has one local minimum at u_0, then the plasma is unstable to electrostatic perturbations if and only if

$$\text{P.V.} \int_{-\infty}^{+\infty} \frac{F(u_0) - F(u)}{(u_0 - u)^2}\, du < 0, \tag{1.27}$$

where we took the Cauchy principal value of the integral. Two stream and bump-on-tail instabilities can be considered as special cases of Penrose-unstable distribution functions. During the nonlinear saturation stage of the instability in 1-D, electron holes form as a result of strong particle trapping. Such an example is shown in Figure 1-3 for a two stream instability simulation using a one-dimensional PIC code. In addition to the kinetic instabilities, electron holes can also form at the nonlinear stage of Landau damping [27] and by chirped autoresonance [28] in a plasma.

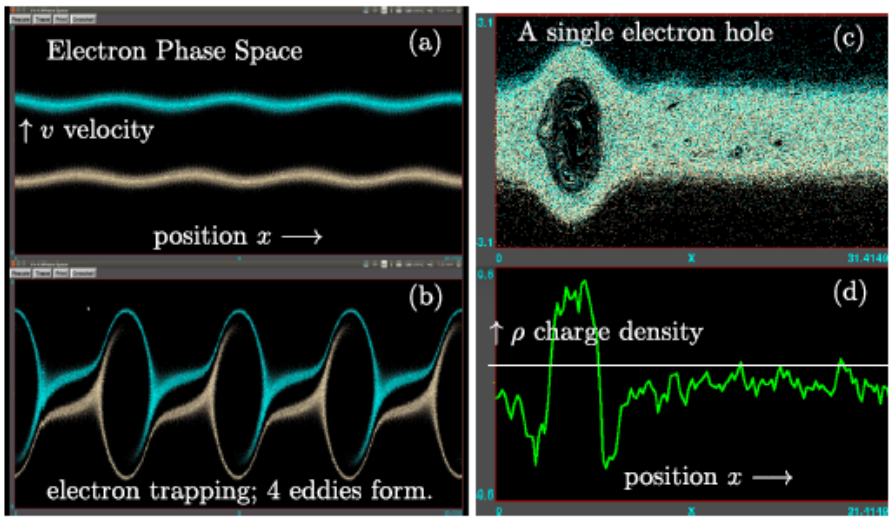

Figure 1-3: (a) Counter propagating electron beams unstable to two stream instability (b) Formation of phase space vortices due to particle trapping (c) A single electron hole in phase space after coalescence (d) Charge density associated with the electron hole. Plot adapted from reference [29], courtesy of I. H. Hutchinson

Electron holes are not only an object of theoretical interest. The study of these nonlinear structures in plasma gained increasing interest after space probe measurements

confirmed their wide-spread existence in the Earth's auroral zone [30], magnetosphere [31] and in the solar wind [32]. They are implicated in magnetic reconnection [33], electron acceleration [34], collisionless shocks [35] and other important plasma dynamics in space. Electron holes are also detected in the laboratory plasma during magnetic reconnection [36] and beam injection [37]. We are going to discuss more in Subsection III.3 about observational evidence.

In the next subsection, we are going to show how an electron hole solution is constructed in a one-dimensional Vlasov-Poisson plasma.

III.1 Integral equation approach

To construct an electron hole solution, we need to start from the basic Vlasov equation. Suppose that a stationary solution is moving with a velocity v_h in the background electron rest frame. In the rest frame of the moving solution, the electron orbits are constant energy contours with energy $\mathcal{E}$ defined as $\mathcal{E} = \frac{1}{2}m_e v^2 - e\phi(x)$. An orbit is said to be *trapped* if $\mathcal{E} < 0$. The Vlasov equation says that distribution function is constant on particle orbits; f is thus a function of $\mathcal{E}$. For the purpose of introduction, we take the ions to be a fixed neutralizing background of density $n_{i\infty}$, Poisson's equation then gives

$$\frac{d^2\phi}{dx^2} = e(n_e - n_{i\infty})/\epsilon_0. \tag{1.28}$$

If we specify the shape of stationary potential profile $\phi(x)$, then the electron density profile $n_e(\phi)$ can be obtained by taking its second derivative $d^2\phi/dx^2$. Taking $\phi(x)$ to be a solitary and half-monotonic (meaning monotonic from its center to infinity) function, the passing electron orbits are determined everywhere. If we further suppose that the electron distribution is known at infinity as $f_{\infty,e}$, then the contribution from passing electrons $n_p(\phi)$ to the total electron density can be expressed as

$$n_p(\phi) = \int_{-\infty}^{+\infty} \frac{v}{\sqrt{v^2 + 2e\phi/m_e}} f_{\infty,e}(v + v_h)\, dv, \tag{1.29}$$

where we have used the constancy of distribution function on a particle orbit. We need the trapped electron distribution to match

$$n_t(\phi) = \int_{-\sqrt{2e\phi/m_e}}^{+\sqrt{2e\phi/m_e}} f_t(v)\, dv = 2\int_{-e\phi}^{0} f(\mathcal{E})\, \frac{d\mathcal{E}}{\sqrt{2m_e(\mathcal{E}+e\phi)}}, \tag{1.30}$$

where $\pm\sqrt{2e\phi/m_e}$ are the velocities of marginally trapped electrons. Knowing $n_t(\phi) = n_e(\phi) - n_p(\phi)$, this integral can be inverted using the Abel transform [38] to find $f(\mathcal{E})$ for $\mathcal{E} < 0$. This final step gives the particle distribution in the trapped region:

$$f(\mathcal{E}) = \int_{0}^{-\mathcal{E}} \frac{1}{\sqrt{2}\pi} \frac{dn_t}{d\phi} \frac{d\phi}{\sqrt{(-\mathcal{E}-e\phi)/m_e}}, \tag{1.31}$$

A schematic of an electron hole is shown in Figure 1-4. A given potential $\phi(x)$ and the background distribution completely determines the values of f on the trapped orbits, which are shaded in the plot.

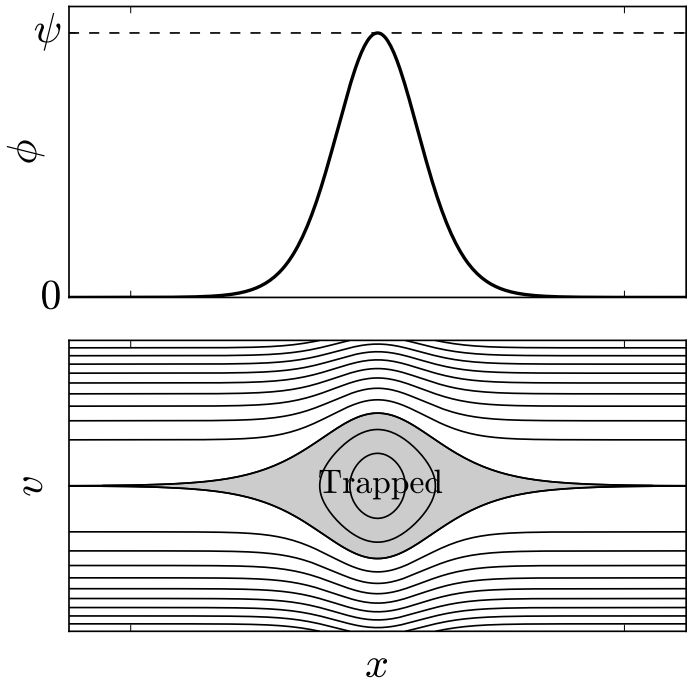

Figure 1-4: Top: electrostatic potential $\phi(x)$ of an electron hole. Bottom: electron phase space orbits, the shaded orbits are trapped.

III.2 Differential equation approach

The alternative way to the above method is the differential equation approach. It is also called the Sagdeev potential [39] approach. Starting with Poisson's equation for a charge density $\rho(\phi)$, we multiply both sides of Poisson's equation by $d\phi/dx$:

$$-\frac{d\phi}{dx}\frac{d^2\phi}{dx^2} = \frac{d\phi}{dx}\frac{\rho}{\epsilon_0}. \tag{1.32}$$

Notice that the left hand side of the equation can be readily written as a total derivative with respect to x. We integrate the equation to give

$$-\frac{1}{2}\epsilon_0\left(\frac{d\phi}{dx}\right)^2 = \int_0^\phi \rho(\tilde{\phi})\, d\tilde{\phi}. \tag{1.33}$$

ϕ is a solitary solution, which means both ϕ and its derivatives vanish at infinity: $d\phi/dx = 0$ at $\phi = 0$. We have used this relation in the integration to get Equation 1.33. The right hand side of Equation 1.33 is called a Sagdeev or classical potential and is often denoted by $V(\phi)$

$$V(\phi) = \int_0^\phi \rho(\tilde{\phi})\, d\tilde{\phi}. \tag{1.34}$$

The potential ϕ can be thought of as the position of a particle moving in the potential $V(\phi)$, with x playing the role of time. For a proper solitary solution to exist, $V(\phi) = 0$ has two solutions, one at $\phi = 0$ and the other at $\phi = \psi$, where ψ is the maximum of hole potential ϕ. The differential equation approach consists of specifying the particle distribution f and thus $\rho(\phi)$. $\rho(\phi)$ is then integrated to get $V(\phi)$. $V(\phi)$ can be used to calculate the potential $\phi(x)$ recognizing that Equation (1.33) gives $d\phi/dx = \pm\sqrt{-2V(\phi)/\epsilon_0}$. Therefore we have

$$x(\phi) = \int_\phi^\psi \frac{d\tilde{\phi}}{\sqrt{-2V(\tilde{\phi})/\epsilon_0}}. \tag{1.35}$$

This formula is valid for positive x, $\phi(x)$ for negative x is obtained by mirror symmetry $\phi(-x) = \phi(x)$.

Thus we have obtained $\phi(x)$. However, the separatrix imposed by ϕ may not align with

that of f we start with. A self-consistency equation needs to be solved that relates different model parameters. This consistency equation can be solved numerically by iterations or algebraically in some simple cases. Schamel [40] introduced a parametric hole model that is particularly influential, it consists of considering a Maxwell-Boltzmann distribution for the trapped species

$$f_e(x,v) = \begin{cases} f_{\infty,\mathrm{e}}(0)\exp\left[-\dfrac{m_e(\sigma\sqrt{2\mathcal{E}/m_e}+v_h)^2}{2T_e}\right] & \text{if } \mathcal{E}>0 \\ f_{\infty,\mathrm{e}}(0)\exp(-\dfrac{v_h^2}{2v_{\mathrm{th,e}}^2})\exp(-\dfrac{\beta\mathcal{E}}{T_e}) & \text{if } \mathcal{E}<0 \end{cases}. \tag{1.36}$$

Here σ is the sign of velocity v, v_h is the electron hole velocity in the rest frame of background electrons, β is the particle trapping parameter and $v_{\mathrm{th,e}} = \sqrt{T_e/m_e}$. A negative β gives a "hole" in the trapped region of electron phase space. In Figure 1-5,

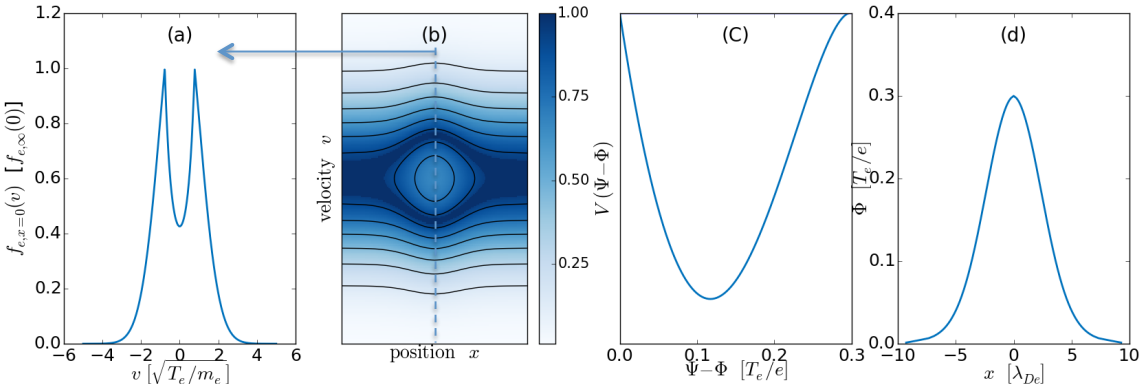

Figure 1-5: (a) Electron velocity distribution at the hole center (b) Electron phase-space density assuming a Maxwellian background plasma (c) Sagdeev potential V as a function of $\psi-\phi$ (d) Electrostatic potential profile of the solitary electron hole

we give an example solution of a Maxwell-Boltzmann or Schamel electron hole solved by iteration with the differential approach. The method first specifies the distribution function on axis (panel a), then $\rho(\phi)$ is known by constancy of f on constant energy contours, the Sagdeev potential is computed to determine ψ (panel c). These steps are iterated until a self-consistent solution is found. Finally, the electrostatic potential ϕ (panel d) can be determined from Equation (1.35) by computing the inverse of $x(\phi)$.

The condition for the existence of a solitary solution requires the Sagdeev potential V to be zero at $\phi = \psi$:

$$V(\psi; v_h, \beta) = 0. \tag{1.37}$$

This condition relates the wave velocity to its amplitude and is often referred to as the *nonlinear dispersion relation* [40]. Schamel [40] derived an algebraic form of the nonlinear dispersion relation for shallow holes $\psi \ll T_e/e$. It was proved using Schamel's model that there is a maximum velocity for a shallow Maxwell-Boltzmann electron hole to travel in the bulk electrons, beyond which the solitary solution no longer exists: $v_h < 1.3 v_{\mathrm{th,e}}$. Nevertheless, electron holes are sometimes observed [41] to travel faster than this threshold velocity, implying deviation from the Schamel's model. Another useful result is obtained making a further assumption that the shallow electron hole is slowly moving $v_h \ll v_{\mathrm{th,e}}$, a simple analytic form of the potential ϕ was obtained in this case [40]

$$\phi = \psi \operatorname{sech}^4(x/4\lambda_{De}). \tag{1.38}$$

This potential profile is sometimes referred to as Schamel's electron hole potential [40].

III.3 Observational features of electron holes

Electron holes have been widely observed in space and laboratory plasma. Early space plasma probes sent back electric field measurements showing random noise in the electric field component parallel to the magnetic field direction with a wide range of frequencies [42]. Modern satellites with highly time-resolved (0.1 ms resolution or better [29]) electric field measurements enabled scientists to look at the fine details of this "noise". Strikingly, this "noise" is mainly composed of a series of bipolar electric field pulses. An example of this measurement is shown in Figure 1-6. Electron holes have been then widely accepted as the explanation for these observations. On a satellite the electric field signal is measured by Langmuir probes. Modern satellites often have three pairs of Langmuir probes, one in each direction [43]. The schematic of a THEMIS satellite and the positions of its electric field sensors is shown in Figure 1-7. The time delay in the measurement on different probes

is used to deduce the velocity of such a structure. Sometimes, the measurement between two adjacent satellites can also be used [44]. Measurements from space often show that these electron holes travel at a velocity on the order of the local electron thermal velocity $v_{\mathrm{th,e}} = \sqrt{T_e/m_e}$ and extend several or several tens of Debye lengths [45]. In the more terrestrial units, they travel at the order of 1000 km/second and their spatial extent is on the order of 100 m to 1000 m. Electron holes have been reported to be present in a wide range of space plasma regions. Different satellite missions have reported their existence all the way from Earth's auroral zone [30] to free solar wind [32]. These observations are often made when there is strong plasma dynamics nearby such as magnetic reconnection [46, 47] and collisionless shocks [32]. Satellite missions that have reported the observations of electron holes include: FAST [30], WIND [48], Cluster [49], THEMIS/ARTEMIS [50], GEOTAIL [47], Van Allen Probes [51] and MMS [34].

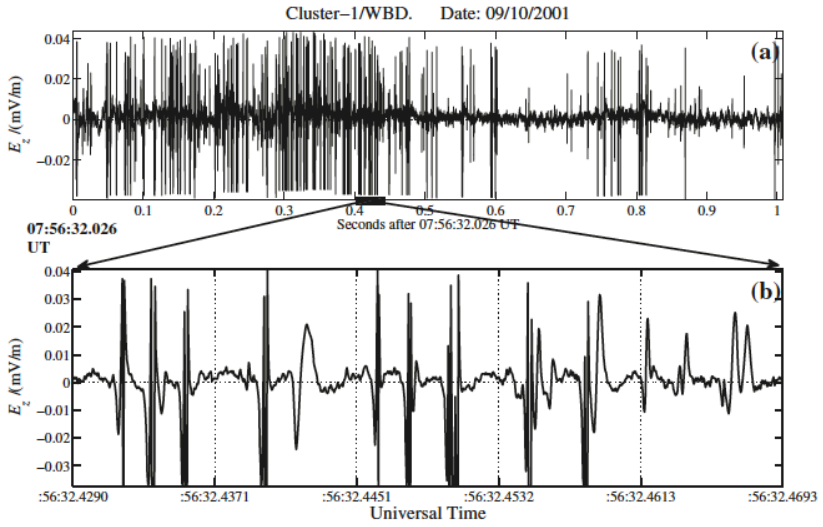

Figure 1-6: Parallel electric field measurement showing electron holes within magnetic reconnection diffusion region at magnetopause, measured by Cluster satellite. Plot adapted from reference [49].

In laboratory, electron holes have been observed during magnetic reconnection experiments on Versatile Toroidal Experiment (VTF) [36]. An array of small 60 µm diameter Langmuir probes are used and phase shift on a pair of probes separated by 2 mm is used to deduce the electron hole velocity. These electron holes generated by magnetic recon-

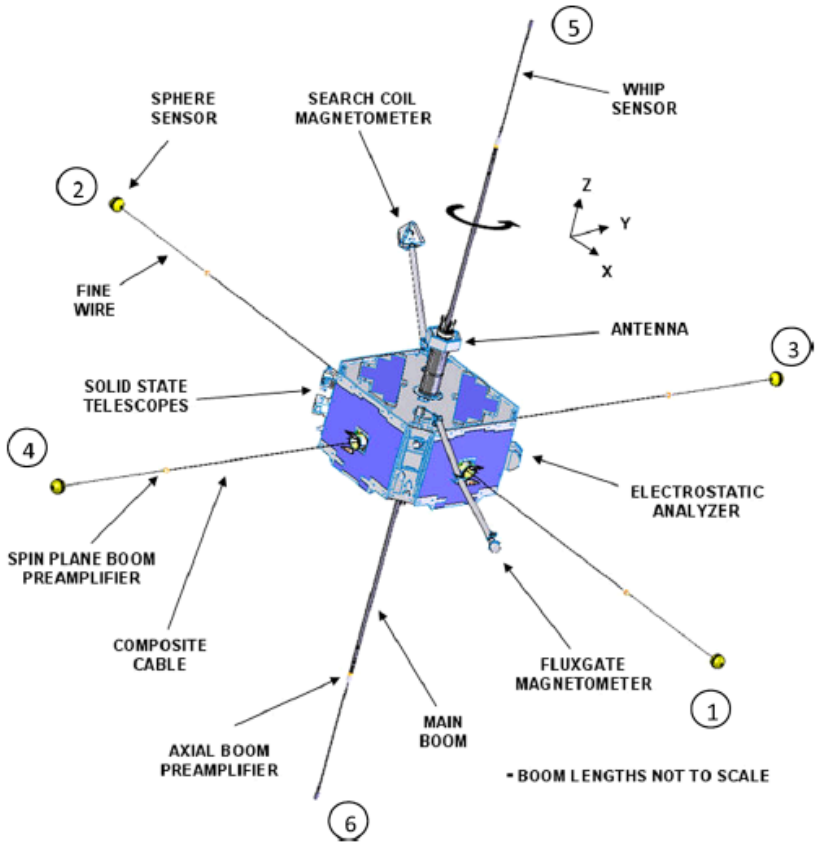

Figure 1-7: Schematic of a THEMIS mission satellite with six electric field sensors. Adapted from reference [43]

nection travel at nearly 4000 km/s ($2.21 v_{\mathrm{th,e}}$) and have a parallel dimension of 1.5 mm ($60\lambda_{De}$). More recently, Lefebvre *et al.* [37] reported observation of electron holes on the LAPD basic plasma facility excited by electron beam injection. Langmuir probes as small as 10 µm in diameter are used to make the observation. Measuring electron holes in laboratory plasma requires sub-Debye-length Langmuir probes, which often need special development.

III.4 Electron holes in higher dimensions

Up to now, we have mainly talked about the theory of electron holes in one spatial dimension. This section reviews some existing literature results on electron holes in higher dimensions.

It can be proved that electron holes cannot exist in unmagnetized isotropic plasma [52].

In this case, there is not enough phase space volume for trapped particles to provide charge for the formation of an electron hole as the phase space volume of trapped electrons scales like $\psi^{N_d/2}$ with N_d the dimensionality [52]. Having a strong magnetic field can bypass this difficulty by reducing the effective dimensionality. It has been confirmed by various PIC simulations that the magnetic field needs to be higher than a threshold value for electron holes to stably exist in three dimensions. The most frequently cited stability criterion is due to Muschietti *et al.* [53], which states that the stability threshold is $\Omega_e > \omega_b$. $\Omega_e = \sqrt{eB/m_e}$ is the electron cyclotron frequency and $\omega_b = \sqrt{e\psi/m_e}/L_\parallel$ is the bounce frequency for trapped electrons with parallel hole length $L_\parallel$. If the magnetic field is not strong enough, an electron holes is observed to "kink" in the transverse direction and its amplitude shrinks until the hole is localized transversely or dissipates. The exact threshold and the instability mechanism remain not completely solved and are subjects of ongoing research [54, 55]. Electron holes are therefore intrinsically lower dimensional objects moving along magnetic field lines. Simplified 1D models are widely used to study electron holes and often produce reasonable agreement with measurements from space [45]. Even in strongly magnetized plasma, electron holes are observed in simulations to resonantly interact with whistler waves and may break up as a result [56]. The three dimensional structure of electron holes in space gives rise to a mono-polar [44] electric field signal perpendicular to the magnetic field direction and sometimes magnetic field perturbations are also observed [50] to be associated with electron holes. Electron holes having a magnetic field signature are often referred to as electromagnetic electron holes as opposed to electrostatic electron holes.

III.5 Electron holes in plasma wake of an object

Electron holes can also be found in kinetic simulations of the plasma wake behind an unmagnetized object in cross-field flow of strongly magnetized plasma [57]. When a plasma flows through an object, the ions fill in the void behind the object more slowly than the electrons, forming an electrostatic potential structure that repels electrons and attracts ions. This particular electrostatic energy landscape makes some electrons, having

barely enough energy to overcome the repelling force or barely reflected by it, stay in the central wake for the longest time. The drifting orbit effect forms a "dimple" in the electron distribution function in the vicinity of these electrons [58]. The dimples get more pronounced further away the orbits drift from the object. Eventually, the dimpled distribution is Penrose unstable and electron holes form from it. A snapshot of the simulation in reference [57] is shown in Figure 1-8. The bottom panel shows the formation of electron holes along the S-shaped "dimple" in electron phase space. Most of the electron holes are observed to move out very fast while one electron hole at central wake remains almost stationary and grows. In this plot, the central electron hole has grown large enough to significantly perturb the ion density (see the top panel).

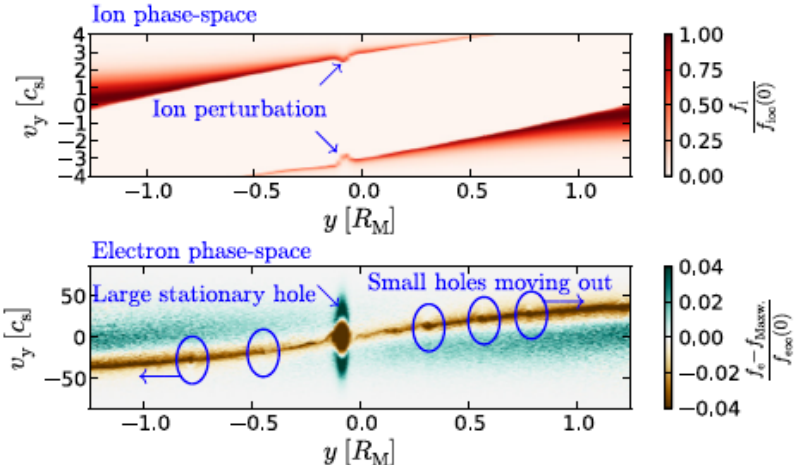

Figure 1-8: Kinetic simulation of plasma wake. Top: ion phase space. Bottom: electron phase space showing the formation of holes. The electron phase space density contours are the difference between the PIC simulation f_e and a Maxwellian distribution for better visibility of holes. Plot adapted from reference [29].

The simulation prediction that kinetic instability in plasma wake behind an unmagnetized object generates electron holes is supported by actual spacecraft data. ARTEMIS mission is a NASA mission of two satellites orbiting the moon. A statistical study of the solitary electrostatic waves encounters by these satellites shows a higher concentration of electron holes in the lunar wake compared to free solar wind. A plot illustration is shown in Figure 1-9. The data show a significantly higher concentration of electron hole events in the lunar plasma wake. The dwell time of satellites is quite uniform around the moon

and the space is uniformly sampled. The results are presented in the Geocentric Elliptic Coordinate system centered around the moon.

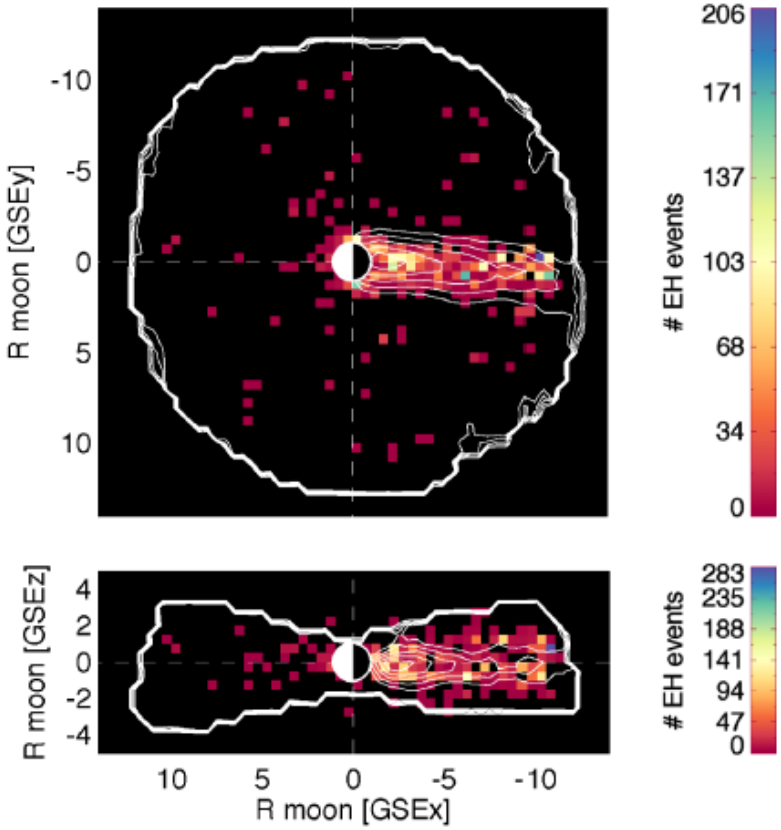

Figure 1-9: Event density of electron hole encounters around the moon, colors show the number of events. The contours are iso-density contours for protons showing the shape of lunar wake. Courtesy of David Malaspina.

IV Other nonlinear solitary wave phenomena in plasma

In this section, we are going to introduce other nonlinear solitary wave phenomena in plasma, with a focus on ion-acoustic solitons. In linear wave theory, the higher order terms in wave amplitude are neglected in linearization. However, when the wave amplitude becomes significant, the linear approach breaks down and nonlinear effects must be taken into account. Nonlinearity plays an important role in plasma physics. The BGK mode electron holes we have presented before in this chapter have strong trapped-particle

nonlinearity. Other nonlinearity such as the convective nonlinearity is responsible for the existence of fluid solitons and shock fronts in plasma [59]. Similar nonlinear waves are also actively studied in hydrodynamics for surface water waves [60] and in optics for light pulses traveling in optical fibers [61]. Plasma is inherently a nonlinear medium, which makes the study of nonlinear phenomena in plasma both important and fruitful.

IV.1 Ion-acoustic soliton and the Korteweg-de Vries equation

Ion-acoustic solitons are solitary pulses of ion perturbations traveling at a velocity slightly higher than the cold ion sound speed $c_s = \sqrt{T_e/m_i}$. They bear some similarities to electron holes. As a localized enhancement of ion density, an ion-acoustic soliton carries positive charge and is thus a positive potential pulse. Bipolar electric fields of the same polarity as an electron hole are associated with an ion-acoustic soliton. Its spatial width is also on the order of several Debye lengths. However, it is fundamentally different, because the ion accumulation provides the excess charge in an ion-acoustic soliton and it emerges from fluid equations rather than kinetic ones. To derive the governing equation of an ion-acoustic soliton, we start by assuming that ions are cold ($T_i \ll T_e$) and nondrifting relative to the electrons. Furthermore, electron inertia is neglected ($m_e \to 0$) and electrons are assumed to be isothermal with an equation of state $P_e = n_e T_e$. Conservation of electron momentum under these assumptions gives what is often referred to as the *Boltzmann electron* approximation for electron density

$$n_e = n_0 \exp\left(e\phi/T_e\right), \tag{1.39}$$

where n_0 is the background electron density. For the ions, we have conservation of density and momentum equations

$$\frac{\partial n_i}{\partial t} + \frac{\partial (n_i v_i)}{\partial x} = 0, \tag{1.40}$$

$$\frac{\partial v_i}{\partial t} + v_i \frac{\partial v_i}{\partial x} = -\frac{e}{m_i}\frac{\partial \phi}{\partial x}. \tag{1.41}$$

To simplify notation, we nondimensionalize the equations with the following normalization: $n_i/n_0 = n$, $v_i/c_s = u$, $x/\lambda_{De} = \eta$, $\omega_{pi}t = \tau$, $e\phi/T_e = \Phi$. Equations (1.40) (1.41) together with Poisson's equation can be written in the dimensionless form

$$\frac{\partial n}{\partial \tau} + \frac{\partial (nu)}{\partial \eta} = 0, \tag{1.42}$$

$$\frac{\partial u}{\partial \tau} + u\frac{\partial u}{\partial \eta} + \frac{\partial \Phi}{\partial \eta} = 0, \tag{1.43}$$

$$\frac{\partial^2 \Phi}{\partial^2 \eta} = \exp(\Phi) - n. \tag{1.44}$$

We first look for a solitary stationary solution that travels with a Mach number M. A solitary solution implies the vanishing of all perturbations at the boundary, thus we have the boundary conditions: $\Phi \to 0$, $u \to 0$, $n \to 1$ as $|\eta - M\tau| \to \infty$. We integrate Equations (1.42), (1.43) with the boundary conditions and use the calculated density n in Equation (1.44). Multiplying Equation (1.44) by $\Phi' = \partial\Phi/\partial\eta$ and integrating with the boundary conditions, we have

$$\frac{1}{2}(\Phi')^2 = \left[\exp(\Phi) + M(M^2 - 2\Phi)^{1/2} - (M^2 + 1)\right]. \tag{1.45}$$

The right hand side of this equation is minus the Sagdeev potential $V(\Phi)$ we introduced while constructing an electron hole solution using the differential approach. We look for a solution that travels slightly faster than c_s with a small amplitude such that $\Phi \ll 1$ and $\delta M = M - 1 \ll 1$. Expand Equation (1.45) in Φ and δM and integrate it with the solitary boundary conditions; we get

$$\Phi = 3\delta M \,\mathrm{sech}^2\left[(\frac{1}{2}\delta M)^{1/2}(\eta - M\tau)\right]. \tag{1.46}$$

This is the stationary ion-acoustic soliton solution in small-amplitude limit. It gives the relation between the soliton amplitude and its velocity: $M = 1 + \psi/3$. Larger ion-acoustic solitons travel faster. The width of a soliton is of order $(\delta M)^{-1/2}$, therefore a faster soliton is narrower. There is one-to-one relationship between amplitude, width and velocity.

Furthermore, it also gives the scaling of η and τ. We introduce ϵ as the scale of δM and a new coordinate $\xi = \eta - \tau$. This is equivalent to changing the reference frame to a moving frame with velocity c_s. The argument in Equation (1.46) can be expressed as $(1/\sqrt{2})\left[\delta M^{1/2}\xi - \delta M^{3/2}\tau\right]$. Therefore, the partial derivatives scale like $\partial/\partial\xi \sim \epsilon^{1/2}$ and $\partial/\partial\tau \sim \epsilon^{3/2}$. We can rewrite the equations with the new variables

$$\frac{\partial n}{\partial \tau} + \frac{\partial (n(u-1))}{\partial \xi} = 0, \tag{1.47}$$

$$\frac{\partial u}{\partial \tau} + (u-1)\frac{\partial u}{\partial \xi} + \frac{\partial \Phi}{\partial \xi} = 0, \tag{1.48}$$

$$\frac{\partial^2 \Phi}{\partial \xi^2} = \exp(\Phi) - n. \tag{1.49}$$

Now we expand the equations near a stationary solution of small amplitude traveling near c_s. We introduce the following expansions

$$n = 1 + \epsilon n^{(1)} + \epsilon^2 n^{(2)} + \dots, \tag{1.50}$$

$$\Phi = \epsilon \Phi^{(1)} + \epsilon^2 \Phi^{(2)} + \dots, \tag{1.51}$$

$$u = \epsilon u^{(1)} + \epsilon^2 u^{(2)} + \dots. \tag{1.52}$$

The lowest order equations with the solitary solution boundary conditions give $n^{(1)} = \Phi^{(1)} = u^{(1)}$. To next order in ϵ, the equations can be combined into one nonlinear partial differential equation only involving $\Phi^{(1)}$

$$\frac{\partial \Phi^{(1)}}{\partial \tau} + \Phi^{(1)}\frac{\partial \Phi^{(1)}}{\partial \xi} + \frac{1}{2}\frac{\partial^3 \Phi^{(1)}}{\partial \xi^3} = 0. \tag{1.53}$$

This is the Korteweg-de Vries (KdV) equation, which was first derived by Korteweg and de Vries [62] studying long surface waves in water in a channel of constant depth. It governs a wide range of nonlinear phenomena in physics. The second term $\Phi^{(1)}\partial\Phi^{(1)}/\partial\xi$ in Equation (1.53) is the nonlinear convective term responsible for wave steepening, the last term $\frac{1}{2}\partial^3\Phi^{(1)}/\partial\xi^3$ is the dispersive term responsible for wave dispersion. A solitary solution forms and propagates without changing its shape at the balance of these two

different effects.

The KdV equation has many interesting properties. The key property is that it admits solitary solutions. More importantly, these solitary solutions have a particle-like behavior. They emerge from collisions without changing their shape. For this reason, the solitary solution was given the name "soliton" by Zabusky and Kruskal [63] (Kruskal was also one of the discoverers of the BGK modes). The initial value problem of the KdV equation can be solved analytically by inverse scattering transform [64]. It has important implications in partial differential equation theory, as it is one of the prototypical exactly solvable nonlinear partial differential equations [65].

IV.2 Schamel's modified Korteweg-de Vries equation with resonant electrons

The derivation of Korteweg-de Vries equation in the context of an ion-acoustic soliton assumes isothermal electrons, which does not take into account the resonant electrons. Resonant electrons trapped inside the wave trough can interact strongly with the ion acoustic soliton and they do not typically obey the isothermal behavior. In fact, observations [66] indicate that flat-topped or dimpled electron distribution is possible inside ion-acoustic waves. Schamel [67] suggested a new kind of electron equation of state, taking into account the possibility of having a plateaued or hole-like distribution with the Maxwell-Boltzmann distribution for the resonant particles. It suffices to replace the Boltzmann electron equation of state by the Schamel's electron equation of state and follow the same approach we have introduced. One then arrives at a modified KdV equation exhibiting a stronger nonlinearity

$$\frac{\partial \Phi}{\partial \tau} + (1 + b\Phi^{\frac{1}{2}})\frac{\partial \Phi}{\partial \xi} + \frac{1}{2}\frac{\partial^3 \Phi}{\partial \xi^3} = 0. \tag{1.54}$$

The constant $b = (1-\beta)/\pi^{1/2}$ is related to the particle trapping coefficient β of Equation (1.36). The trapped region of electron distribution function is a plateau if $\beta = 0$ and a hole if $\beta < 0$. Schamel found that the numerical solutions of this modified KdV equation

satisfy qualitatively the same behavior as that of a KdV equation. The stationary solution of Schamel's mKdV equation gives solitons with smaller width and higher speeds than the KdV solitons because of its stronger nonlinearity.

V Thesis motivation and outline

This thesis aims to understand the time dependent behavior of electron holes on a quantitative level, namely how the velocity of an electron hole evolves over time and the stability of a stationary electron hole. Another aspect of this thesis is to study the ion coupling effect of electron holes and understand the boundary between an electron hole and a soliton.

The past theoretical work in this field has a strong focus on constructing stationary electron hole solutions and studying their structural properties [67, 52, 68, 45, 69]. Dupree [70] studied the dynamics of phase-space holes using global momentum conservation. His main interest was the growth mechanism and he had a focus on ion holes. As we shall see in Chapter 2 and Chapter 3 of this thesis, his theory is flawed as he introduced approximations too early in his derivations and therefore cannot account for what is observed in numerical simulations. Stability theory for BGK electron holes was attempted by Lewis and Symon [71], Schamel and Jovanović [72, 73]. The past theoretical work on hole stability often consists of abstruse mathematical operator theory and was never successfully applied to explain instabilities observed in simulations to the best of our knowledge. Furthermore, some of these analyses have adopted a symmetric potential eigenmode as an approximation and expand in inverse powers of frequency [72, 73]. However, as we shall see in this thesis, the observed destabilizing eigenmode is approximately a low-frequency antisymmetric mode so these assumptions would be inappropriate. The past numerical simulations in the literature, on the other hand, are relatively empirical and qualitative [74, 75, 76, 77, 78, 79], making it difficult to compare with existing theory. This knowledge gap constitutes motivation for this thesis.

The current thesis work starts from first principles and lays out a new theoretical and

simulation framework to study these nonlinear objects. The results from the theory and simulations are compared quantitatively to one another. The questions that this thesis tries to answer are of fundamental importance and have potential applications in space physics. The chapters in this thesis are organized in the following way:

Chapter 2 introduces the novel approach of hole kinematics and derives the momentum rate of change that governs the hole velocity. The "jetting" effect is found to be crucial to the hole velocity. Constant acceleration and growth are considered in this chapter. This chapter mainly consists of analytic treatment and the phenomena predicted by the theory will be verified by numerical simulations in the following chapter. The materials presented in this chapter have been published as a journal paper which can be found in reference [80].

Chapter 3 introduces a novel Particle-In-Cell simulation code. A hole tracking technique enables us to follow the trajectory of a fast-moving solitary hole and study quantitatively hole acceleration and coupling to ions. We observe a transient at the initial stage of hole formation when the hole accelerates to several times the cold-ion sound speed. Artificially imposing slow ion speed changes on a fully formed hole causes its velocity to change even when the ion stream speed in the hole frame greatly exceeds the ion thermal speed, so there are no reflected ions. The behavior that we observe in numerical simulations agrees very well with our analytic results presented in Chapter 2. The materials presented in this chapter have been published as a journal paper which can be found in reference [81].

Chapter 4 reports a new type of instability of electron holes interacting with passing ions. The nonlinear interaction of electron holes and ions is investigated by extending the theory presented in Chapter 2 to the frequency domain. It is shown that the oscillation in the velocity of an electron hole parallel to the magnetic field direction becomes unstable when the hole velocity in the ion frame is slower than a few times the cold ion sound speed. The instability mechanism can drive significant perturbations in the ion density. The instability threshold, oscillation frequency and instability growth rate derived from the theory yield quantitative agreement with the observations from the novel high-fidelity

hole-tracking Particle-In-Cell (PIC) code we have introduced in Chapter 3. The materials presented in this chapter have been published as a journal paper which can be found in reference [82].

Chapter 5 demonstrates that an electron hole can form a stable coupled state with an ion-acoustic soliton, namely a coupled hole-soliton pair. This combined structure travels at a velocity slightly higher than the ion sound speed in the ion frame. It exhibits soliton-like behavior during collisions though different from a classical KdV soliton. A velocity gap between the coupled state and the free state of an electron hole is explored and the velocity gap is observed to be set by the hole oscillatory velocity instability introduced in Chapter 4. Transition between these two states is shown to be possible in both directions by going through an unstable phase. Finally, the implications of these results for space observations are discussed. The materials presented in this chapter is a journal paper in preparation.

Chapter 6 summarizes this thesis and briefly introduces the extension of this thesis work to future work such as understanding electron hole transverse instability in higher dimensions.

Chapter 2

Electron hole kinematics deduced from momentum conservation

This chapter explains the analysis of reference [80], of which Ian H. Hutchinson was the principal author, but to which Chuteng Zhou made significant contributions. The derivations in this chapter serve as the foundation for what follows. The exposition here is in the words of the present author.

In this chapter, we are going to analyze the kinematic properties of electron holes and develop an analytic theory governing how their velocities change. The aim is to explain the velocity of electron holes observed in simulations and space with this theoretical framework. The essence of this theory is conservation of plasma momentum in the direction parallel to the magnetic field. In a Vlasov-Poisson plasma, the total particle momentum is conserved with vanishing boundary conditions for the fields. When the plasma is magnetized, the Vlasov-Poisson system is a reasonably good description of plasma dynamics parallel to the magnetic field. The electromagnetic momentum of the field can be ignored for a field aligned electrostatic structure and the sum of electron and ion momentum is conserved

$$\dot{P}_i + \dot{P}_e = 0, \tag{2.1}$$

where $\dot{P}_i$ and $\dot{P}_e$ are respectively the rates of momentum change for ions and electrons.

The electron hole kinematics and the evolution of its velocity are determined by this momentum conservation relation. The treatment is one-dimensional and is intended to describe the parallel motions of electron holes. Electron holes need a strong enough magnetic field to stably exist (see Chapter 1) and therefore can be modeled by structures moving along the field lines. This analytic theory also quantitatively characterizes the strength of momentum coupling between an electron hole and the ions.

I Ion momentum rate of change

We consider the effects of hole acceleration and change of hole shape on ion momentum. First, we clarify some terms. The electron hole potential is denoted by $\phi(x)$. It is a solitary pulse that extends from x_1 to x_2 in its rest frame. x_1 and x_2 are taken to be far away enough from the hole center such that ϕ and its derivatives vanish at these boundaries. The exact choice of x_1 and x_2 is unimportant given that there is no potential difference between $\phi(x_1)$ and $\phi(x_2)$. So we consider a symmetric electron hole while asymmetric holes can also exist. Subscripts 1 and 2 denote values at x_1 and x_2. Electron hole velocity in the lab frame is denoted by U. The principles of our method are illustrated in Figure 2-1. Hole acceleration and deformation induce change in the particle velocity and density. The momentum rate of change in the region outside the hole region $[x_1, x_2]$ is given by $\dot{P}_{\text{out}} - \dot{P}_{\text{in}}$. The total momentum rate of change can be obtained adding the momentum rate of change inside the hole region $\dot{P}_{\text{contained}}$ with the momentum outflow rate

$$\dot{P}_{\text{total}} = \dot{P}_{\text{contained}} + (\dot{P}_{\text{out}} - \dot{P}_{\text{in}}). \tag{2.2}$$

For the purpose of calculating $\dot{P}_{\text{total}}$ for ions, we consider a single ion stream. This method can be generalized to a distribution of particles with trapped species as we are going to show in the case of electrons. It is important to note that the final momentum rate of change will be evaluated in an inertial frame, while for the simplicity of calculation, we are also going to use the rest frame of the electron hole, which may not be an inertial frame of reference. If it is not stated otherwise, the variables are evaluated in the hole

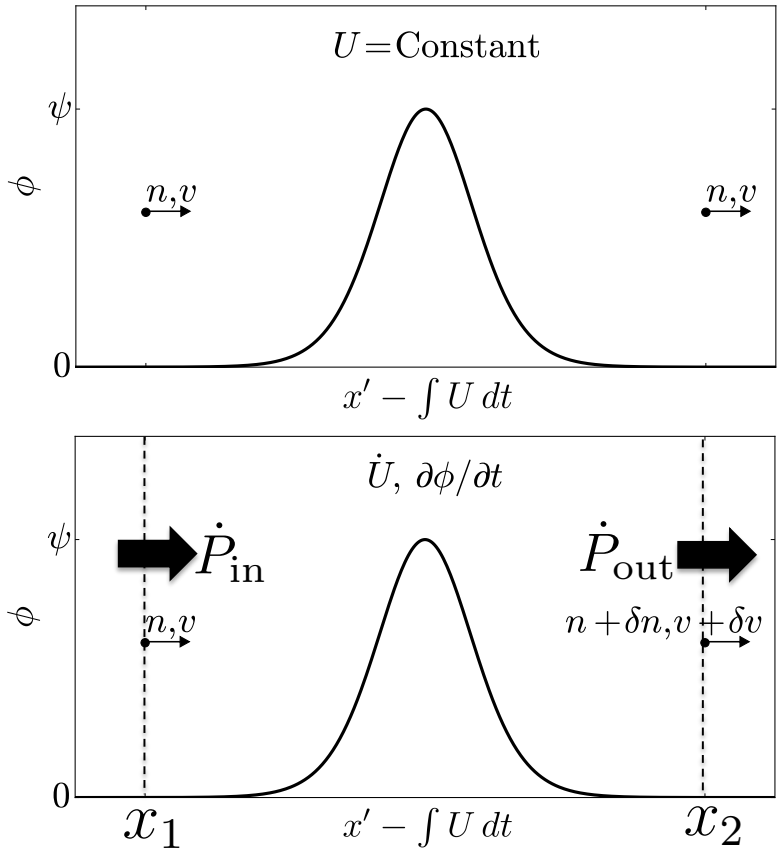

Figure 2-1: Top: a passing particle exits the hole region with exactly the same velocity as it enters when the hole has a constant velocity and does not change its shape. Bottom: there is change in passing particle velocity and density thus momentum transfer when the hole is accelerating or changing its shape.

rest frame. All the inertial frame quantities are denoted with primes. For example, v' is related to v by $v' = v + U(t)$, where $U(t)$ is the instantaneous velocity of the electron hole in the lab/inertial frame.

I.1 Momentum change due to hole acceleration

We first introduce ion transit time

$$\delta t_i = \int_{x_1}^{x_2} \frac{dx}{v}. \tag{2.3}$$

This duration is the time it takes for an ion to transit the hole region. We first fix the hole shape $\phi(x)$ and only consider the acceleration effect. In the rest frame of the electron hole, an ion admits a constant of motion by integrating its equation of motion

$$\frac{1}{2}m_i v^2 + e\phi + m_i \dot{U} x = \text{Constant}, \tag{2.4}$$

where $\dot{U}$ is the hole acceleration. For this analysis, we study the constant acceleration case where $\dot{U}$ is constant. We first calculate net momentum outflow rate

$$\begin{aligned}
\dot{P}_{\text{out,i}} - \dot{P}_{\text{in,i}} &= m_i(n_2 v_2 v_2' - n_1 v_1 v_1') \\
&= m_i(n_2 v_2 v_2' - n_2 v_2 v_1' + n_2 v_2 v_1' - n_1 v_1 v_1') \\
&= m_i \left[n_2 v_2 (v_2' - v_1') + (n_2 v_2 - n_1 v_1) v_1' \right]. \qquad (2.5)
\end{aligned}$$

This expression should be evaluated simultaneously at time t for all the quantities involved. The first term in the final expression accounts for the change in ion velocity in the inertial frame. $v_2'(t) - v_1'(t)$ can be related to hole rest frames quantities by

$$\begin{aligned}
v_2'(t) - v_1'(t) =& v_2(t) - v_1(t) \qquad (2.6) \\
=& v_2(t) - v_1(t - \delta t_i) + \delta t_i \dot{U}.
\end{aligned}$$

We use the constant of motion along the ion orbit to determine $v_2(t) - v_1(t - \delta t_i)$

$$\begin{aligned}
v_2(t) - v_1(t - \delta t_i) &= \frac{2\dot{U}(x_1 - x_2)}{v_1(t - \delta t_i) + v_2(t)} \\
&= \dot{U} \int_{x_1}^{x_2} \frac{-2}{v_1(t - \delta t_i) + v_2(t)} \, dx. \qquad (2.7)
\end{aligned}$$

Therefore, the first term of the net momentum outflow rate in Equation (2.5) is

$$m_i n_2 v_2 (v_2' - v_1') = m_i n_2 \dot{U} \int_{x_1}^{x_2} \left(\frac{-2 v_2(t)}{v_1(t - \delta t_i) + v_2(t)} + \frac{v_2}{v} \right) dx. \tag{2.8}$$

Up to now, no approximations have been made. We make a first approximation here assuming that ion transit time δt_i is much shorter than the typical acceleration time scale $v/\dot{U}$

$$|\dot{U}\delta t_i/v| \ll 1. \tag{2.9}$$

This approximation is going to be referred to as the *short transit-time approximation*. The net momentum transfer effects can be expanded as a power series of the small expansion parameter $|\dot{U}\delta t_i/v|$. We only retain the lowest order contributions. For this reason, we can be more liberal about using interchangeably the values within one transit time in the following algebra, knowing that this approximation only leads to higher order corrections. Using the short transit-time approximation for ions, we can replace n_2 by n_1, $2v_2(t)/(v_1(t-\delta t_i)+v_2(t))$ by 1 and v_2 by v_1 in Equation (2.8) to lowest order and we have

$$m_i n_2 v_2 (v_2' - v_1') \simeq m_i n_1 \dot{U} \int_{x_1}^{x_2} \left(-1 + \frac{v_1}{v}\right) dx. \tag{2.10}$$

The second term in Equation (2.5) accounts for net momentum outflow due to accumulation of ions inside the hole region. Continuity equation for ions gives

$$n_2 v_2 - n_1 v_1 = -\int_{x_1}^{x_2} \frac{\partial n}{\partial t}\, dx = -\dot{N} \tag{2.11}$$

The density n can be considered as the sum of steady state density and a small correction first order in small expansion parameter $|\dot{U}\delta t_i/v|$

$$n = \frac{n_1 v_1}{v}(1 + \mathcal{O}(|\dot{U}\delta t_i/v|)) \tag{2.12}$$

To the lowest order, the ion accumulation rate is

$$\int_{x_1}^{x_2} \frac{\partial n}{\partial t}\, dx \simeq \int_{x_1}^{x_2} \left(\frac{n_1}{v}\frac{\partial v_1}{\partial t} - \frac{n_1 v_1}{v^2}\frac{\partial v}{\partial t}\right) dx. \tag{2.13}$$

The density of ion stream n_1 when it enters hole region is determined by the background ion density, it is thus a constant in time. $\partial v_1/\partial t$ is simply $-\dot{U}$ as the hole frame is

accelerating. $\partial v/\partial t$ can be obtained from the constant of motion

$$\frac{1}{2}m_i v_1^2 + m_i \dot{U} x_1 = \frac{1}{2}m_i v^2 + \phi(x) + m_i \dot{U} x. \tag{2.14}$$

Take the partial derivative of the above equation with respect to time while fixing x gives

$$\frac{\partial v}{\partial t} = \frac{v_1}{v}\frac{\partial v_1}{\partial t} = -\frac{v_1}{v}\dot{U}. \tag{2.15}$$

Now choose the inertial frame as the instantaneous rest frame of the electron hole such that $v_1' = v_1$ and the second term in Equation (2.5) can be written as

$$\begin{aligned} m_i v_1'(n_2 v_2 - n_1 v_1) &= -m_i v_1 \dot{N} \\ &= m_i n_1 \dot{U} \int_{x_1}^{x_2} \left(\frac{v_1}{v} - \frac{v_1^3}{v^3}\right) dx. \end{aligned} \tag{2.16}$$

We have only retained the lowest order terms. To lowest order in $|\dot{U}\delta t_i/v|$, the net momentum outflow rate is obtained by adding Equations (2.10) and (2.16) together

$$\dot{P}_{\text{out,i}} - \dot{P}_{\text{in,i}} = m_i n_1 \dot{U} \int_{x_1}^{x_2} \left[-1 + 2\frac{v_1}{v} - \left(\frac{v_1}{v}\right)^3\right] dx. \tag{2.17}$$

Last we calculate the contained ion momentum rate of change

$$\dot{P}_{\text{contained,i}} = \frac{d}{dt}\int_{x_1}^{x_2} m_i n v'\, dx \tag{2.18}$$

$$= \frac{d}{dt}\int_{x_1}^{x_2} m_i n (v + U)\, dx. \tag{2.19}$$

Recall that to lowest order, $nv = n_1 v_1$ and again we choose the inertial frame as the instantaneous rest frame of the electron hole such that instantaneously $U = 0$. Therefore we get

$$\dot{P}_{\text{contained,i}} = m_i n_1 \dot{U} \int_{x_1}^{x_2} \left(-1 + \frac{v_1}{v}\right) dx. \tag{2.20}$$

The total rate of momentum change for ions due to hole acceleration is thus

$$\dot{P}_{\mathrm{i,a}} = m_i n_1 \dot{U} \int_{x_1}^{x_2} \left[-2 + 3\frac{v_1}{v} - \left(\frac{v_1}{v}\right)^3 \right] dx. \tag{2.21}$$

To lowest order, we can use the steady state velocity $v(x) = \sqrt{v_1^2 - 2e\phi(x)/m_i}$ in the above expression.

So far, we have not made any assumptions about the magnitude of ϕ. Expression (2.21) can be further simplified if we make the shallow hole approximation: $2e\phi \ll m_i v_1^2$. Define a small parameter of expansion $\epsilon = 2e\phi/m_i v_1^2$, the integrand in Equation (2.21) can then be expanded as

$$\begin{aligned} -2 + 3\frac{v_1}{v} - \left(\frac{v_1}{v}\right)^3 &= -\frac{3}{4}\epsilon^2 + \mathcal{O}(\epsilon^3) \\ &\simeq -3\left(\frac{e\phi}{m_i v_1^2}\right)^2. \end{aligned} \tag{2.22}$$

In the shallow hole limit, the total ion momentum rate of change due to hole acceleration can be approximately expressed as

$$\dot{P}_{i,a} \simeq m_i n_1 \dot{U} \int_{x_1}^{x_2} -3\left(\frac{e\phi}{m_i v_1^2}\right)^2 dx. \tag{2.23}$$

The short transit time approximation holds when the ions are not in the vicinity of being reflected. The momentum effect of reflected ion streams will be discussed at the end of next section.

I.2 Momentum change due to hole growth

In this section, we calculate the effect of hole potential change on the ion momentum. Instead of considering a hole accelerating without changing its shape, we assume right now that the hole is stationary $\dot{U} = 0$ while its potential is subject to temporal variation $\dot{\phi} \neq 0$. In this section, there is no difference between the hole rest frame and the inertial frame. The *short transit-time approximation* we are going to use in this case is similar in

nature to the one before. It consists of assuming that any change in the velocity of an ion transiting the hole due to $\dot{\phi}$ is a first order correction to its orbit. In a more mathematical language, this approximation can be expressed as

$$|\dot{\phi}\delta t_i/\phi| \ll 1. \tag{2.24}$$

Recall that the net momentum outflow rate is $\dot{P}_{\rm out,i} - \dot{P}_{\rm in,i} = m_i\left[n_2 v_2(v_2' - v_1') + (n_2 v_2 - n_1 v_1)v_1'\right]$. The difference in ion velocity can be calculated integrating its equation of motion. The energy difference of an ion between x_1 and x_2 is

$$\begin{aligned}\frac{1}{2}m_i v_2^2 - \frac{1}{2}m_i v_1^2 &= \int_{t_1}^{t_2} e\dot{\phi}\, dt \\ &= \int_{x_1}^{x_2} \frac{e\dot{\phi}}{v}\, dx.\end{aligned} \tag{2.25}$$

This energy difference comes from energization/de-energization due to hole potential change during the transit time. To lowest order in $\dot{\phi}\delta t_i/\phi$, the velocity difference can be expressed as

$$v_2' - v_1' = v_2 - v_1 \simeq \frac{1}{m_i v_1^2}\int_{x_1}^{x_2} \frac{v_1}{v} e\dot{\phi}\, dx. \tag{2.26}$$

The accumulation of ion density inside the hole due to $\dot{\phi}$ can be expressed using the lowest order expression $n_1 v_1 = nv[1 + \mathcal{O}(\dot{\phi}\delta t_i/\phi)]$. To lowest order, we have

$$\begin{aligned}\dot{N} &\simeq \int_{x_1}^{x_2} n_1 \frac{\partial}{\partial t}\left(\frac{v_1}{v}\right) dx \\ &= n_1 \int_{x_1}^{x_2} -\frac{v_1}{v^2}\frac{\partial v}{\partial \phi}\dot{\phi}\, dx \\ &\simeq \frac{n_1}{m_i v_1^2}\int_{x_1}^{x_2} \frac{v_1^3}{v^3} e\dot{\phi}\, dx.\end{aligned} \tag{2.27}$$

The contained ion momentum rate of change due to hole growth is zero to relevant order as $nv \simeq n_1 v_1$ is constant in time. Thus the total rate of change of ion momentum due to

hole growth $\dot{\phi}$ is

$$\begin{aligned}\dot{P}_{i,g} &\simeq m_i \left[n_2 v_2 (v_2' - v_1') + (n_2 v_2 - n_1 v_1) v_1'\right] \\ &\simeq m_i n_1 v_1 \int_{x_1}^{x_2} \left[\frac{v_1}{v} - \left(\frac{v_1}{v}\right)^3\right] \frac{e\dot{\phi}}{m_i v_1^2}\, dx. \end{aligned} \tag{2.28}$$

With shallow hole approximation, we can again expand the $v_1/v - v_1^3/v^3$ as $-\epsilon + \mathcal{O}(\epsilon^2)$. Then to lowest order in $\epsilon = 2e\phi/m_i v_1^2$. The final result for a shallow electron hole is

$$\dot{P}_{i,g} \simeq -m_i n_1 v_1 \int_{x_1}^{x_2} \frac{\partial}{\partial t} \left(\frac{e\phi}{m_i v_1^2}\right)^2 dx. \tag{2.29}$$

So far, we have only considered the situation where ions are much faster than the reflection velocity limit in the hole frame. The short transit-time approximation will first break down when the ion velocity approaches the minimum required to overcome the potential barrier in the hole frame. When the ion stream does not have enough energy to go through the electron hole potential barrier in the hole frame, it is reflected. The momentum change of an reflected ion is $-2m_i v_1$. For ion arrival rate of $n_1|v_1|$, the total rate of change of ion momentum due to reflection is

$$\dot{P}_{i,r} = -2m_i v_1 n_1 |v_1|. \tag{2.30}$$

This momentum rate of change is predominant when present and cannot be balanced by other effects. Therefore it is impossible for an electron hole to reflect ions at steady-state. Previously, Dupree [70] derived a momentum conservation relation for electron holes which only takes into account the reflected ion momentum change. Our results reveal the important jetting effects, which were previously ignored. We will see in Chapter 3 that jetting effects have important implications for electron hole motions.

II Electron momentum rate of change

We have calculated the momentum rate of change for a single ion stream in the previous section. The results can be readily applied to a distribution of passing ions or electrons given that the short transit-time approximation still holds. The major complication here is that electrons have both passing and trapped populations. Suppose that in the rest frame of the electron hole, the background electron population has a velocity distribution $f_1(v_1)$. Electrons are attracted by the hole potential and an electron arriving with velocity v_1 in the hole frame has a velocity $\sqrt{v_1^2 + 2e\psi/m_e}$ at the hole center, where ψ is the maximum of $\phi(x)$. The majority of passing electrons satisfy finite transit-time approximation for moderate hole accelerations and growths that we are interested in. Nevertheless, there is narrow band of orbits near the separatrix where finite transit-time approximation breaks down. It is only a tiny fraction of the total electron population, therefore we proceed ignoring these marginally passing electrons. When the electron hole is accelerating, the passing electrons have a momentum rate of change which is

$$\dot{P}_{e,p} = m_e \dot{U} \int_{x_1}^{x_2} \int_{-\infty}^{+\infty} \left[-2 + 3\frac{v_1}{v} - \left(\frac{v_1}{v}\right)^3 \right] f_1(v_1)\, dv_1 dx. \tag{2.31}$$

Similarly, the momentum rate of change due to hole growth for passing electrons is

$$\dot{P}_{e,g} = m_e \dot{U} \int_{x_1}^{x_2} \int_{-\infty}^{+\infty} \left[\frac{v_1}{v} - \left(\frac{v_1}{v}\right)^3 \right] \frac{-e\dot{\phi}}{m_e v_1^2} f_1(v_1)\, dv_1 dx. \tag{2.32}$$

The above expressions are for passing electrons. Trapped electrons move with the solitary potential. They accelerate together with the wave such that

$$\dot{P}_{e,t} = m_e \dot{U} \int_{x_1}^{x_2} n_t(x) dx. \tag{2.33}$$

$n_t(x)$ is the number density of trapped electrons. There is no hole growth acceleration for trapped electrons as on average a trapped electron has zero net momentum in the hole frame. The passing orbits near separatrix become trapped when an electron hole grows in size. We can neglect the momentum change of electrons associated with newly trapped

phase-space by the same argument.

To calculate the total electron momentum rate of change $\dot{P}_e$, we need to know the number of trapped electrons in an electron hole. This quantity can be obtained by a global charge neutrality argument. An electron hole has a solitary potential profile $\phi(x)$, thus Poisson's equation indicates that the total charge of an electron hole over the entire space is zero. We have seen in Chapter 1 that the distribution function of passing orbits is determined by the background distribution and the hole potential ϕ. With the short transit-time approximation, we use the electron orbits at steady state to calculate the total passing electrons number by constancy of distribution function on these orbits

$$N_p = \int_{x_1}^{x_2} \int_{-\infty}^{+\infty} \frac{v_1}{v} f_1(v_1)\, dv_1. \tag{2.34}$$

Total charge neutrality gives $N_p + N_t = N_i$. The total number of ions can be obtained integrating steady-state ion density for an electron hole traveling at a velocity U in the ion frame

$$N_i = n_1 \int_{x_1}^{x_1} \frac{|U|}{\sqrt{U^2 - 2e\phi(x)/m_i}}\, dx. \tag{2.35}$$

We have used the steady-state ion density $n_i = n_1|U|/\sqrt{U^2 - 2e\phi(x)/m_i}$ here, which is obtained by conservation of ion flux: $n_i v_i = n_1 v_1$. The momentum rate of change for trapped electrons can be evaluated as

$$\dot{P}_{e,t} = m_e \dot{U} \left[\int_{x_1}^{x_2} \frac{n_1|U|}{\sqrt{U^2 - 2e\phi(x)/m_i}}\, dx - \int_{x_1}^{x_2} \int_{-\infty}^{+\infty} \frac{v_1}{v} f_1(v_1)\, dv_1\, dx \right]. \tag{2.36}$$

When $e\psi \ll m_i v_1^2$, the ion density perturbation is negligible inside the electron hole and the above expression can be rewritten as

$$\dot{P}_{e,t} \simeq m_e \dot{U} \int_{x_1}^{x_2} \int_{-\infty}^{+\infty} \left(1 - \frac{v_1}{v}\right) f_1(v_1)\, dv_1\, dx. \tag{2.37}$$

The total electron momentum rate of change due to hole acceleration is obtained by

adding Equations (2.31) and (2.37)

$$\dot{P}_{e,a} = m_e \dot{U} \int_{x_1}^{x_2} \int_{-\infty}^{+\infty} \left[-1 + 2\frac{v_1}{v} - \left(\frac{v_1}{v}\right)^3 \right] f_1(v_1)\, dv_1 dx. \tag{2.38}$$

The integral over velocity can be performed to give a closed-form expression when the background electrons have a Maxwellian distribution in the hole frame

$$f_1(v_1) = \frac{n_1}{\sqrt{2\pi} v_{\mathrm{th,e}}} \exp(-\frac{v_1^2}{2v_{\mathrm{th,e}}^2}), \tag{2.39}$$

we can use an unshifted Maxwellian when the hole velocity U is significantly slower than the background electron thermal speed: $|U| \ll v_{\mathrm{th,e}}$. Defining $\chi = \sqrt{e|\phi(x)|/T_e}$, a integration over velocity gives

$$\dot{P}_{e,a} = -m_e n_1 \dot{U} \int_{x_1}^{x_2} h(\chi)\, dx. \tag{2.40}$$

The function h is defined as

$$\begin{aligned} h(\chi) \quad &= -\frac{2}{\sqrt{\pi}} \int_0^{+\infty} \left[-1 + \frac{2\xi}{(\chi^2+\xi^2)^{1/2}} - \frac{\xi^3}{(\chi^2+\xi^2)^{3/2}} \right] e^{-\xi^2} d\xi \\ &= -\frac{2}{\sqrt{\pi}} \chi + \left[(2\chi^2 - 1) e^{\chi^2} \operatorname{erfc}(\chi) + 1 \right]. \end{aligned} \tag{2.41}$$

It is useful to remark the asymptotic behaviors of the function $h(\chi)$ at shallow ($\chi \to 0$) and deep hole ($\chi \to \infty$) limits: $h(\chi) \to \chi^2 - \frac{8}{3\sqrt{\pi}}\chi^3$ as $\chi \to 0$ and $h(\chi) \to 1 - \frac{2}{\sqrt{\pi}\chi}$ as $\chi \to \infty$. In Figure 2-2, we have plotted the function h and its asymptotic approximations in two different limits. The term $-m_e \int_{x_1}^{x_2} h(\chi)\, dx$ in Equation (2.40) can be viewed as the effective mass of an electron hole. An electron hole has a negative effective mass because it is a density deficit.

One important aspect of electron hole dynamics is that it accelerates like an electron in the absence of ion response. Suppose there is a background force field F (gravity, large scale electric field) giving rise to a background acceleration $\dot{v}_b = F/m_e$. Then in a reference frame that is accelerating with the same acceleration $\dot{v}_b$, the electron momentum

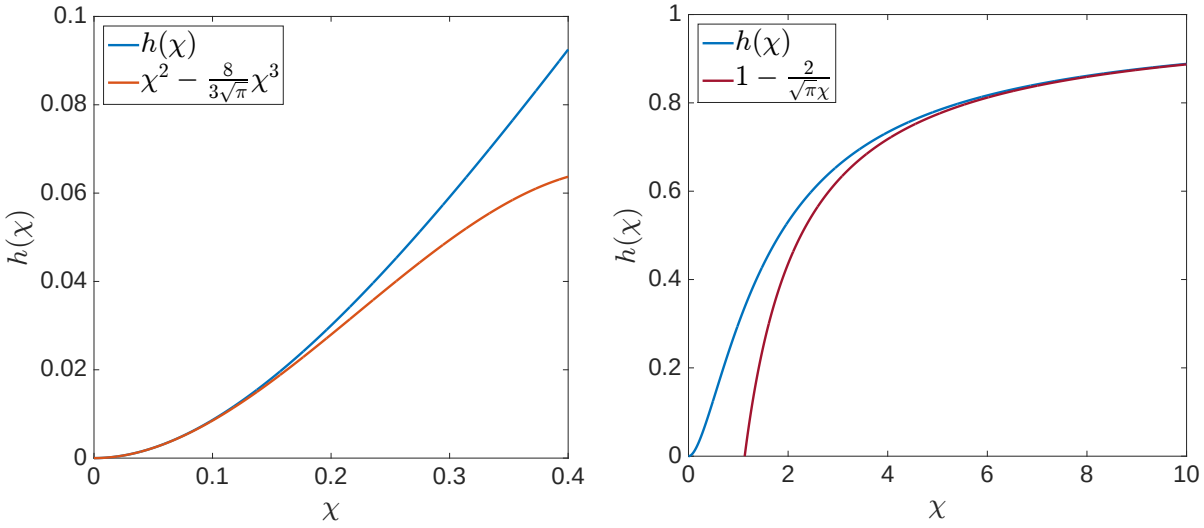

Figure 2-2: Plot of $h(\chi)$ compared with its asymptotic approximations.

rate of change is given by Galilean relativity

$$\dot{P}_{e,a} = -m_e n_1 (\dot{U} - \dot{v}_b) \int_{x_1}^{x_2} h(\chi)\, dx. \tag{2.42}$$

Neglecting ion contributions, the electron momentum rate of change should be zero in this accelerating frame, which is possible only if $\dot{U} = \dot{v}_b$. A fast electron hole with little ion response accelerates like an electron. In Dupree's terminology [70], an electron hole has the same effective charge-to-mass ratio as an electron.

III Acceleration caused by hole growth

Having derived all the basic equations for hole kinematics, now we apply the previous results to hole acceleration when its potential ϕ grows. Electron holes grow in amplitude during their formations by particle trapping. The evolution of their velocity during this growth stage is studied in this section. During hole growth, the momentum balance is between hole growth ion jetting effect, hole acceleration ion jetting effect and hole acceleration electron term. The hole growth electron term is small if the hole remains near the peak of electron distribution function such that $f_1' \simeq 0$ and $\dot{P}_{e,g}$ is zero to lowest order. The momentum balance equation can therefore be written in the rest frame of

background ions ($v_1 = -U$) as

$$-h(\chi)m_e\dot{U} - 3\left(\frac{e\psi}{m_iU^2}\right)^2 m_i\dot{U} + \left(\frac{2e^2\dot{\psi}\psi}{m_iU^3}\right) = 0. \tag{2.43}$$

To a first degree approximation, we model the hole potential by a rectangular pulse that is ψ in height. We have used the shallow hole approximation for the hole growth ion jetting and hole acceleration ion jetting terms. Defining a new variable $v_p = \sqrt{2e\psi/m_i}$ which is the ion passing velocity, we write the above equation in terms of v_p and U as

$$-\frac{m_e}{m_i}h(\frac{v_p}{\sqrt{2}c_s})\dot{U} - \frac{3}{4}\frac{v_p^4}{U^4}\dot{U} + \frac{v_p^3}{U^3}\dot{v}_p = 0. \tag{2.44}$$

This equation can be integrated numerically for an initial set of values (U_0, v_{p0}). We use a standard Runge-Kutta method to solve the equation numerically for different initial values. These growth curves are shown in Figure 2-3. When an electron hole grows in amplitude thus v_p, its velocity U should follow one of the curves. An electron hole born with a low velocity in the ion frame gets significant acceleration after the initial growth while those born at higher velocities are accelerated less. These phenomena shall be verified in numerical PIC simulations in Chapter 3.

IV Electron hole momentum coupling to ions by hole pushing and pulling

Suppose a shallow electron hole is accelerated at $\dot{U}$ without changing its shape. It induces change in ion and electron momentum at rates

$$\dot{P}_{e,a} = -m_e n_1 \dot{U} \int_{x_1}^{x_2} h(\chi)\, dx, \tag{2.45}$$

$$\dot{P}_{i,a} = m_i n_1 \dot{U} \int_{x_1}^{x_2} -3\left(\frac{e\phi}{m_i v_1^2}\right)^2 dx. \tag{2.46}$$

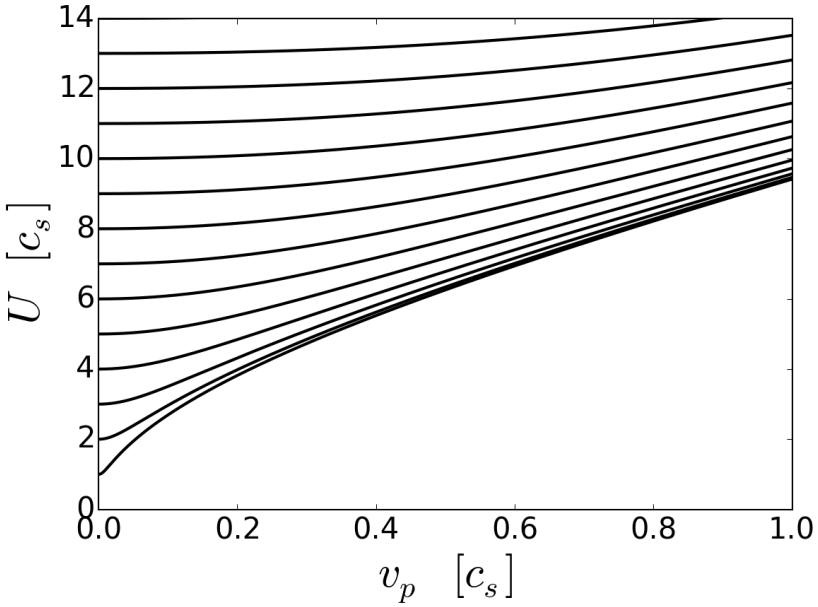

Figure 2-3: U as a function of v_p obtained by solving Equation (2.44) with $m_i/m_e = 1836$ and different U_0.

The relative magnitude of the ion effect and electron effect is equal when

$$\frac{|v_1|}{c_s} = M_{i,e} \equiv \left[\frac{3m_i}{m_e} \frac{\int_{x_1}^{x_2} \left(\frac{e\phi}{T_e}\right)^2 dx}{\int_{x_1}^{x_2} h\left(\sqrt{\frac{e\phi(x)}{T_e}}\right) dx} \right]^{\frac{1}{4}} . \tag{2.47}$$

$M_{i,e}$ is the critical Mach number at which ion jetting effect is comparable to the electron jetting effect. For a shallow electron hole, this velocity is typically a few times c_s. An electron hole traveling at a speed slower than $M_{i,e}c_s$ in the ion frame has strong momentum coupling to ions.

When momentum is injected into the ions, a part of it is going to leak into the electrons through the momentum coupling by the electron hole. We model the momentum injection rate using a background acceleration $\dot{v}_b$ for the ions. Now the momentum balance between

the electron and ion terms gives

$$-m_e n_1 \dot{U} \int_{x_1}^{x_2} h(\chi)\, dx - 3 m_i n_1 (\dot{U} - \dot{v}_b) \int_{x_1}^{x_2} \left(\frac{e\phi}{m_i v_1^2} \right)^2 dx = 0. \tag{2.48}$$

Recognizing that $\dot{U} - \dot{v}_b = -\dot{v}_1$ and we have the following relation

$$\frac{\dot{U}}{c_s} = \left(\frac{M_{i,e}^4 c_s^4}{v_1^4} \right) \frac{\dot{v_1}}{c_s}. \tag{2.49}$$

This relation says that any finite momentum injection rate for ions will cause the electron hole to accelerate through $\dot{v}_1$, resulting in momentum change of electrons. This momentum coupling is proportional to v_1^{-4}, thus it is stronger for slower electron holes in the ion frame.

Equation (2.49) can be further integrated to give

$$\left[\frac{U}{c_s} \right]_A^B = \left[\frac{M_{i,e}^4 c_s^3}{-3 v_1^3} \right]_A^B. \tag{2.50}$$

The initial state is A and the final state is B. This expression shows quantitatively how the hole velocity changes as a function of the ion velocity in the hole frame. Thus the momentum coupling can be revealed through hole "pushing" (decrease in $|v_1|$) and hole "pulling" (increase in $|v_1|$). When the ions are accelerated, the electron hole should accelerate in the same direction as the ions. Pushing and pulling is asymmetric because of the $1/v_1^3$ dependency. It is easy to "push" an electron hole with ion acceleration and more difficult to "pull" it. This also reflects the fact that the coupling strength increases as the electron hole slows down in the ion frame. These predicted phenomena have been explored and quantitatively verified using PIC simulation. The results are presented in the next chapter.

V Conclusions

We have given an analytic treatment of electron hole kinematics by treating the electron hole as a composite object. This theoretical framework of hole kinematics shall be

extensively used in this thesis. The analytic results shall be verified against numerical simulations in Chapter 3.

Chapter 3

Hole tracking Particle-In-Cell simulation

We have presented an analytic theory for electron hole kinematics in Chapter 2. In order to verify our analytic theory and better understand the movement of these phase space electron holes, we use a one-dimensional electrostatic hole tracking Particle-In-Cell simulation code to simulate electron hole motion. It gives a good representation of electron holes in the presence of a relatively strong magnetic field such as in the Earth's magnetosphere. We have fully kinetic ions in our simulation, as the effect of ion dynamics on electron holes is what we are interested in. Simulation of a single solitary electron hole is performed in a modest sized box with open boundary conditions rather than periodic. Electrons and ions have fixed Maxwellian distributions outside the boundaries.

This Chapter is organized in the following way: the hole tracking particle simulation implementation is described in detail in Section I. Section II presents results from hole tracking PIC simulation of electron holes in initial transient and steady state motion. Observations from simulations are compared with an analytic theory. Section III is devoted to numerical experiments where we artificially accelerate ion streams to push or pull the hole. They show important momentum coupling between electron hole and ions. Final summary comments are given in Section IV.

I Hole tracking simulation

Periodic boundary conditions are avoided in this study because the hole can interact with itself through the periodic boundaries, masking the phenomena we are studying. Open boundary conditions for particles are used in our simulation. Particles are free to leave the computation domain and new particles are injected at every time step to represent the Maxwellian distribution of ions and electrons in surrounding plasma. Boundary conditions for potential ϕ are homogeneous with $\phi'(\pm L_x) = \pm\phi(\pm L_x)/\lambda_{\mathrm{De}}$ at the two ends of our simulation domain. These boundary conditions assume that electrostatic potential falls exponentially to zero on the Debye length scale in surrounding plasma. Electron holes move at several times the cold ion sound speed up to electron thermal speed [26] relative to bulk species, while the spatial extent of an electron hole is only a couple of Debye lengths. The total distance traveled by an electron hole for a long run is therefore hundreds or thousands of its own size. A non-periodic simulation of the long term evolution of an electron hole would require thousands of Debye lengths in domain size if a fixed domain is used. An electron hole is sensitive to the statistical noise level in PIC simulation. For N_s particles per computation cell, the statistical noise level on charge density scales like $1/\sqrt{N_s}$ [24] . To have a clear resolution of the hole, we need a large number of particles per Debye length. The combination of a large simulation domain with the requirement of a high number of particles per length would demand excessive computational resources. Simulating a fast moving electron hole using a fixed domain is not efficient.

Therefore, we adopt a more adaptive approach to this problem. A 1-D Particle-In-Cell (PIC) code is used which detects the hole signal and moves the computation domain accordingly so that the hole always stays inside it. We refer to this method as "hole tracking". The major component of hole tracking is a feedback control mechanism. The hole position is detected with an automated search algorithm. At every time step, electric field from the simulation is convolved with a bipolar hole electric field signal. The hole potential in its moving frame is considered to follow approximately the analytic solution

[40]:

$$\phi(x) \;=\; \psi\,\mathrm{sech}^4(\frac{x}{L})\,, \tag{3.1}$$

which gives rise to a bipolar electric field of the form $E(x) = -\frac{4\psi}{L}\tanh(\frac{x}{L})\,\mathrm{sech}^4(\frac{x}{L})$. The typical hole half width L is taken to be $4\lambda_{\mathrm{De}}$. This choice will be justified later in Section II. However, we observe that the choice of L has very little effect on hole tracking results as long as it is in the vicinity of a few Debye lengths. The position of the filtered signal maximum is taken to be where the electron hole is. Hole search algorithm for on board solitary wave detection [32] of space probes is generally more sophisticated than the one presented here. However, our algorithm achieves good performance for the purpose of this study and is easy to implement.

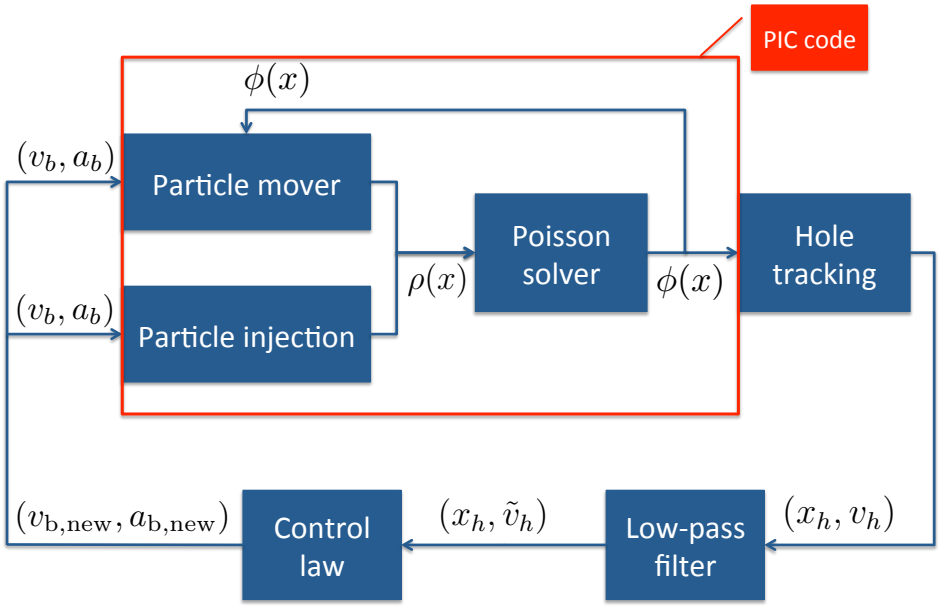

Figure 3-1: Block diagram of hole tracking. $\rho(x)$ and $\phi(x)$ are charge density and potential in the simulation, x_h and v_h are position and velocity of electron hole, $\tilde{v}_h$ is the hole velocity after smoothing is applied, v_b and a_b are velocity and acceleration of simulation box.

Figure 3-1 gives a block diagram of the code's major components. At every time step k, the hole search algorithm gives the position of electron hole $x_h[k]$ relative to the

simulation domain. Lab frame hole velocity $v_h[k]$ is given by $(x_h[k]-x_h[k-1])/\delta t+v_b[k]$, where δt is the time step size of simulation and $v_b[k]$ is the velocity of simulation domain from time step $k-1$ to k. The hole speed calculated this way is subject to high frequency noise. There is statistical noise that is intrinsic to PIC simulation and sampling noise reflecting the fact that hole position can only be evaluated with a finite precision limited by search algorithm spatial grid step. The noise is amplified by taking the numerical time derivative. Consequently, a low-pass filter is required to filter out high frequency noise in measured hole velocity. We adopt a causal Butterworth filter [83] of second order in our simulation. The cutoff frequency is empirically chosen as $0.005\,\omega_{pe}$. The higher the cutoff frequency, the faster the control law will respond to changes in the hole velocity but it will also make it more sensitive to noise. The filtered hole velocity $\tilde{v}_h[k]$ is used as an input of control law to extrapolate the simulation box velocity $v_b[k+1]$ that is required to follow the hole motion. The control law takes both hole velocity $\tilde{v}_h[k]$ and relative position $x_h[k]$ as input for robust feedback control on both velocity and position. The control law can be expressed as

$$\frac{v_b[k+1]-v_b[k]}{\delta t} \;=\; K_1 x_h[k] + K_2(\tilde{v}_h[k]-v_b[k])\,, \tag{3.2}$$

where K_1 and K_2 are respectively control coefficients on position and velocity.

There is a certain freedom in the choice of control coefficients K_1 and K_2. The control law should respond fast enough so that the electron hole does not leave the domain but not induce instability or excessive overshoot. In our simulation, position is normalized to λ_{De} and velocity is normalized to $c_{\mathrm{s}} = \sqrt{\frac{T_e}{m_i}}$. The control coefficients we adopt are then $K_1 = 0.0025\,\omega_{pe}^2$ and $K_2 = 0.75\,\omega_{pe}$. The exact values of K_1 and K_2 have been determined empirically.

The particle pushing and particle injection parts of the PIC code need to take into account the fact that the simulation domain is moving relative to the background plasma and is accelerating. As a consequence of acceleration, the simulation domain is no more an inertial frame of reference. In addition to the force due to the electric field, particles feel an extra acceleration which is the opposite of box acceleration a_b. This term is

included during particle pushing. Background plasma particle distribution relative to simulation domain is now a Maxwellian shifted by minus the box velocity $-v_b$. The velocity distribution of particle fluence across simulation boundaries can be written as

$$|v|f(v)dv \;=\; \frac{n_0|v|}{\sqrt{2\pi}v_{\rm th}} \exp\left[-\frac{(v+v_b)^2}{2v_{\rm th}^2}\right] dv\,, \tag{3.3}$$

where $v_{\rm th} = \sqrt{\frac{T_{i/e}}{m_{i/e}}}$. Eq. (3.3) can be integrated to obtain the total number of particles that need to be injected into the simulation box during a time step of length δt:

$$N_{\rm injection} \;=\; \frac{2n_0 v_{\rm th}\delta t}{\sqrt{2\pi}} \exp\left(-\frac{v_b^2}{2v_{\rm th}^2}\right) + n_0 v_b \delta t \,{\rm erf}\left(\frac{v_b}{\sqrt{2}v_{\rm th}}\right)\,. \tag{3.4}$$

At each iteration, $N_{\rm injection}$ particles are injected following a distribution given by eq. (3.3) for both ions and electrons. The velocity sign of a particle determines which boundary it will be injected from. $N_{\rm injection}$ and eq. (3.3) need to be evaluated at every iteration as v_b is constantly changing as a result of feedback control. A standard *acceptance-rejection method* [84] is implemented to draw random velocities from a distribution expressed by eq. (3.3). The particle injection is considered to be uniform in time. Once injected, they will experience a partial kick and drift. The time duration of this partial particle push is $\theta\delta t$, where θ is a random number uniformly distributed between 0 and 1. The PIC simulation uses a leapfrog integration scheme. As a consequence, velocities of particles are always at half a time step behind their positions. Injection is made consistent with this leapfrog scheme, otherwise, unphysical density perturbations are excited at the simulation boundaries. The standard PIC component of the code is a 1-D electrostatic Particle-In-Cell code, which is referred to as ESPIC [57]. Charge weighting in the code uses a cloud-in-cell [24] approach and Poisson equation is solved by a direct tridiagonal method.

We choose the length of simulation domain to be $48\,\lambda_{\rm De}$ across. By virtue of hole tracking, we do not need a very big domain size to simulate a fast moving hole. However, it should be large enough so that electron holes stay away from boundaries during simulations. In this way, unphysical boundary effects can be avoided. The longest excursion that a hole makes from the center of simulation box is around $15\lambda_{\rm De}$ before it is caught

up by hole tracking in all of our simulations. This choice of domain size guarantees a safety margin from boundaries without being too demanding on computational resources. In order to seed a phase space hole, we initialize the electron distribution with a phase space perturbation. The details of this initialization will be discussed in Section II.

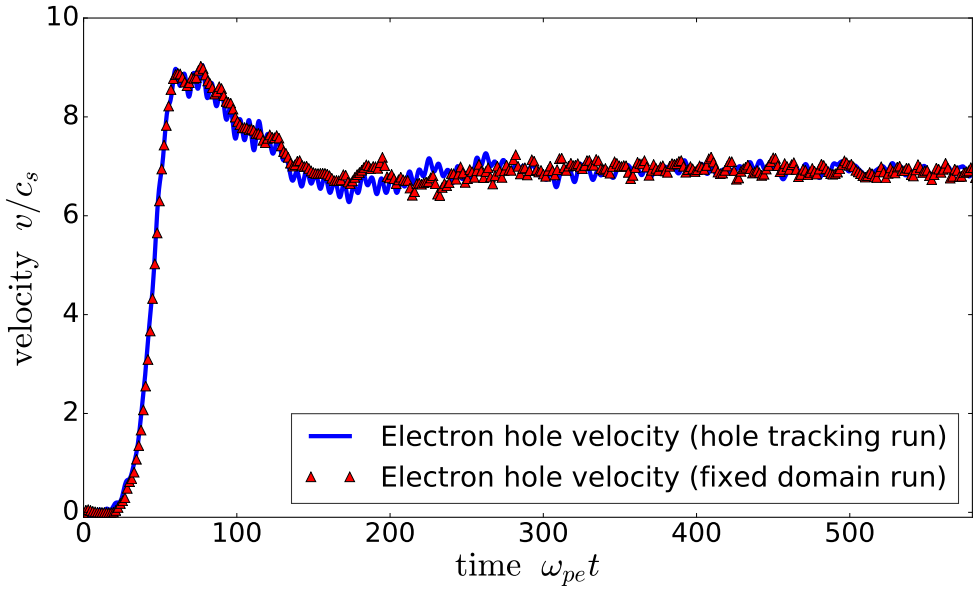

Figure 3-2: Velocity of an electron hole in two different runs, in the fixed domain run, the electron hole hits the boundary at $\omega_{pe}t = 590$ while the hole tracking run can successfully simulate hole motion for a much longer period of time. Velocity data shown here are smoothed using a low-pass filter of cutoff frequency $0.15\,\omega_{pe}$.

Figure 3-2 compares velocity evolution of an electron hole in an ordinary fixed domain PIC run to what we obtain from a hole tracking PIC run using the same initialization setting. The fixed domain run uses a domain which is $192\,\lambda_{\mathrm{De}}$ across with 2×10^8 particles and 4000 spatial cells. The hole tracking run uses a standard $48\,\lambda_{\mathrm{De}}$ domain and thus only requires a quarter as many particles and spatial cells. The agreement between the two runs demonstrates the strength of hole tracking, which is able to resolve hole motion to the same precision with less computational resources. And for longer time durations, the gain would be even greater.

We use $10^7 - 10^9$ particles in our simulations depending on the size of hole we want to simulate. Simulating a shallower hole requires more particles to keep the same signal-

to-noise ratio. The number of cells is chosen to be 10^3 so that we have ~ 20 grid-points per Debye length, making sure that the hole structure is well resolved. The code is fully parallelized to meet the challenge of the large number of particles and time steps required to resolve the phenomena we are interested in. It is observed that a choice of time step size bigger than $0.5/\omega_{pe}$ may drive the simulation numerically unstable. We have explored a range of different time step sizes in our simulation from $0.01/\omega_{pe}$ to $0.4/\omega_{pe}$. The choice of time step size does not affect simulation results if it is below the stability threshold. $\delta t = 0.3/\omega_{pe}$ is the choice we adopt in our simulations.

Feature tracking PIC simulation is a very versatile tool by its nature. A similar approach can be used to investigate the highly resolved dynamics of a wide class of nonlinear plasma phenomena, such as the formation and kinematics of ion holes.

II Initial transient to steady state

There are different ways to seed a phase space hole at the initial stage of a numerical simulation. Schamel derived an analytic solution for electron hole structure in the absence of ion response [40]. This analytic expression of electron distribution function has been used as initialization of hole simulation by Eliasson *et al.*[74]. However, we adopt a different approach in our simulation which can be divided into the following steps:

Step 1: for a given electron density n_0, each electron is initialized with a random position which is uniformly distributed in spatial domain. A *Quiet Start* [24] technique is used for position initialization to make sure that the number of particles in each spatial cell is uniform.

Step 2: for a given electron thermal velocity $v_{\mathrm{th,e}} = \sqrt{\frac{T_e}{m_e}}$, each electron is initialized with a random velocity according to a probability distribution which is a Maxwellian

$$\tilde{f}_{e,0} = \frac{1}{\sqrt{2\pi} v_{\mathrm{th,e}}} \exp\left(-\frac{v^2}{2v_{\mathrm{th,e}}^2}\right) . \tag{3.5}$$

Step 3: for each electron with a position x and a velocity v, a random number α is drawn uniformly between 0 and 1. The velocity is rejected if α is smaller than a predefined value $f_d(x, v)$, where

$$f_d(x, v) \;=\; h_d \exp\left(\frac{-(v - v_d)^2}{2\sigma_d^2}\right) \exp\left(\frac{-x^2}{2\lambda_d^2}\right) . \tag{3.6}$$

This is a bell-shaped function in space and velocity: h_d is the dimple depth which is smaller than 1; σ_d is the dimple velocity width; v_d is the dimple initial velocity and λ_d is the dimple spatial width.

If a velocity is rejected in Step 3, we return to Step 2 and choose a new velocity and then move on to Step 3 to go through another rejection test with this new velocity, iterating until the velocity is accepted. By this process we initialize a dimple in the velocity distribution, localized in position and velocity, but maintain the initial density uniform by enhancing the rest of the electron distribution. Since at each rejection step, the same fraction of velocities (determined by f_d) is rejected, the final distribution is proportional to $\tilde{f_{e0}}(1 - f_d)$. And since the total density is uniform, the normalization gives (a complete proof of the distribution function generated by the rejection method can be found in Appendix A)

$$f_{e,0} \;=\; n_0 \frac{\tilde{f}_{e,0} - \tilde{f}_{e,0} f_d}{1 - \displaystyle\int_{-\infty}^{+\infty} \tilde{f}_{e,0} f_d \, dv} , \tag{3.7}$$

where $f_{e,0}$ is the initial electron distribution in our simulation. This hole seeding process is simple to implement but does not give an initial electron hole potential. However, the initial phase space perturbation will evolve into a self-consistent hole and the electron hole potential will grow out of a uniform background. We refer to the process described above as "uniform density initialization". The uniform density initialization reduces the initial plasma oscillations in the simulation due to charge imbalance.

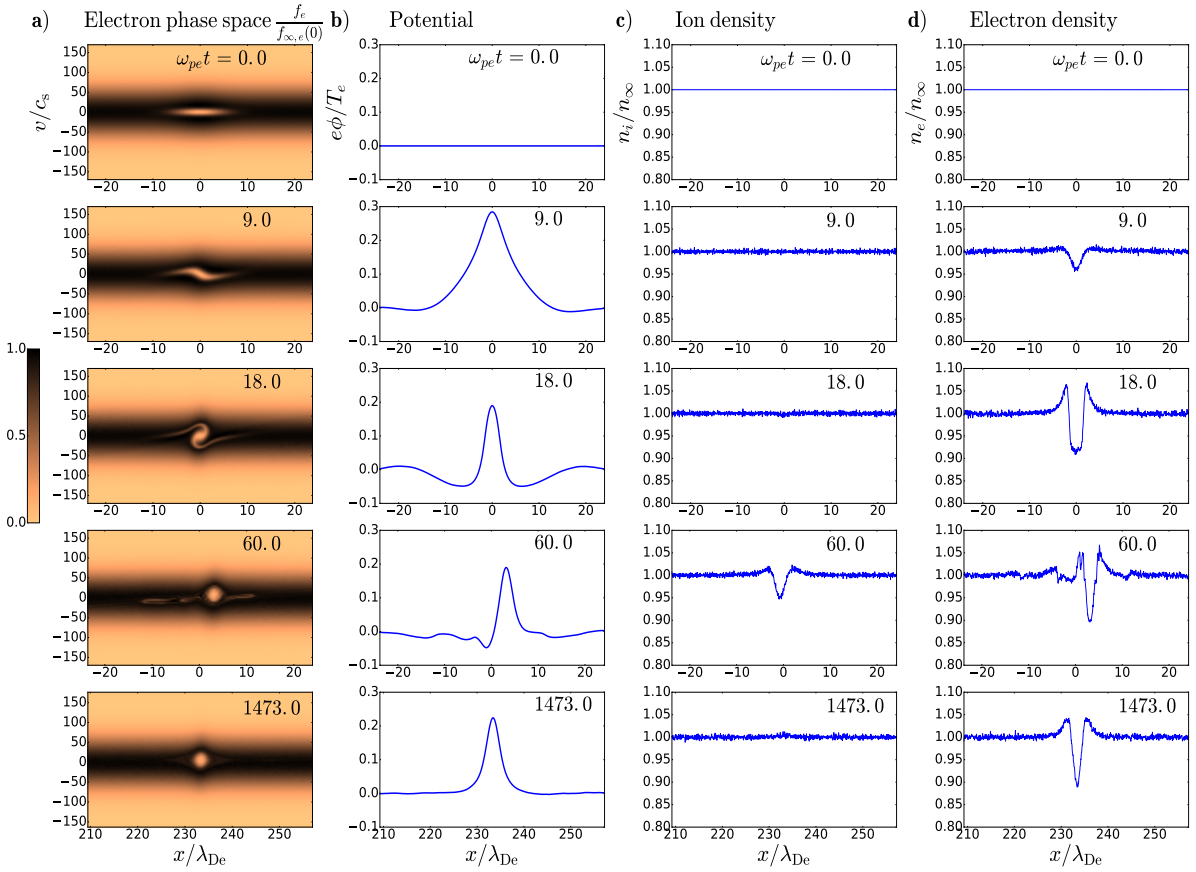

Figure 3-3: a) Normalized electron phase space density contours b) Potential, c) Ion density, d) Electron density. Position x and velocity v are relative to lab frame. The plots shown on the same row are from the same time step in the simulation.

Figure 3-3 shows a run with uniform density initialization and the subsequent transient. The ions are initialized and injected as a Maxwellian distribution with a temperature T_i and a drift velocity of $-1c_s$ in lab frame. The temperature ratio T_e/T_i is 20, mass ratio $m_i/m_e = 1836$. The ions are therefore a cold beam. Initialization parameters for electron phase space density deficit are $h_d = 0.9$, $v_d = 0$, $\sigma_d = 0.15\, v_{\mathrm{th,e}}$, $\lambda_d = 4\,\lambda_{\mathrm{De}}$. The number of particles used in this run is $N_e = N_i = 5.12 \times 10^7$.

The first row of Figure 3-3 shows the initialization of simulation. Notice the initial dimple shape of deficit in electron phase space density. Ion and electron density are equal and uniform by virtue of *Quiet Start*. As a consequence, the initial potential is zero for our initialization. Once simulation starts, the 2nd and 3rd rows of column a) in Figure 3-3 show that the initial perturbation in electron phase space begins to rotate, following phase space flow. Its aspect ratio changes during this process. The same rows of column d) show that a cavity quickly appears in electron density, giving rise to a positive potential pulse which in turn traps the low energy electrons inside. Row 4 shows that after ions have time to respond to this potential ($\omega_{pe}t > (m_i/m_e)^{\frac{1}{2}}$), a cavity of depth $\simeq 5\%$ forms in ion density at the initial position of the hole. The initial ion density perturbation is deeper for a smaller mass ratio ($\simeq 13\%$ for $m_i/m_e = 100$). The electron hole is ejected by this ion density cavity, speeding up during this process. Ions are initialized with a negative drift velocity in the lab frame so that the electron hole is ejected in the positive x direction in this run. Once ejected, the electron hole leaves the ion perturbation and other transient remnants behind it and moves into uniform background plasma. The fully formed self-consistent hole has a shorter spatial width than initialization in this case.

The ion density perturbation eventually moves out of the simulation domain and our simulation tracks the hole into background plasma. The x axis labels in Figure 3-3 give the absolute position in lab frame. The last row shows that the electron hole has traveled more than $200\lambda_{\mathrm{De}}$ but is still well-centered in our simulation domain thanks to hole tracking. A steady state hole can be observed in its rest frame. The potential height of the fully formed electron hole $e\psi/T_e$ is approximately 0.23 for this run, where ψ is the maximum of hole potential. The attached ion-acoustic soliton structure described by Saeki et al. [75] is

not very visible in the steady state hole because the ions are all traveling at approximately $8c_s$ in the hole frame. The average ion kinetic energy in the hole frame is much bigger than $e\psi$. The perturbation in the ion density due to the hole is therefore negligible. The electron density has a deep cavity with excess of electrons around it due to shielding, which is typical of an electron hole [26].

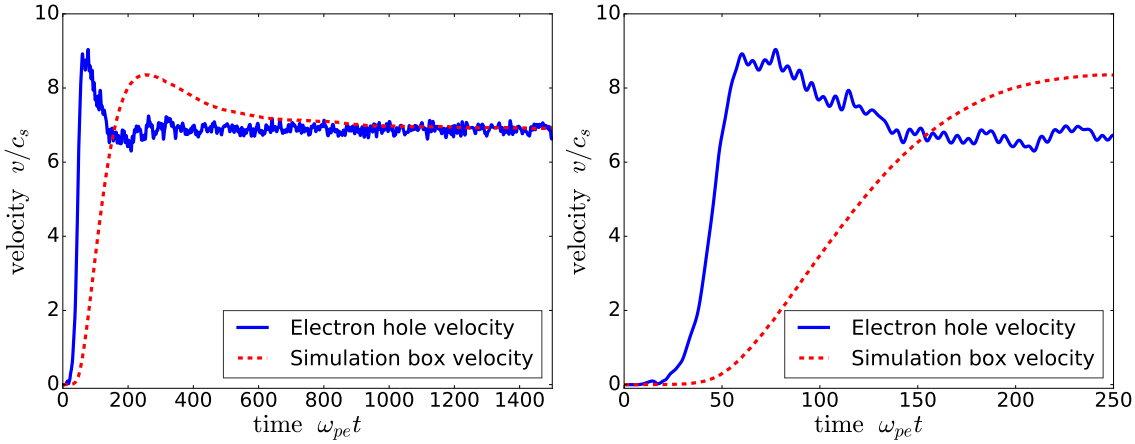

Figure 3-4: Lab frame velocity of electron hole and simulation domain. The plot on the right is a close-up examination of the initial transient for the same run. Hole velocity is smoothed using a low-pass filter of cutoff frequency $0.15\,\omega_{pe}$.

The lab frame velocity of electron hole and simulation domain are plotted in Figure 3-4 for this same run. The feedback control law expressed by eq. (3.2) has both proportional and integral terms of velocity error. As a consequence, both differences in velocity and position between electron hole and simulation domain eventually vanish. We can observe the detailed evolution of electron hole dynamics in Figure 3-4. At the beginning, there is an initial dwell in the hole velocity. It corresponds approximately to the growth time of initial ion density perturbation. Then the electron hole is rapidly accelerated and its velocity reaches $8.9\,c_s$ at $\omega_{pe}t = 60$, this corresponds to the time it leaves the initial ion density cavity. Once moving into uniform background plasma which has a higher ion density, the electron hole is decelerated and its velocity finally stabilizes around $6.9\,c_s$ at $\omega_{pe}t \approx 130$.

An important question arises: what determines the final steady state velocity of an elec-

tron hole? To answer this question, we have performed a detailed quantitative study of this transient acceleration. 50 runs have been carried out using hole tracking PIC for different ion to electron mass ratios m_i/m_e, hole depths ψ and initial ion drift velocity v_i. We take advantage of the flexibility of our code to explore a wide range of parameters. Mass ratio can be easily changed in our simulation. Hole depth is controlled by parameters of uniform density initialization described at the beginning of this section. A deeper dimple depth h_d combined with a bigger dimple velocity width σ_d will give rise to a deeper and wider deficit in initial electron phase space density. It will then evolve into a deeper self-consistent hole. The dimple spatial width λ_d is kept constant at $4\lambda_{\mathrm{De}}$. We shall see that the spatial widths of electron holes in our simulation are close to $4\lambda_{\mathrm{De}}$ despite difference in their depths. A choice of λ_d which is too wide can give rise to multiple holes. We also use $v_d = 0$ for initialization, which means the initial electron phase density deficit has zero average velocity in lab frame. Electrons are initialized and injected with zero drift velocity in lab frame, ions are initialized and injected with a drift velocity v_i in lab frame. This initial drift velocity between ions and electron hole is very important to hole dynamics. Electron to ion temperature ratio T_e/T_i is 20. We have $v_i < v_{\mathrm{th,e}}$ for all our runs so that Buneman type of instability is avoided [85]. Ion-electron acoustic type of instability in principle can be excited for some of these runs but it has very weak growth rate [86] and is not observed in our simulation. No disruptive plasma instabilities are observed in the runs presented and hole tracking works properly. Each run consists of a hole tracking simulation of 10000 time steps with a step size of $0.3/\omega_{pe}$. All of the runs except for two use $N_i = N_e = 2.56 \times 10^7$ as the total number of particles. It becomes more and more computationally challenging as we try to push the runs to shallow hole limit. The two shallowest holes we have explored require 10^9 particles for successful hole tracking.

Each run is examined individually to determine when exactly the hole enters steady state motion. Steady state quantities such as hole depth and hole velocity are calculated by taking their average value over 1000 time steps right after the steady state is reached. Figure 3-5 gathers the results from these runs we have done using different parameters.

U is the velocity of an electron hole in the initial rest frame of ions. Therefore, we have $U = v_h - v_i$ with our initialization process and its initial value U_0 is equal to $-v_i$. $v_p/c_s = \sqrt{2e\psi/T_e}$ is the normalized ion passing velocity at hole center, which is proportional to the square root of hole depth.

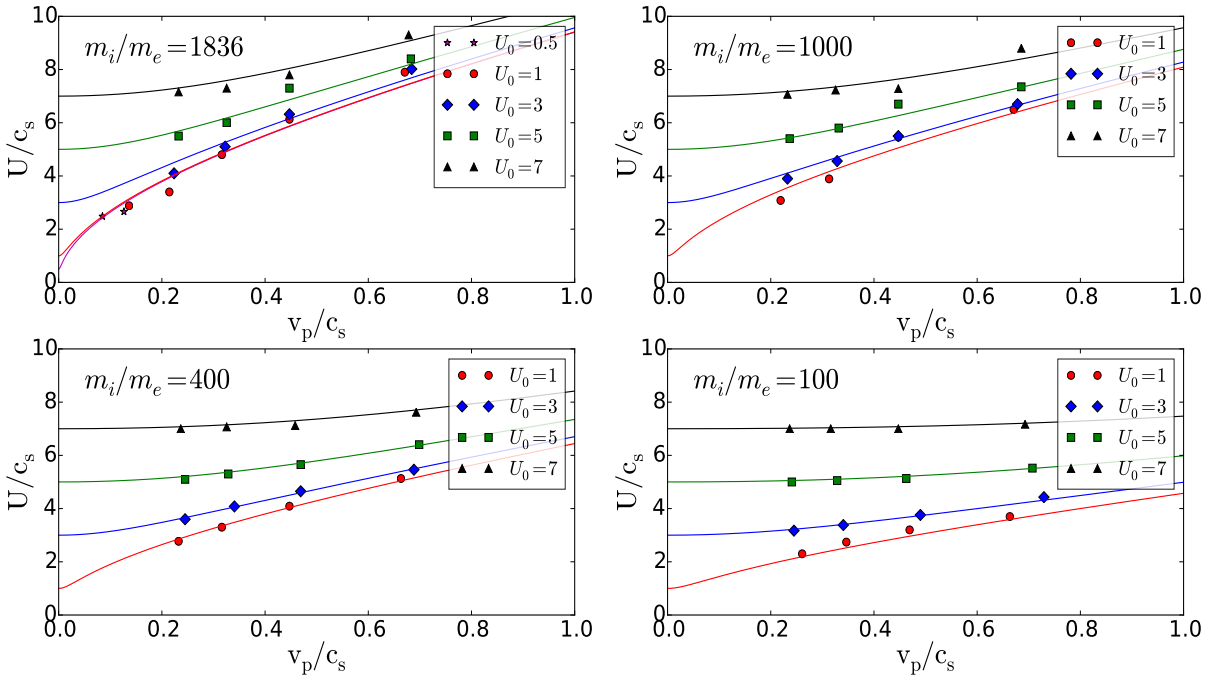

Figure 3-5: Steady state hole velocity in initial ion rest frame as a function of mass ratio, steady state hole depth and initial hole velocity, solid curves in each plot are obtained from hole momentum conservation theory.

Our hole momentum conservation theory presented in Chapter 2 predicts the hole kinematics. The theory assumes no specific hole structure and can be applied to electron holes in our simulation. It is our goal here to compare simulation results with our analytic theory. For an electron hole generated from uniform density initialization, the theory provides an explanation for the initial hole acceleration. The change in ion momentum due to hole potential growth must be balanced by change in hole velocity. This initial transient acceleration is governed by Equation (2.44)

$$-\frac{m_e}{m_i}h(\frac{1}{\sqrt{2}}\frac{v_p}{c_s})\dot{U} - \frac{3}{4}\frac{v_p^4}{U^4}\dot{U} + \frac{v_p^3}{U^3}\dot{v_p} = 0\,, \tag{3.8}$$

where the function h for holes that move slowly compared with electron thermal speed ($v_h \ll v_{\mathrm{th,e}}$) is

$$h(\chi) \;=\; -\frac{2}{\sqrt{\pi}}\chi + \left[(2\chi^2-1)e^{\chi^2}\,\mathrm{erfc}(\chi)+1\right]\,. \tag{3.9}$$

Eq. (3.9) comes from the expression of electron momentum rate of change when an electron hole is present in electron distribution function and a detailed derivation can be found in Chapter 2. $v_p = \sqrt{2e\varphi/m_i}$ the ion passing velocity is a function of the growing potential $\varphi(t)$. The initial conditions are $U(t=0)=U_0$ and $\varphi(t=0)=0$. Thus, we have $U(v_p=0)=U_0$. Eq. (3.8) can then be solved for U as a function of v_p using a standard Runge-Kutta scheme for different initial values of U_0 and mass ratio m_i/m_e. Solutions are plotted as solid lines in Figure 3-5. The theory predicts that the velocity of an electron hole in ion rest frame follows $U(v_p)$ curve when its depth grows. In the lab frame, this would mean that uniform density initialization with an ion drift velocity $-U_0$ gives rise to a steady state hole of velocity $U(v_p)-U_0$ when its potential grows from 0 to $e\psi = \frac{1}{2}m_i v_p^2$. Figure 3-5 shows quite good agreement between simulation results and theoretical $U(v_p)$ solutions. In terms of change in hole velocity $\Delta U = U(v_p)-U_0$, the quantitative agreement between theory and simulations is within 20%. The cases where the prediction of analytic theory deviates from simulation results are the ones with small U_0. Our theory assumes a short-transit-time approximation for ions. The transit time of ions through the hole region needs to be much shorter than the typical acceleration timescale $U/\dot{U}$. This approximation is barely adequate when the ion velocity is slow relative to the hole and important initial acceleration occurs, which corresponds to the runs with small U_0.

The steady state hole we obtain in our simulation is a very stable coherent structure whose amplitude hardly decays over thousands of electron plasma periods if the noise level in the simulation is kept low by using a sufficient number of particles. Schamel derived an analytic solution [40] for the shape of a slowly moving ($v_h \ll v_{\mathrm{th,e}}$) steady state electron hole in the limit of small amplitudes ($e\psi/T_e \ll 1$). Electron holes in our simulations generally satisfy these two conditions. The form of this solution is given in eq. (3.1). The

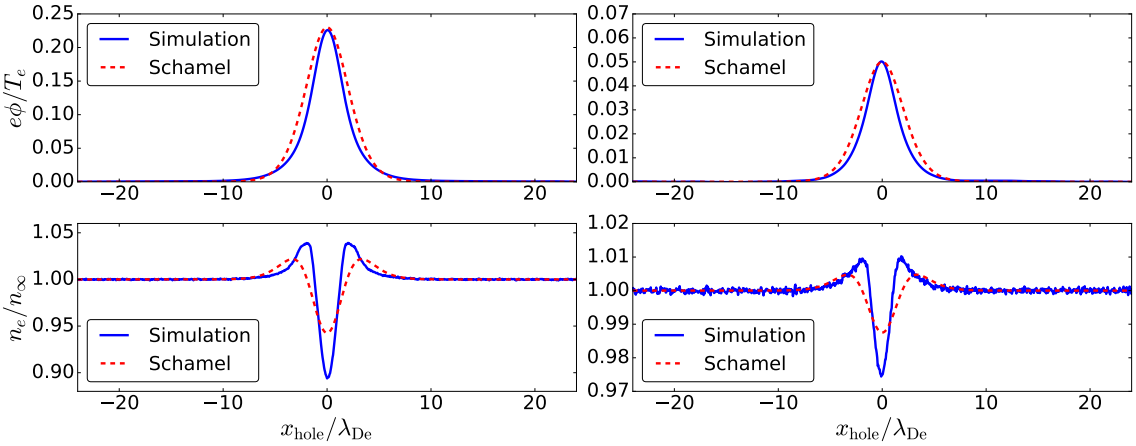

Figure 3-6: Potential and electron density profile for two steady state electron holes of different depths and speed compared with Schamel's analytic solution, $e\psi = 0.23T_e\,, v_h = 6.9c_s$ on the left and $e\psi = 0.05T_e\,, v_h = 3.8c_s$ on the right, simulation results are averaged over 100 time steps to reduce fluctuations.

hole half width L is given by the nonlinear dispersion relation [26]:

$$L = \left(-\frac{32}{Z'_{\rm Re}(v_h/\sqrt{2}v_{\rm th,e})}\right)^{\frac{1}{2}} \lambda_{\rm De}\,. \tag{3.10}$$

$Z_{\rm Re}$ is the real part of plasma dispersion function [87]. For $|x| \ll 1$,

$$Z_{\rm Re}(x) \approx -2x\left[1 - \frac{2}{3}x^2 + \frac{4}{15}x^4 + ...\right]\,. \tag{3.11}$$

These expressions yield $L \to 4\lambda_{\rm De}$ when $v_h/v_{\rm th,e} \to 0$. For $v_h = 6.9\,c_s$, $L \approx 4.05\lambda_{\rm De}$ by evaluating eq. (3.10). Schamel's analytic expression and the steady state holes in our simulation are plotted in Figure 3-6.

Analytic curves are generated with $L = 4\lambda_{\rm De}$ and the maximum of potential measured in the simulation is taken as ψ. The analytic expression for electron density is derived by taking the second derivative of Schamel's expression for hole potential. The steady state holes in our simulations are slightly narrower than Schamel's analytic form and also have a deeper dip in electron density. Nevertheless, $L \simeq 4\lambda_{\rm De}$ holds for holes of different depths and using Schamel's form in hole search algorithm is an acceptable approximation and yields good performance. For the hole tracking simulation, we can

find the electron distribution in the rest frame of an electron hole. The velocity and position of an electron in the simulation domain are the same as their values in the hole frame when the hole is in steady-state motion. We compare the distribution from our simulation with Schamel's solution. Figure 3-7 shows the value of hole-frame electron distribution function f_e as a function of total energy, $\mathcal{E} = \frac{1}{2}m_e v^2 - e\phi(x)$, normalized to its separatrix value $f_s = f_{\infty,e}(0)\exp(-v_h^2/2v_{\mathrm{th,e}}^2)$. Electrons that have negative energy in

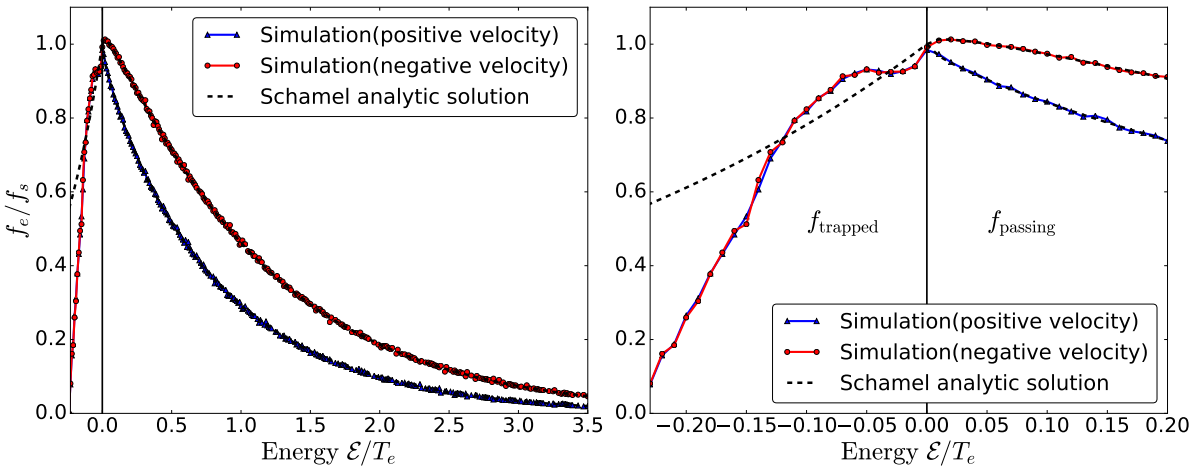

Figure 3-7: Electron distribution on constant energy $\mathcal{E}$ orbit in hole frame, $e\psi = 0.23T_e$, $v_h = 6.9c_s$. Dashed line is Schamel's solution for an electron hole with the same depth traveling at the same speed relative to bulk electrons.

hole frame are trapped and those with positive energy are passing. Schamel's solution [40] is given by

$$f_e(x,v) = \begin{cases} f_{\infty,\mathrm{e}}(0)\exp\left[-\dfrac{m_e(\sigma\sqrt{2\mathcal{E}/m_e}+v_h)^2}{2T_e}\right] & \text{if } \mathcal{E}>0 \\ f_{\infty,\mathrm{e}}(0)\exp(-\dfrac{v_h^2}{2v_{\mathrm{th,e}}^2})\exp(-\dfrac{\beta\mathcal{E}}{T_e}) & \text{if } \mathcal{E}<0 \end{cases} \tag{3.12}$$

where $\sigma = \operatorname{sign} v$ and β is the trapped particle parameter. It can be shown that for a slowly moving shallow hole [26], β is given by

$$\beta \simeq 1 - \frac{15}{16}\pi^{1/2}(e\psi/T_e)^{-1/2}\,. \tag{3.13}$$

For $e\psi = 0.23T_e$, the value of β is -2.47.

Schamel's solution coincides with a Maxwellian distribution shifted by minus the hole velocity $-v_h$ for passing electrons. In the trapped region, Schamel's solution is Maxwell-Boltzmann shaped. The distribution obtained from our simulation agrees with Schamel's solution for passing electrons; but the trapped distribution is different. The deeply trapped orbits in our simulation are less populated than in Schamel's solution, which explains why the electron hole in our simulation is narrower at its center. The trapped electron distribution in a steady-state hole is determined by its initialization. We can generate electron holes with different shapes of f_{trapped} by changing the shape of function f_d in our initialization. Our analytic kinematic theory is not affected by the exact structure of an electron hole as it applies to generic electron holes with global charge neutrality.

Hole tracking simulation enables us to visualize directly trapped electrons in a steady state hole. As the simulation domain is moving at the same speed as the electron hole, electrons that are on passing orbits are quickly exchanged out of the domain and only the ones on trapped orbits stay and travel with the solitary wave. Our simulation tracks the step at which a particle is injected. The middle panel of Figure 3-8 shows the phase space density of electrons from initialization $f_{e,t=0}$ normalized to current electron phase space density f_e in a steady state hole of potential profile $\phi(x)$. The velocity half-width of densely populated orbits by initial particles in phase space is around $28c_s$ at hole center, which is approximately equal to $v_{p,e} = \sqrt{\frac{2e\psi}{m_e}}$ for $e\psi = 0.23T_e$ as expected. Trapped orbits are therefore almost entirely populated by electrons from initialization. These electrons are trapped from the beginning of the simulation and stay inside the simulation domain with the hole.

In the run with a relatively high U_0 ($U_0 > 5c_s$), the ions are less perturbed by the initial hole potential as a result of their high relative speed to the hole. This initialization gives a smaller initial transient speed-up as shown in Figure 3-5. In this case, possible formation of more than one electron hole from our initialization is observed. When this happens, one principal hole is formed which is much deeper than all others. The attraction and coalescence behavior of holes with similar velocity reminiscent of the previous

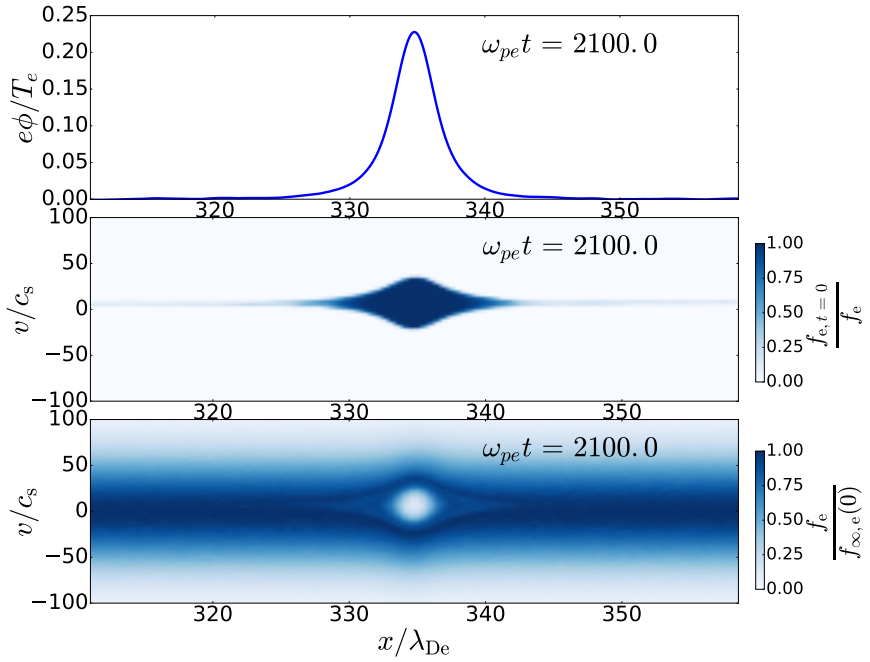

Figure 3-8: The hole potential (top panel), the relative phase space density of initial electrons (middle panel) and the normalized electron phase space density (bottom panel) at time $\omega_{pe}t = 2100$, the hole has a lab frame velocity of $6.9c_s$, x and v are relative to lab frame.

experimental and numerical investigations [88] [89] [90] is observed in our simulations. Our hole tracking algorithm tracks the most significant hole signal which is given by the deeper hole. Figure 3-9 shows a case of two electron holes moving in the same direction with similar speed for a long period of time ($\sim 1000/\omega_{pe}$) until they get close to one another and subsequently their main bulk parts coalesce to one due to mutual attraction. The smaller hole experiences "tidal" deformations [89] during the interaction and a part of it eventually escapes. A transient increase of magnitude $\sim 0.5c_s$ is observed in the velocity of the principal hole when it interacts with the smaller one. The interaction is relatively smooth because of the disparities between the sizes of two holes.

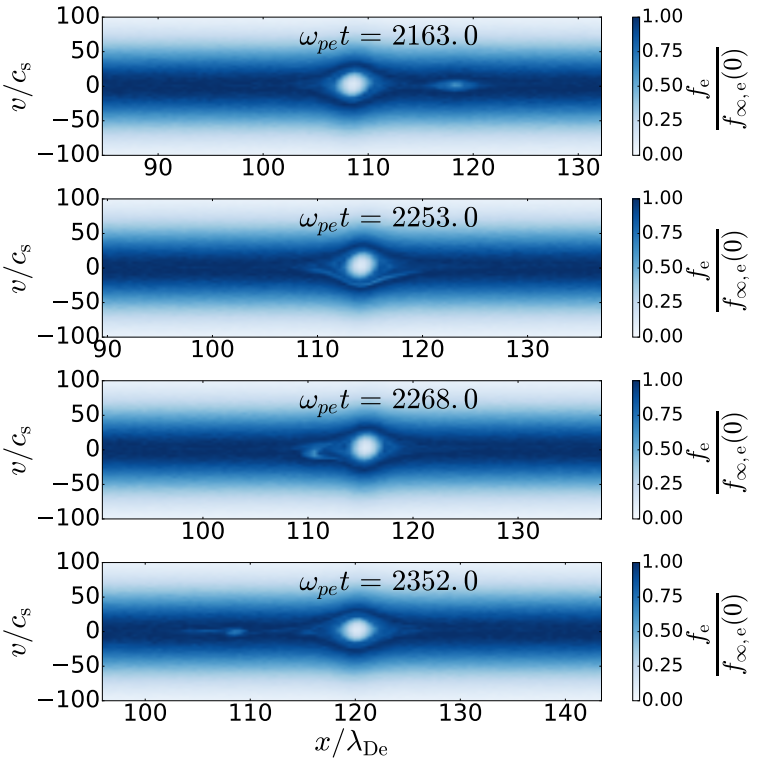

Figure 3-9: Coalescence of electron holes of different size in our simulation, a shallow hole is followed by a much deeper one and they eventually partly coalesce. A piece of the shallower hole is sprayed out. This run is performed with $U_0 = 7c_s$,$m_i/m_e = 1836$ and the deeper hole at the center of simulation domain has a depth of $e\psi = 0.23T_e$, the shallower hole has a depth of $e\psi = 0.03T_e$.

III Hole pushing and pulling

One of the big advantages of the hole tracking simulation is in that it allows us to study kinematics of an electron hole with slight deviation from its steady state without worrying about losing it from the simulation domain. This feature enables us to probe momentum coupling between ions and an electron hole in quasi steady state. In the theory developed by Dupree et al., the only momentum exchange [70] between electron hole and ions is through ion reflection by hole potential. This would imply that an electron hole can only "feel" a change in ion momentum when ions begin to reflect from hole potential. For beam-like ions and a shallow electron hole, this only happens when the drift velocity of ions is within several $v_{\mathrm{th,i}}$ in the rest frame of the electron hole. However, our numerical experiments contradict this conclusion. We clearly see ion influence on electron hole kinematics even when there are effectively zero reflected ions.

The way we investigate this problem is through applying an artificial acceleration to ions. The acceleration is applied by adding an artificial linear background potential to the electrostatic potential that is used to move ions but not electrons in the particle mover of PIC code. The linear artificial potential gives rise to a constant field which accelerates ions at a constant rate. At the same time, ions are injected from a distribution of background ions which is accelerating at the same rate. The overall effect is that all ions experience a constant background field in addition to the field that electrons experience. When ions are accelerated so that their velocity approaches the hole velocity, this is called "pushing". The opposite case is called "pulling". We artificially accelerate ions only after the hole is in steady state. The value of this artificial acceleration is chosen to be on the order of $c_s\omega_{pe}/1000$. The velocity of an ion in the rest frame of a steady state hole is typically a few times the sound speed c_s in our simulation. The hole spatial width is generally a few times λ_{De} the Debye length. The time it takes for an ion to transit through hole region is therefore on the order of $50/\omega_{pe}$. During this time, the change in ion velocity due to this artificial background acceleration is around $0.05c_s$, which is much smaller compared to its velocity in hole frame. This choice of artificial acceleration guarantees that short transit-time approximation is valid for ions in these runs.

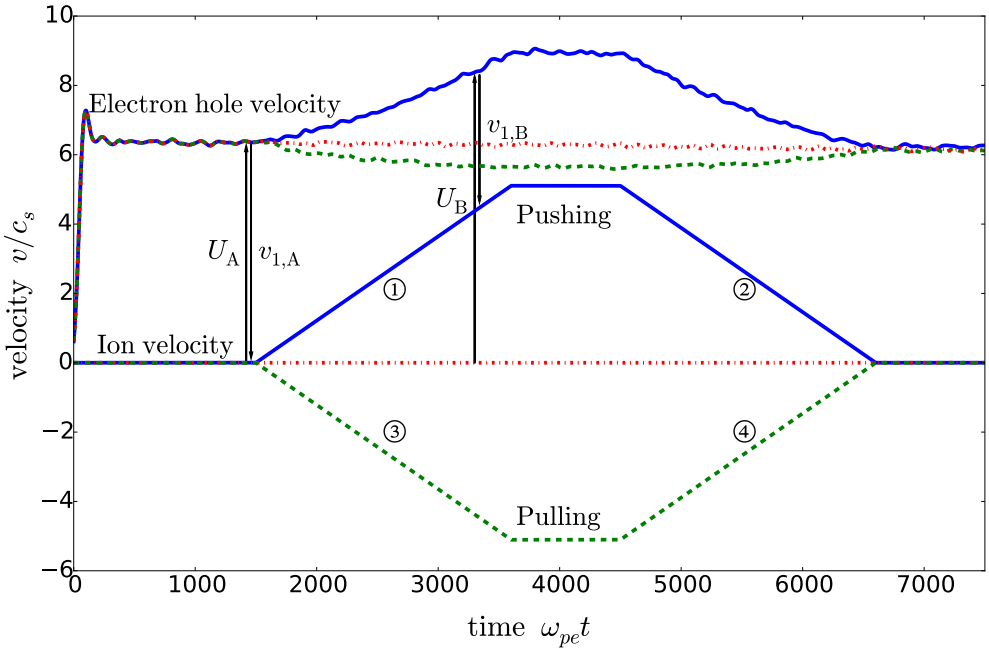

Figure 3-10: Hole velocity response to artificial ion acceleration, $T_e/T_i = 20$, $e\psi = 0.1T_e$. Solid line is the "pushing" run and dashed line is the "pulling" run. Dashed dot line is a reference run where no artificial acceleration is applied.

Figure 3-10 shows the electron hole velocity evolution in our hole pushing and pulling runs. In the pushing run, constant artificial ion acceleration is applied from $\omega_{pe}t = 1500$ to $\omega_{pe}t = 3600$(phase ①), which accelerates the drift velocity of ions from 0 to $5c_s$ in its initial rest frame. Then acceleration of the same magnitude but opposite sign is applied from $\omega_{pe}t = 4500$ until $\omega_{pe}t = 6600$ (phase ②) to bring the ions back to their initial velocity. The pulling run is the same except that we exchange the order of the two acceleration phases (③④ instead of ①②). Contrary to what Dupree's theory would predict, the velocity of the electron hole changes immediately after the artificial acceleration is applied to ions before any ions are reflected by the hole potential. Moreover, the change in hole velocity is always in the same direction as ion acceleration. Results in Figure 3-10 also show a strong asymmetry in pushing and pulling. For the same initial velocity of the electron hole in ion rest frame, pushing gives larger hole velocity response than pulling. Both pulling and pushing are reversible.

We need the theory of hole momentum conservation presented in the previous chapter

to understand the phenomena we see in our simulations. The theory can be generally applied to cases where one or both species in plasma are subjected to a uniform background force. Hole pushing and pulling can be described by the Equation (2.49) relating initial and final states A and B during the process of pushing or pulling:

$$\frac{\Delta U}{c_s} = \frac{U_{\rm B} - U_{\rm A}}{c_s} = \frac{M_{ie}^4}{3}\left(\frac{1}{|v_{1,\rm B}/c_s|^3} - \frac{1}{|v_{1,\rm A}/c_s|^3}\right), \tag{3.14}$$

where M_{ie} is the Mach number of hole velocity at which electron momentum rate magnitude is equal to ion momentum rate magnitude. $M_{ie}^4/3$ is given by

$$\frac{M_{ie}^4}{3} = \frac{m_i}{m_e}\left[\int_{x_1}^{x_2}\left(\frac{e\phi(x)}{T_e}\right)^2 dx \Big/ \int_{x_1}^{x_2} h\left(\sqrt{\frac{e\phi(x)}{T_e}}\right) dx\right]. \tag{3.15}$$

$\phi(x)$ is the electron hole potential profile with x_1 and x_2 denoting its spatial extent (theory assumes that ϕ and its derivative vanish at x_1 and x_2). The special function h is defined by eq. (3.9). The definitions of $U_{\rm A}$, $U_{\rm B}$, $v_{1,\rm A}$, $v_{1,\rm B}$ are illustrated by arrows in Figure 3-10 for a pushing run. U is the velocity of an electron hole in the initial rest frame of ions and v_1 is the drift velocity of ions in the hole frame.

The theory assumes that the hole does not change its shape during pushing or pulling, so $M_{\rm ie}$ is a constant for a hole of given potential. Eq. (3.14) can give us some important insight on how pushing and pulling would behave according to the theory. First, the influence of artificial ion acceleration on hole velocity U is instantaneous. Any finite change in v_1 will result in change in hole velocity. Second, pushing and pulling are asymmetric. There is no limit on how much a hole can be pushed in its velocity, while pulling is limited by $-M_{ie}^4/3|v_{1,\rm A}/c_s|^3$. Third, pushing and pulling are independent of path and thus reversible. These properties agree qualitatively with what we see in our simulations.

A quantitative comparison between the theory and our simulations is shown in Figure 3-11. The theoretical curves of $\Delta U(v_{1,\rm B})$ shown in solid lines are calculated from eqs. (3.14) (3.15). The reference velocity $v_{1,\rm A}$ is chosen as the velocity of ions in the hole

frame right before the artificial acceleration is applied to ions. Its value is determined by the initialization that generates the steady state hole. The calculation of multiplication factor $M_{ie}^4/3$ depends on the exact hole potential profile $\phi(x)$. Since $h(\chi) \to \chi^2$ as $\chi \to 0$, the value of $M_{ie}^4/3$ is $\sim (m_i/m_e)(e\psi/T_e)$ for the holes in our simulations which are relatively shallow. We use the potential output from our simulation to calculate a more precise value. The interval $[x_1, x_2]$ over which the integrals are performed in eq. (3.15) is determined with the electric field. The theory assumes that hole electric field vanishes at its boundaries. Thus we can practically consider x_1 and x_2 to be the two positions where the electric field in our simulation first changes its sign outside the hole center. Once the electric field begins to oscillate on its thermal level, we are in background plasma. The values of integrals in eq. (3.15) are evaluated numerically at each time step of acceleration and its average value is used in eq. (3.14). The theory is compared with

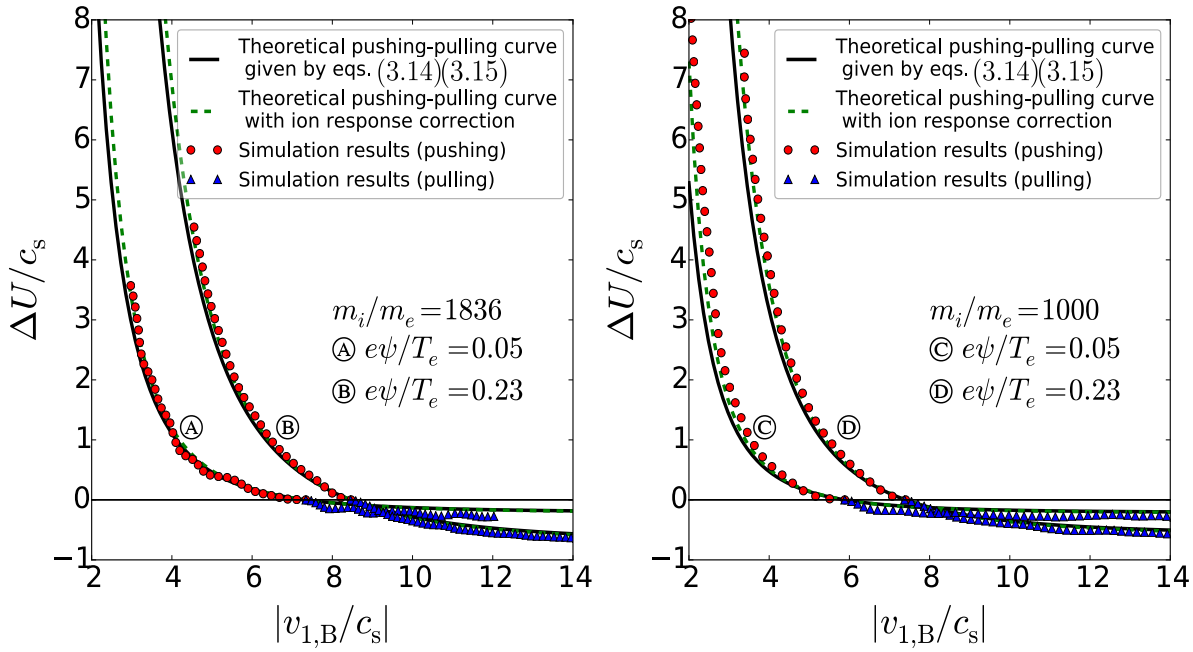

Figure 3-11: Hole pushing and pulling runs for holes of different depths using two different mass ratios. The value of ψ is the average value during acceleration. $T_e/T_i = 20$, $N_i = N_e = 2.56 \times 10^7$.

simulation results in Figure 3-11. The simulation velocity is just the hole velocity obtained from the hole tracking algorithm. The hole velocity is filtered by a low-pass filter of cutoff

frequency $0.005\omega_{pe}$. The ions are beam-like and their drift velocity is considered to follow the constant acceleration that is artificially applied. This assumption is adequate as the momentum imparted by ions to electrons is a fraction smaller than $\sim m_e/m_i$ of the total momentum injected by the background artificial field.

Numerical experiments show good agreement with the theory. The agreement is further improved by including ion density variation due to hole potential in the theory. This modified solution is plotted in dashed lines in Figure 3-11. The original theory presented in Chapter 2 assumes no ion density perturbation in the derivation of trapped electron density from charge balance. However, when an electron hole is pushed, the relative velocity of ions in the hole frame decreases. The ion density accumulation inside the hole, which is an ion-acoustic response attached to the hole in Saeki et al.'s terminology [75], becomes more important as ions are slowed down by hole potential. If we account for ion density variation to order $(c_s/v_1)^2(e\phi/T_e)$, then $h(\chi)$ is replaced by $h(\chi)-(c_s/v_1)^2(e\phi/T_e)$ in the derivation of eq. (3.14). This leads to the modified solution:

$$\left[\frac{U}{c_s}\right]_A^B = M_{ie}^4\left[\frac{1}{K^2(v_1/c_s)}+\frac{1}{2K^3}\ln\left|\frac{v_1/c_s-K}{v_1/c_s+K}\right|\right]_A^B, \tag{3.16}$$

where $K = \int_{x_1}^{x_2}(e\phi(x)/T_e)\,dx/\int_{x_1}^{x_2} h\left(\sqrt{(e\phi(x)/T_e}\right)dx$ is a constant. K is evaluated in the same way as $M_{ie}^4/3$ by performing numerical integration over $[x_1, x_2]$. For shallow holes, we have $K \simeq 1$ as $e\psi/T_e \ll 1$. This correction is more important for small $|v_1|$.

In deriving function h, we assume an electron hole situated near the top of the electron distribution. This approximation is no longer adequate when a hole is pushed to an important fraction of $v_{th,e}$. It is also observed in our simulations that the depth and shape of an electron hole changes slightly ($< 5\%$) during pushing and pulling. This can have several important implications. The derivation of eq. (3.14) assumes no change in the hole potential. Hole growth and shrinkage will induce hole velocity change as we see in the initial transient. This effect is ignored in our analysis. The change and fluctuations of hole potential in our simulations also make it difficult to evaluate accurately $M_{ie}^4/3$. We observe 5% to 10% fluctuations in its value at different time steps. It is the average

value that is used in Figure 3-11.

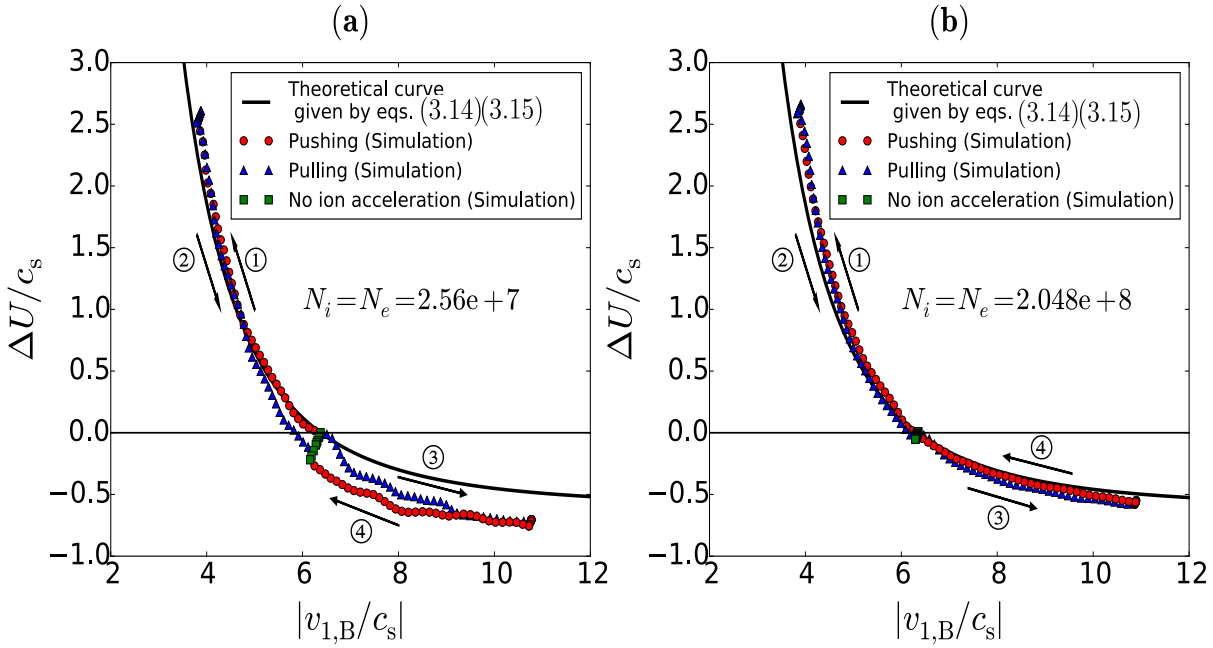

Figure 3-12: Illustration of reversibility and hysteresis in pushing and pulling. (a) Pushing, pulling and no ion acceleration runs showing spontaneous hole velocity decay and hysteresis. (b) The same runs as (a) with eight times as many particles, the spontaneous velocity decay and hysteresis are reduced by using more particles. The number of computation cells is 1000 in these runs and the domain length is $48\lambda_{\text{De}}$ across. $T_e/T_i = 20$, $e\psi = 0.1T_e$.

In hole pushing and pulling experiments, we are trying to resolve small changes in hole velocity to the extent that statistical noise in our simulation needs to be treated carefully. We observe slow spontaneous decay in the velocity of a steady-state hole during long time hole tracking simulation. This effect is shown in Figure 3-12. The three runs in plot (a) correspond to the pushing-pulling-back run(① ②), the pulling-pushing-back run (③ ④) and the reference run with no artificial ion acceleration presented in Figure 3-10. Notice the decay in hole velocity even when there is no ion acceleration at all. The change is in diagonal direction for the run with no ion acceleration because $U = -v_1$ when ion drift velocity stays constant. The same effect in pushing and pulling runs leads to hysteresis, which can also be seen in plot (a). This slow hole velocity decay is reduced by using more particles in the simulation. The runs shown in the plot (b) of Figure 3-12

exhibit less velocity decay by virtue of using more particles. Pushing-pulling process is also more reversible, which agrees better with our theory predictions. This effect can be explained by detrapping of trapped electrons in an electron hole due to statistical fluctuations in the PIC simulation. The depth of an electron hole $e\psi$ slowly shrinks when the marginally trapped orbits are intermittently connected to background plasma by fluctuating electric fields. Its velocity U decreases as a consequence of its shrinking size. Eq. (3.8) relates the depth of an electron hole to its velocity. For the run with no ion acceleration shown in plot (a), the hole depth $e\psi$ decreases from $0.1025T_e$ at $\omega_{pe}t = 1500$ to $0.098T_e$ at $\omega_{pe}t = 7500$. The decrease in hole velocity calculated from eq. (3.8) for the amount of depth shrinkage is $\Delta U_{\text{Decay}} \simeq -0.1c_s$. The actual decay in velocity observed in our simulation is $\Delta U_{\text{Decay}} \simeq -0.2c_s$. Though small in magnitude, this effect is important for pulling runs as ΔU_{Decay} can be an important fraction of the predicted ΔU. By taking into account this correction, the agreement between our theory and simulation in high $|v_1|$ limit is within $\pm 10\%$.

Eq. (3.14) gives no lower limit on how small $|v_1|$ can get by pushing the hole. This is unphysical as ions will be reflected by hole potential if $|v_1| < v_{p,i}$, where $v_{p,i} = \sqrt{2e\psi/m_i}$ is the marginal ion passing velocity. The modified solution given in eq. (3.16) shows that ions cannot approach the hole velocity closer than $|v_1| = Kc_s$ with $K > 1$. In our simulations, we observe that instability occurs before $|v_1|$ can get close to this limit. Ion density is perturbed in the case of instability and the electron hole can be disrupted if pushed further. The exact nature of this instability is beyond the scope of this chapter. A complete treatment of this instability is given in Chapter 4.

IV Summary

In this chapter, we introduce a new way of simulating a moving electron hole by tracking its motion. The full dynamics of electron hole interacting with ions are studied quantitatively using this computer simulation technique in both transient and steady-state regimes. We find that an electron hole generated using a uniform density initialization

approach can be accelerated to several times the ion sound speed by initial ion density perturbation. The final steady-state velocity reached by electron hole depends on ion-to-electron mass ratio, hole depth and the initial hole velocity in the ion frame. Dynamical coupling of a steady-state hole and ions is investigated by applying a slow artificial acceleration to ions. The velocity of an electron hole reacts instantaneously to changes in ion momentum. An electron hole can be pushed or pulled in velocity by artificially imposed ion acceleration. Pulling and pushing are asymmetric. Simulations are compared with the newly developed analytic theory of hole momentum conservation. Good qualitative and quantitative agreement is presented in this study.

Chapter 4

Plasma electron hole velocity oscillatory instability

The early theoretical research of electron holes (EHs) neglected the ion dynamics for simplicity and considered them as a uniform neutralizing background [40]. Later, Saeki *et al.* [75] showed using PIC simulations that an EH can be disrupted by ions when its velocity is slower than the ion sound speed. Eliasson *et al.* [74] reported that a standing EH in the ion frame can be ejected from the ion density cavity it created and is attracted to ion density maxima. The recent observations of "slow" EHs also suggest a more important role for the ions. EHs traveling with the ion sound speed c_s have been recently reported at a magnetic reconnection site [91] and the magnetopause [92] measured by the Cluster spacecrafts, a velocity much slower than what was frequently observed before ($\sim v_{\mathrm{th,e}}$). The authors suggested that Buneman instability resulting from dynamic reconnecting current sheets generated these slow EHs. Schamel gave an upper limit [26] for the speed of the EHs by a structural existence argument. How slow can an EH travel? Saeki *et al.* [75] briefly touched upon this question by deriving the nonlinear dispersion relation using the Sagdeev pseudo-potential method. However, the nonlinear dispersion relation is based on the existence of a stationary solution of which the *stability* is not guaranteed. An EH can experience different kinds of instabilities in higher dimensions, e.g. the whistler instability [56] in the strongly magnetized case and the transverse instability [53] in the

weakly magnetized case. These instability mechanisms do not involve ion dynamics. Ion-acoustic wave radiation from a solitary structure in plasma has been studied in the case of Langmuir soliton [93] and ion hole [94]. Dyrud *et al.* [76] reported the observation of ion-acoustic waves emitted from a chain of electron holes in PIC simulations. Dokgo *et al.* [95] reported the generation of coherent ion-acoustic solitary waves from an EH as it propagates from a lower plasma density region to a higher plasma density region. In this chapter, we show that the ion dynamics is important for the stability of an EH even in the 1-D equilibrium, causing an oscillatory velocity instability for slow electron holes to decay into ion-acoustic waves. This discovery suggests that the solitary solutions constructed using the Sagdeev pseudo-potential method can be unstable to small perturbations when the ion dynamics becomes important.

The instability mechanism discussed in this chapter is closely related to the velocity, and thus to the kinematics of an EH. The EH kinematics has been studied in Chapter 2 treating the EH as a composite object. Chapter 3 shows our theory is successful in explaining quantitatively the dynamics of EHs observed in PIC simulations, such as the transient self-acceleration and the "hole pushing/pulling" effect due to steady-state hole momentum coupling to the ions. In this chapter, we extend our theory to the frequency domain and use multiple-scale analysis to give a mathematically rigorous treatment of the instability.

This chapter summarizes the research work that is published in reference [82]. It is organized as follows: in Section I, we report the observational details of this instability from our PIC simulation. In Section II, a first principle analytic calculation using hole kinematics theory is presented, the instability boundary, unstable mode frequency and growth rate are analytically derived and compared with the PIC simulation observation. Section III justifies the eigenmode ansatz that we have adopted in this chapter. In Section IV, we are going to discuss the nonlinear stage of the instability and its potential implication in space plasma. Section V is the summary.

I PIC observation of the instability

The simulations are performed using a 1-D electrostatic PIC code with fully kinetic ions, which is designed to study highly-resolved EH dynamics. A solitary EH is created in our simulation using an electron phase-space density deficit as the initial seed [81]. The thermal noise in our PIC simulation is controlled by using more than 10^6 particles per cell. There are ~ 10 cells per Debye length to resolve the detail of an EH. We performed box simulation of a solitary EH with an open boundary computation domain that can self-consistently follow the EH motion [81] (also see Chapter 3). The size of the computation domain is only $\sim 50\lambda_{\rm De}$ by virtue of using hole tracking. Our hole-tracking PIC allows us to study the detail of hole motion with reasonable computational cost. Once a steady-state EH is obtained in our simulation, we apply an artificial slow ion acceleration to slowly "push" the EH with ions so that it slows down in the ion frame. This "pushing" process has been demonstrated to be quasi steady-state and reversible [81]. We discovered when performing these "pushing" runs that there is a limit velocity of the EH in the ion frame, below which the EH becomes unstable. This threshold velocity is well above other physical limits of the system such as the ion reflection velocity limit.

An example of the instability observed in our PIC simulation is presented in Figure 4-1. For this particular case, we initialized the EH with a Gaussian shaped phase-space density deficit defined as

$$f_d(x,v) \;=\; h_d \exp\left(-\frac{(v-v_d)^2}{2\sigma_d^2}\right)\exp\left(-\frac{x^2}{2\lambda_d^2}\right), \tag{4.1}$$

with $h_d = 0.9$, $v_d = -3c_s$, $\sigma_d = 0.15v_{\rm th,e}$ and $\lambda_d = 4\lambda_{\rm De}$. The initial electron distribution function is given by

$$f_e(x,v) \;=\; \frac{n_\infty}{\sqrt{2\pi}v_{\rm th,e}}\exp\left(-\frac{v^2}{2v_{\rm th,e}^2}\right)\frac{1-f_d(x,v)}{1-\displaystyle\int_{-\infty}^{+\infty}\frac{1}{\sqrt{2\pi}v_{\rm th,e}}\exp\left(-\frac{v^2}{2v_{\rm th,e}^2}\right)f_d(x,v)\,dv}. \tag{4.2}$$

The normalization factor in the expression of $f_e(x,v)$ ensures that the initial electron

density is spatially uniform in order to have a relatively "quiet" initialization (see Chapter 3). An EH forms after this initial electron distribution function is allowed to evolve self-consistently as we have shown in Chapter 3. Initially, the cold ion stream of temperature $T_i = T_e/20$ has a mean velocity of $-10c_s$ in the lab frame. We slowly accelerate the ions towards the EH velocity with an acceleration of $0.008\omega_{pe}c_s$ to continuously explore different EH velocities in the ion frame. On the top left, we show the characteristic solitary potential structure of a stable EH that extends over several Debye lengths. In a steady-state EH, the ions are slowed down by the hole potential and their density is slightly higher inside the EH. This ion density compressional pulse is the ion-acoustic response attached to the phase-space EH described by Saeki *et al.* [75] It is clearly visible inside the stable EH shown on the left. When the EH slows down in the ion frame, the oscillation amplitude in its velocity begins to grow once its speed is slower than a threshold value. The EH potential and the ion density at a later time step ($\omega_{pe}t = 2925$) after the instability has grown are presented on the right for comparison. The EH keeps its potential shape while its velocity oscillates. The down stream ion density becomes unsteady as the velocity oscillation amplitude grows. Unsteady ion density perturbations are emitted from the EH after the instability onset. The perturbations propagate in the ion frame with the ion sound speed, mainly in the opposite direction to the EH velocity. The EH velocity was obtained from the hole-tracking module in our code [81] and a low pass filter has been applied to it to filter out the statistical noise. The "hole pushing" can be turned off at any moment before the instability onset and the EH will enter a stable steady-state with the same velocity, but not after the EH is slower than the threshold velocity.

A similar phenomenon also happens in a plasma with counter-streaming ions. We initialize [1] an EH at rest ($U = 0$ initially) in the lab frame on top of the electron distribution with counter-streaming ions traveling at $\pm v_i$ in the laboratory frame. We do not need to apply any special technique such as the hole pushing and hole tracking. The initialization will naturally favor the formed EH to stay at $U = 0$ and we can do a regular

[1] This initialization corresponds to $h_d = 1$, $v_d = 0$, $\sigma_d = 0.98v_{\mathrm{th,e}}$ and $\lambda_d = 4\lambda_{\mathrm{De}}$.

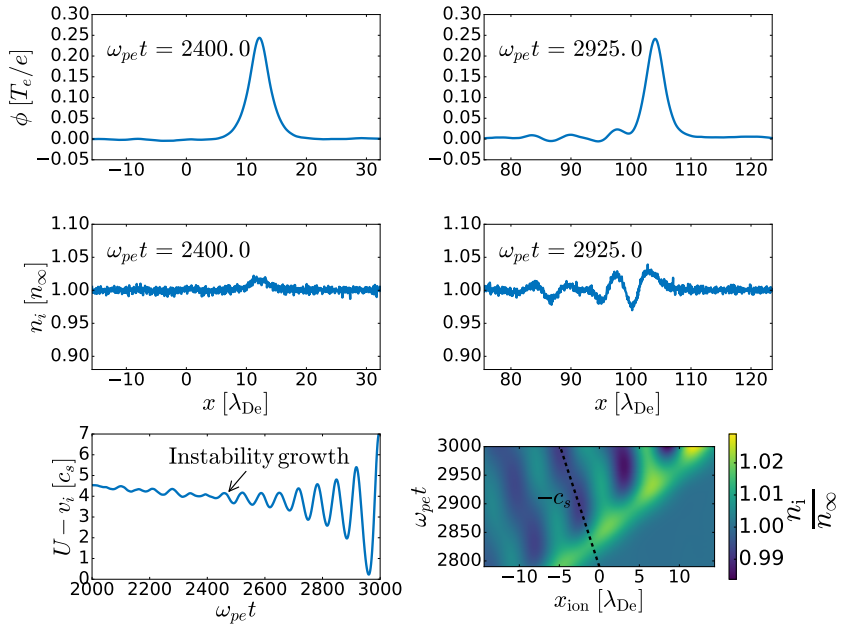

Figure 4-1: The hole potential (first row) and the ion density (second row) before (left) and after (right) the instability growth. Bottom left panel shows the EH velocity in the ion frame and the bottom right panel shows the ion density perturbations due to the EH and the instability. The bulk electrons are Maxwellian at rest in the laboratory frame and $T_e/T_i = 20$.

box simulation of the EH with a static domain. We observe that there is a minimum value of v_i below which the system is unstable. A case of the observed instability is shown in Figure 4-2. The self-consistently formed EH is unstable. Perturbations in its velocity grow exponentially. Ion-acoustic perturbations grow and are emitted from both sides of the EH because the ions are counter-streaming. The simulation was performed with warm ions $T_i = T_e$, corresponding to a case where ion-acoustic waves are strongly Landau damped, ion counter-streaming type of instability and Buneman instability are ruled out by the simulation parameter setting. For this particular case shown in Figure 4-2, using a slightly higher $v_i = 7c_s$ can stabilize the instability. We shall see later in Section II that from the stability point of view, the counter-streaming ion case is equivalent to the single ion stream case.

We have repeated the numerical experiments with different parameter settings. It is observed that for the same EH, the instability only depends significantly on the relative

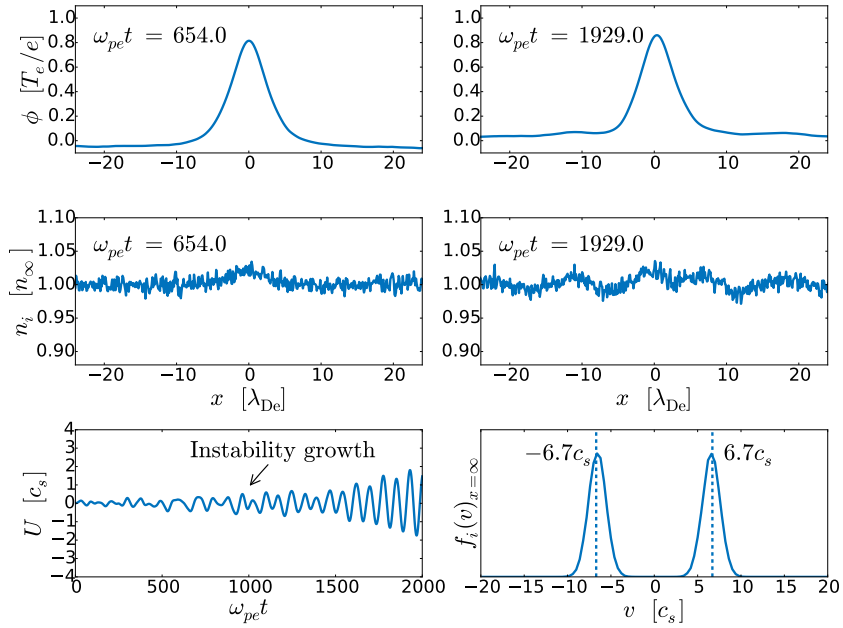

Figure 4-2: The hole potential (first row) and the ion density (second row) before (left) and after (right) the instability growth in a plasma with counter-streaming ions. Bottom left panel shows the EH velocity and the bottom right panel shows the ion distribution function with counter-streaming Maxwellians. The ion streams have an average velocity of $\pm 6.7 c_s$ and $T_i = T_e$. The bulk electrons are Maxwellian at rest in the lab frame.

velocity between the EH and the ions $U - v_i$. The EH velocity with respect to the bulk electrons U and the relative velocity drift between the ions and the bulk electrons v_i alone have no significant influence on the instability onset and its growth. We have performed simulations with an electron-to-ion temperature ratio T_e/T_i from 20 down to 0.5. We observe that this velocity instability clearly persists in the regime $T_e \leq T_i$, where ion-acoustic type of instability is unexpected. A hotter ion population leads to a higher threshold value of $U - v_i$ and damped ion-acoustic wings. We shall discuss the finite ion temperature effect on the instability in detail in Section II.

It is clear that a self-consistent solitary solution with a complete ion response can be constructed in the case of instability using the Sagdeev pseudo potential or the BGK approach. Our PIC code actually does this by solving Poisson's equation numerically. However, once this steady-state solitary solution is allowed to evolve in time, it becomes unstable. The characteristics of this instability does not fit into any existing linear plasma

stability theory. The core of this problem is very nonlinear because of the strong particle trapping nonlinearity in the EH. We need to adopt a new approach to analyze its mechanism.

II Hole velocity stability deduced from kinematics

II.1 Frequency response of the momentum rate of change

To analyze this instability, we first consider the steady-state solution of an EH. The steady-state EH potential $\phi(x)$ is considered to extend from x_a to x_b in the hole frame, with x_a and x_b taken to be far away from the center of the hole so that both $\phi(x)$ and its derivatives vanish at these limits: $\phi(x_a) = \phi(x_b) = \phi'(x_a) = \phi'(x_b) = 0$. The ions and the bulk electrons are assumed to be Maxwellian at rest in the lab frame with their background density being denoted by n_∞. The EH moves at a velocity U in the lab frame. The sign convention is such that $U < 0$. We first adopt a cold beam approximation for ions and the finite ion temperature effect will be treated later on in this chapter. The distance is normalized to λ_{De}, ϕ is measured in T_e/e, the velocity is in units of $c_s = \sqrt{T_e/m_i}$ and the time is normalized to $1/\omega_{pi}$. The schematic of a steady-state EH is shown in Figure 4-3. The steady-state velocity and density of the ions in the hole frame can be derived from conservation of energy and the continuity equation:

$$\begin{cases} v_0(x) = -\dfrac{U}{|U|}\sqrt{U^2 - 2\phi(x)} \\ n_0(x) = n_\infty \dfrac{|U|}{\sqrt{U^2 - 2\phi(x)}} \end{cases} \tag{4.3}$$

In Chapter 2, we have established that the motion of an EH is governed by the momentum conservation when acceleration or growth are steady. The parallel momentum contained in the electromagnetic field can be ignored for a field-aligned solitary electrostatic structure. The momentum balance is between the two components of the plasma: $\dot{P}_i + \dot{P}_e = 0$, where $\dot{P}_{i/e}$ represents the total inertial-frame momentum rate of change for the two species. Here we extend the analysis to oscillatory acceleration or the frequency

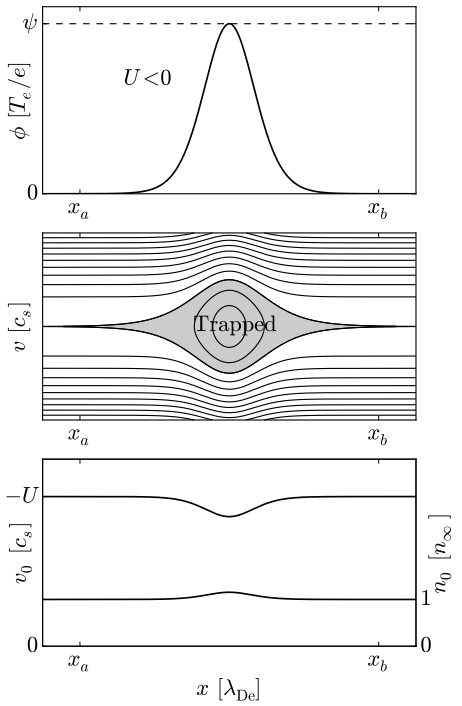

Figure 4-3: Schematic of a steady-state EH with the associated phase-space structure and the ion response. Top: EH potential, middle: electron phase space orbits, the trapped orbits are shaded. Bottom: the steady-state ion velocity v_0 and density n_0 in the hole frame.

domain. To a first approximation, we are going to assume that the EH potential $\phi(x)$ in the hole frame does not change and there is a small perturbation in the hole velocity represented by $\dot{U} \sim \mathrm{Re}(\exp[-i\omega t])$. Our ansatz corresponds to an eigenmode which results in a displacement of the steady-state equilibrium. It is sometimes referred to as the Goldstone mode of a soliton solution [96]. This ansatz of eigenmode is justified through a linearized Vlasov-Poisson approach in Section III. The frequency ω we consider is much lower than the average passing electron transit frequency. The passing electrons feel a nearly constant hole acceleration during their transit (this amounts to a short-transit-time approximation for electrons), so that we can use the previous expression of $\dot{P}_e$ in Chapter 2 for $U \ll v_{th,e}$ with a full ion response correction

$$\dot{P}_e \;=\; -m_e \dot{U} n_\infty \int_{x_a}^{x_b} h(\sqrt{\phi(x)}) + 1 - \frac{|U|}{\sqrt{U^2 - 2\phi(x)}}\, dx, \tag{4.4}$$

where $h(\chi) = -\frac{2}{\sqrt{\pi}}\chi + (2\chi^2 - 1)e^{\chi^2}\,\mathrm{erfc}(\chi) + 1$. The ion response correction accounts for the ion density accumulation inside the EH. The exact shape of the trapped electron distribution does not appear in our approach. The total number of trapped electrons inside the EH is deduced from global charge neutrality of the solitary structure. Our ansatz treats the trapped electron phase-space structure as a holistic object.

The ions however feel an oscillating potential when they transit the hole region. The ion momentum change can be decomposed into two different terms, a momentum outflow term $\dot{P}_{io}$ at the boundaries and a contained momentum term $\dot{P}_{ic}$. The conservation of momentum needs to be evaluated at a fixed time. Let subscripts s and f refer to the starting time and the final time, a and b refer to the positions x_a and x_b in the hole frame and bar denote velocities in the inertial frame (the unbarred velocities are evaluated in the hole frame, notice that prime was adopted to denote the inertial frame quantity in Chapter 2). An ion particle enters the control volume at x_a when $t = t_s$ exits at x_b when $t = t_f$. At $t = t_f$, we have therefore

$$\begin{aligned}\frac{\dot{P}_{io}}{m_i} &= n_{bf}v_{bf}\bar{v}_{bf} - n_{af}v_{af}\bar{v}_{af} \\ &= n_{bf}v_{bf}\bar{v}_{bf} - n_{bf}v_{bf}\bar{v}_{af} + n_{bf}v_{bf}\bar{v}_{af} - n_{af}v_{af}\bar{v}_{af} \\ &= n_{bf}v_{bf}(\bar{v}_{bf} - \bar{v}_{af}) + (n_{bf}v_{bf} - n_{af}v_{af})\bar{v}_{af}.\end{aligned} \tag{4.5}$$

The term $\bar{v}_{bf} - \bar{v}_{af}$ represents the "jetting" effect [80] due to the hole acceleration. In the comoving frame of the EH, the equation of motion of a single ion particle admits a first integral

$$\frac{1}{2}v^2 + \phi(x) + \int \dot{U}v\,dt = \text{Constant}. \tag{4.6}$$

Applying this conservation law between the time t_s and t_f, we have

$$v_{bf}^2 - v_{as}^2 + 2\int_{t_s}^{t_f} \dot{U}v\,dt = 0. \tag{4.7}$$

The equilibrium velocity for $\dot{U} = 0$ is $v_0(x) = -\frac{U}{|U|}\sqrt{U^2 - 2\phi(x)}$. The idea is to do an expansion around the equilibrium orbit. Perturbation expansion gives $v = v_0 + v_1$ and

$|v_1|/|v_0| \sim |t_{ab}\dot{U}/U| \ll 1$ where $t_{ab} = t_f - t_s$ is the single ion transit time. In principle, the amplitude of the hole acceleration can be made arbitrarily small to satisfy this ordering. To leading order in the small parameter $t_{ab}\dot{U}/U$, we expand the difference between the ion velocity exiting and entering the hole region $v_{bf} - v_{as}$

$$\begin{aligned} v_{bf} - v_{as} &= \frac{-2}{v_{bf} + v_{as}} \int_{t_s}^{t_f} \dot{U} v \, dt \\ &\simeq \int_{x_a}^{x_b} \frac{\dot{U}(t(x, x_b))}{U} \, dx. \end{aligned} \tag{4.8}$$

where $t(x, x_b) = t_f - \int_x^{x_b} \frac{du}{v(u)}$ is an intermediate time. To keep notations simple, we will omit its explicit form while keeping in mind that unless stated otherwise, $\dot{U}$ and v are evaluated when the considered ion particle is at the position indicated by the dummy variable of the integration. Taking into account the change in the hole velocity between t_s and t_f, we have

$$\begin{aligned} \bar{v}_{bf} - \bar{v}_{af} &= v_{bf} - v_{as} + \int_{t_s}^{t_f} \dot{U} \, dt \\ &\simeq \int_{x_a}^{x_b} (\frac{1}{U} + \frac{1}{v_0}) \dot{U} \, dx. \end{aligned} \tag{4.9}$$

Thus we have obtained the "jetting" effect due to the acceleration of the EH to the relevant order and the first term in Eqn. (4.5) can be evaluated as

$$n_{bf} v_{bf} (\bar{v}_{bf} - \bar{v}_{af}) \simeq n_\infty \int_{x_a}^{x_b} (-1 - \frac{U}{v_0}) \dot{U} \, dx. \tag{4.10}$$

To calculate the second term in Eqn. (4.5), we need to know how the ion flux changes with $\dot{U}$. We apply the continuity of an ion fluid element from x_a to x_b

$$n_{as} v_{as} \delta t_{as} = n_{bf} v_{bf} \delta t_{bf}, \tag{4.11}$$

where δt_{as} and δt_{bf} are two infinitesimal time durations for the same ion fluid element to enter and exit the control volume. They are related by the derivative of transit time t_{ab}

with respect to the starting time t_s: $\delta t_{bf} \simeq \delta t_{as}(1 + \frac{dt_{ab}}{dt_s})$. Thus, to leading order,

$$\begin{aligned} n_{bf}v_{bf} - n_{af}v_{af} &= n_{bf}v_{bf} - n_{bf}v_{bf}\frac{\delta t_{bf}}{\delta t_{as}}\frac{v_{af}}{v_{as}} \\ &= n_{bf}v_{bf}\left[1 - \frac{\delta t_{bf}}{\delta t_{as}}(1 + \frac{v_{af} - v_{as}}{v_{as}})\right] \\ &\simeq n_{bf}v_{bf}(-\frac{dt_{ab}}{dt_s} - \frac{v_{af} - v_{as}}{v_{as}}), \end{aligned} \tag{4.12}$$

where we used the constancy of inflow density $n_{as} = n_{af} = n_\infty$ and that dt_{ab}/dt_s is of the same order as $(v_{af} - v_{as})/v_{as}$. The derivative dt_{ab}/dt_s describes the non-constancy of the ion transit time due to the hole acceleration. It can be evaluated to the first order using $t_{ab} = \int_{x_a}^{x_b} \frac{dx}{v}$ and the conservation law of Eqn. (4.6)

$$\begin{aligned} \frac{dt_{ab}}{dt_s} &= \frac{d}{dt_s}\int_{x_a}^{x_b} \frac{1}{v}\, dx \\ &= \int_{x_a}^{x_b} -\frac{1}{v^3}\frac{\partial(v^2/2)}{\partial t_s}\bigg|_x dx \\ &= \int_{x_a}^{x_b} -\frac{1}{v^3}\frac{\partial}{\partial t_s}\bigg|_x \left(v_{as}^2/2 - \phi(x) - \int_{x_a}^{x} \dot{U}\, dx_1\right) dx \\ &\simeq \int_{x_a}^{x_b} \frac{1}{v^3}[-U\dot{U}(t_s) + \int_{x_a}^{x} \ddot{U}\, dx_1]\, dx. \end{aligned} \tag{4.13}$$

$\ddot{U}$ is the rate of change of hole acceleration, or the jerk, evaluated when the ion particle is at x_1. We used interchangeably $\partial/\partial t_s$ and $\partial/\partial t$ as $dt = dt_s(1 + \mathcal{O}(t_{ab}\dot{U}/U))$ for x_1 fixed. We can further get rid of the $\dot{U}(t_s)$ term in Eqn. (4.13) performing integration by parts

$$\begin{aligned} \dot{U}(t_s) - \frac{1}{U}\int_{x_a}^{x} \ddot{U}\, dx_1 &= \dot{U}(t_s) - \frac{1}{U}\int_{x_a}^{x} v\, d\dot{U} \\ &\simeq \dot{U}(t_s) - \left[\frac{\dot{U}(t)v_0(x)}{U} - \frac{\dot{U}(t_s)v_0(x_a)}{U}\right] + \frac{1}{U}\int_{x_a}^{x} \dot{U}\frac{dv_0}{dx_1}\, dx_1 \\ &\simeq -\frac{\dot{U}(t)v_0(x)}{U} - \frac{1}{U}\int_{x_a}^{x} \frac{\dot{U}\phi'(x_1)}{v_0(x_1)}\, dx_1. \end{aligned} \tag{4.14}$$

We used here $dv_0/dx_1 = -\phi'/v_0$, where ϕ' is the spatial derivative of ϕ. Combining Eqns.

(4.13) and (4.14), we can evaluate the right hand side of Eqn. (4.12) as

$$\begin{aligned} n_{bf}v_{bf}(-\frac{dt_{ab}}{dt_s}-\frac{v_{af}-v_{as}}{v_{as}}) &\simeq n_\infty(-U)\int_{x_a}^{x_b}-\frac{1}{v_0^3}\Big[-U\dot{U}(t_s)+\int_{x_a}^{x}\ddot{U}\,dx_1\Big]-\frac{1}{U}\frac{\dot{U}}{v_0}\,dx \\ &\simeq n_\infty\int_{x_a}^{x_b}\frac{U^2}{v_0^3}\Big[\frac{\dot{U}v_0}{U}+\frac{1}{U}\int_{x_a}^{x}\frac{\dot{U}\phi'}{v_0}\,dx_1\Big]+\frac{\dot{U}}{v_0}\,dx \\ &= n_\infty\int_{x_a}^{x_b}\frac{U}{v_0^2}\dot{U}+\frac{U}{v_0^3}\Big(\int_{x_a}^{x}\frac{\dot{U}\phi'}{v_0}\,dx_1\Big)+\frac{\dot{U}}{v_0}\,dx. \end{aligned} \tag{4.15}$$

We choose the inertial frame as the instantaneous rest frame of the EH so that $\bar{v}_{af} = v_{af} \simeq -U$, we have a final expression for the total rate of momentum outflow by using Eqns. (4.10) and (4.15). It is first order in $t_{ab}\dot{U}/U$, thus linear in $\dot{U}$

$$\dot{P}_{io} = m_i n_\infty \int_{x_a}^{x_b}(-1-2\frac{U}{v_0}-\frac{U^2}{v_0^2})\dot{U}-\frac{U^2}{v_0^3}\Big(\int_{x_a}^{x}\frac{\dot{U}\phi'}{v_0}\,dx_1\Big)\,dx. \tag{4.16}$$

Now we proceed to calculate the rate of change of ion momentum contained inside the control volume between x_a and x_b in the same inertial frame at $t = t_f$

$$\dot{P}_{ic} = m_i\int_{x_a}^{x_b}\frac{\partial(nv)}{\partial t}\,dx + m_i\dot{U}\int_{x_a}^{x_b} n\,dx. \tag{4.17}$$

The derivation of $\dot{P}_{ic}$ is similar in spirit to what we have shown for $\dot{P}_{io}$ but involves heavier algebra, we leave it to the Appendix B. The final result which is the same order as $\dot{P}_{io}$ in Eqn. (4.16) can be expressed as

$$\dot{P}_{ic} = -m_i n_\infty \int_{x_a}^{x_b}\int_{x_a}^{x}\frac{U}{v_0^3}\int_{x_a}^{x_1}\dot{U}(t(x_2,x))\phi''(x_2)\,dx_2\,dx_1\,dx. \tag{4.18}$$

We combine Eqs. (4.16) and (4.18) to give a full expression for $\dot{P}_i = \dot{P}_{io} + \dot{P}_{ic}$. The conservation of total momentum gives an eigenmode equation for ω:

$$\dot{P}_i(\omega) + \dot{P}_e(\omega) = 0. \tag{4.19}$$

The imaginary part of ω determines the stability of the corresponding eigenmode.We

apply Nyquist stability analysis [97] to determine the stability.

The equation can be rewritten as $\dot{P}_i/\dot{P}_e+1=0$, where $\dot{P}_i/\dot{P}_e$ is given by a long integral expression

$$\begin{aligned}\frac{\dot{P}_i}{\dot{P}_e}(\omega,U,\phi) = -\frac{m_i}{m_e}\Bigg[&\int_{x_a}^{x_b}\left(-1-2\frac{U}{v_0(x)}-\frac{U^2}{v_0^2(x)}\right)\exp\left(i\omega\int_x^{x_b}\frac{dx_3}{v_0(x_3)}\right)\,dx \\ &-\int_{x_a}^{x_b}\frac{U^2}{v_0^3(x)}\int_{x_a}^{x}\frac{\phi'(x_1)}{v_0(x_1)}\exp\left(i\omega\int_{x_1}^{x_b}\frac{dx_3}{v_0(x_3)}\right)\,dx_1\,dx \\ &-\int_{x_a}^{x_b}\int_{x_a}^{x}\frac{U}{v_0^3(x_1)}\int_{x_a}^{x_1}\exp\left(i\omega\int_{x_2}^{x}\frac{dx_3}{v_0(x_3)}\right)\phi''(x_2)\,dx_2\,dx_1\,dx\Bigg] \\ \Bigg/ &\left(\int_{x_a}^{x_b}h(\sqrt{\phi(x)})+1-\frac{|U|}{\sqrt{U^2-2\phi(x)}}\,dx\right).\end{aligned} \tag{4.20}$$

$\dot{P}_i/\dot{P}_e$ can be expanded to give a much simpler form in the limit where the ion kinetic energy in the hole frame is much greater than their electrostatic potential energy $U^2 \gg 2\psi$ with ψ being the maximum of ϕ. This approximation is very well satisfied at the onset of instability observed in our simulation. The leading term of the expanded form is

$$\frac{\dot{P}_i}{\dot{P}_e}(\omega,U,\phi) \simeq -\frac{m_i}{m_e}\frac{\psi^2}{U^4}\frac{4i\frac{\omega}{U}I\left(\frac{\omega}{U}\right)+i\frac{\omega^2}{U^2}I'\left(\frac{\omega}{U}\right)-3I_0}{\displaystyle\int_{x_a}^{x_b}h(\sqrt{\phi(x)})-\frac{\phi(x)}{U^2}\,dx}, \tag{4.21}$$

where

$$I_0 = \int_{x_a}^{x_b}\tilde{\phi}(x)^2\,dx, \tag{4.22}$$

$$I\left(\frac{\omega}{U}\right) = \int_{x_a}^{x_b}\int_{x_a}^{y}\tilde{\phi}(x)\tilde{\phi}(y)\exp\left[i\frac{\omega(x-y)}{U}\right]\,dx\,dy, \tag{4.23}$$

with $\tilde{\phi}(x)=\phi(x)/\psi$ being the normalized potential profile function. This leading term is second order in the small expansion parameter $2\psi/U^2$. The details of this expansion are given in Appendix C. Both the full expression and the leading order expansion of $\dot{P}_i/\dot{P}_e(\omega)$ can be evaluated numerically for real frequencies ω using for example the widely cited Schamel type of EH potential $\phi(x)=\psi\,\mathrm{sech}^4(x/4)$. In the evaluation, we use the

sign convention that x_a is $-\infty$ and x_b is $+\infty$ in the hole frame. The resulting contours are plotted in the panel (a) of Figure 4-4. The number of encirclements of the point -1 in the complex plane by the $\dot{P}_i/\dot{P}_e(\omega)$ contour gives the number of unstable ω solutions to the eigenmode Eqn. (4.19). There is a critical speed U_c for $|U|$ below which the system is unstable. The leading order term is within a few percent of the full expression at the onset of instability. From now on, we will work with the leading order term instead of the full expression for the purpose of studying this instability. This approximation makes the mathematics much more tractable. Our analysis is general and can be applied to any type of equilibrium EH potential, including but not limited to Schamel type of EHs.

The $\dot{P}_i/\dot{P}_e(\omega)$ contour is essential to the study of this instability. We are going to take advantage of its scaling property to solve for the critical speed U_c. To simplify the notation, we introduce two auxiliary functions F and G defined as

$$F(\frac{\omega}{U}) = 4i\frac{\omega}{U}I(\frac{\omega}{U}) + i\frac{\omega^2}{U^2}I'(\frac{\omega}{U}) - 3I_0, \tag{4.24}$$

$$G(U) = \frac{m_e}{m_i}\frac{1}{\psi^2}\left[U^4\int_{x_a}^{x_b} h(\sqrt{\phi(x)})\,dx - U^2\int_{x_a}^{x_b}\phi(x)\,dx\right]. \tag{4.25}$$

We have therefore

$$\frac{\dot{P}_i}{\dot{P}_e}(\omega, U) = -\frac{F(\frac{\omega}{U})}{G(U)}. \tag{4.26}$$

We look for the critical speed U_c for a given equilibrium hole potential ϕ such that the $\dot{P}_i/\dot{P}_e(\omega)$ contour crosses the point -1 in the complex plane. F depends on U through ω/U, it gives the same contour for different U values when ω is evaluated on the real axis, although at different ω values. While F is a complex-valued function, function G only takes real values. U scales the size of the $\dot{P}_i/\dot{P}_e(\omega)$ contour through G. This property is demonstrated in Figure 4-4. The identical $F(\omega/U)$ contour for different values of U using a Schamel type of EH potential is shown in the panel (b) of Figure 4-4. We denote its intersection with the positive real axis by $C(\tilde{\phi})$. The existence of this intersection $C(\tilde{\phi})$ is guaranteed for a general class of admissible hole potential $\phi(x)$, which we will show later in this chapter. The critical speed U_c, below which the system is unstable, satisfies an

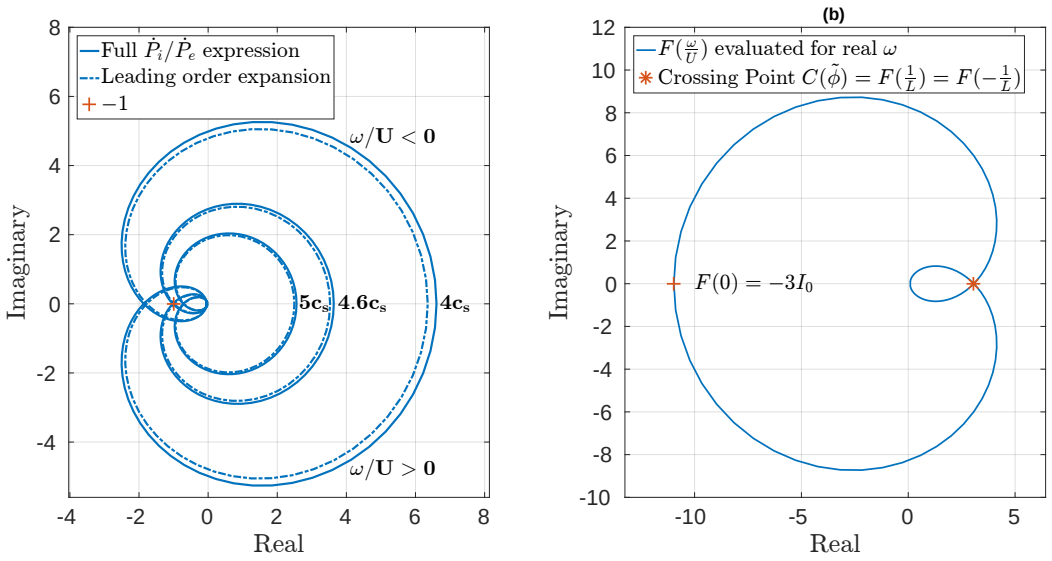

Figure 4-4: (a): $\dot{P}_i/\dot{P}_e$ evaluated on the real axis for $\phi = 0.23\,\mathrm{sech}^4(x/4)\,, m_i/m_e = 1836$ and three different hole speeds. $\dot{P}_i/\dot{P}_e(\omega)+1=0$ has two unstable zeros when $|U| < U_c = 4.6c_s$ here. (b): $F(\omega/U)$ function defined in Eqn. (4.24) evaluated for ω on the real axis using $\tilde{\phi}(x) = \mathrm{sech}^4(x/4)$. F contour is invariant for different hole velocity U.

equation

$$-\frac{C(\tilde{\phi})}{G(-U_c)} \;=\; -1. \tag{4.27}$$

The above equation gives a quadratic equation in U_c^2

$$U_c^4 \int_{x_a}^{x_b} h(\sqrt{\phi(x)})\,dx - U_c^2 \int_{x_a}^{x_b} \phi(x)\,dx - \psi^2 \frac{m_i}{m_e} C(\tilde{\phi}) = 0. \tag{4.28}$$

The unique real and positive solution of U_c^2 is

$$U_c^2 \;=\; \frac{\displaystyle\int_{x_a}^{x_b} \phi(x)\,dx + \sqrt{\left(\int_{x_a}^{x_b} \phi(x)\,dx\right)^2 + 4\psi^2 \frac{m_i}{m_e} C(\tilde{\phi}) \int_{x_a}^{x_b} h(\sqrt{\phi(x)})\,dx}}{2\displaystyle\int_{x_a}^{x_b} h(\sqrt{\phi(x)})\,dx}. \tag{4.29}$$

Now we calculate the oscillation frequency of the unstable eigenmode. At marginal instability, the $\dot{P}_i/\dot{P}_e(\omega)$ contour crosses -1. We need to find the frequency for which this

crossing happens. The imaginary part of $\dot{P}_i/\dot{P}_e$ is

$$\mathrm{Im}\left(\frac{\dot{P}_i}{\dot{P}_e}(\omega)\right) \;=\; -\frac{\mathrm{Im}\left(F(\frac{\omega}{U})\right)}{G(U)}, \tag{4.30}$$

where

$$\mathrm{Im}\left(F(\frac{\omega}{U})\right) \;=\; 4\frac{\omega}{U}\mathrm{Re}\left(I(\frac{\omega}{U})\right) + \frac{\omega^2}{U^2}\mathrm{Re}\left(I'(\frac{\omega}{U})\right). \tag{4.31}$$

To calculate the imaginary part of $\dot{P}_i/\dot{P}_e$, we need to evaluate $\mathrm{Re}(I(\frac{\omega}{U}))$. It can be shown by taking x_a and x_b to infinity that

$$\begin{aligned}\mathrm{Re}\left(I(\frac{\omega}{U})\right) \;&=\; \frac{1}{2}\left(\int_{-\infty}^{\infty}\tilde{\phi}(x)\exp\left(i\frac{\omega}{U}x\right)\,dx\right)\left(\int_{-\infty}^{\infty}\tilde{\phi}(y)\exp\left(-i\frac{\omega}{U}y\right)\,dy\right)\\ &=\; \frac{1}{2}\tilde{\Phi}(\frac{\omega}{U})^2,\end{aligned} \tag{4.32}$$

where $\tilde{\Phi}$ is the modulus of the Fourier transform of $\tilde{\phi}$. Thus $\mathrm{Im}(\dot{P}_i/\dot{P}_e)(\omega) = 0$ gives

$$\mathrm{Im}\left(F(\frac{\omega}{U})\right) \;\equiv\; \frac{\omega}{U}\tilde{\Phi}(\frac{\omega}{U})\left[2\tilde{\Phi}(\frac{\omega}{U}) + \frac{\omega}{U}\tilde{\Phi}'(\frac{\omega}{U})\right] \;=\; 0 \tag{4.33}$$

Eqn. (4.33) admits three real solutions for ω, one is the trivial $\omega = 0$, the other two solutions are given by the equation

$$-\frac{\tilde{\Phi}'(\frac{\omega}{U})}{2\tilde{\Phi}(\frac{\omega}{U})} \;=\; \frac{1}{\omega/U}. \tag{4.34}$$

Since $\tilde{\phi}$ is real, we have $\tilde{\Phi}$ is an even function and Eqn. (4.34) gives two solutions that have the opposite sign. We define the positive ω solution of Eqn. (4.34) as ω_0 and a length scale L

$$L \;\equiv\; \frac{|U|}{\omega_0}. \tag{4.35}$$

The $\dot{P}_i/\dot{P}_e$ contour crosses the real axis at frequency ω_0 for a given EH potential ϕ and U. L is the characteristic length of the EH and it is entirely determined by the EH potential *shape* $\tilde{\phi}$. At the onset of instability, we have $\dot{P}_i/\dot{P}_e(\omega_0(U_c), -U_c) = -1$, ω_0 evaluated for

the critical speed U_c is therefore the angular frequency of the initially growing unstable eigenmode. We define this frequency as

$$\omega_c \equiv \omega_0(U_c) \equiv \frac{U_c}{L}. \tag{4.36}$$

It is the critical ion transit frequency through the hole potential. The frequency of the growing oscillation corresponds to a physical frequency of the system.

The existence of this critical frequency ω_c and the crossing point $C(\tilde{\phi})$ are guaranteed by the continuous differentiablility of the EH potential $\phi(x)$. A physical EH potential $\phi(x)$ should possess a second derivative as it satisfies Poisson's equation $\phi''(x)+\rho(x)/\epsilon_0 = 0$, and a physical $\rho(x)$ should have bounded variation. This smoothness requirement constrains the asymptotic behavior of its Fourier transform. Function $\tilde{\Phi}(p)$ decays at least as fast as p^{-3} when $p \to \infty$ [98]. Thus we have $-\tilde{\Phi}'(p)/2\tilde{\Phi}(p) = -\frac{1}{2}d\ln(\tilde{\Phi}(p))/dp \geq 3/2p > 1/p$ as $p \to \infty$. While as $p \to 0$, we have $-\tilde{\Phi}'(p)/2\tilde{\Phi}(p) \to -\tilde{\Phi}'(0)/2\tilde{\Phi}(0) \ll 1/p$. Solutions are guaranteed for Eqn. (4.34). The behavior of the F contour is as follows. As $\omega/U \to 0^+$, we have $\mathrm{Re}(F(\omega/U)) \to -3I_0 < 0$ and $\mathrm{Im}(F(\omega/U)) \to 0^+$. Asymptotic analysis as $\omega/U \to +\infty$ gives $\mathrm{Re}(F(\omega/U)) \to 0^+$ and $\mathrm{Im}(F(\omega/U)) \to 0^-$. In other words, with ω/U increasing from 0 to infinity, the F contour starts from a point on the negative real axis, goes into the upper half plane, crosses the positive real axis at $1/L$ and returns to zero. The crossing point $C(\tilde{\phi})$ shown in Figure 4-4(b), which is crucial to this instability, is an universal feature for all physically admissible hole potentials $\phi(x)$ and we have $C(\tilde{\phi}) = F(1/L)$. Contours without a crossing can be obtained only from unphysical hole shapes. For example, $\tilde{\phi} = \exp(-|x|/\lambda)$ does not give a crossing point and is therefore stable; but it is unphysical, as the electric field is undefined at $x = 0$.

Having obtained the analytic solution for the critical speed and the unstable oscillation frequency, we now compare these results with our PIC observations. The hole pushing technique enables us to explore continuously the EH velocity in the ion frame. We performed a series of runs with different initialization to create EHs of different sizes. Then we determined the critical speed U_c by inspecting the onset of unstable velocity oscillations as the hole speed is decreased. It is compared with the threshold speeds ob-

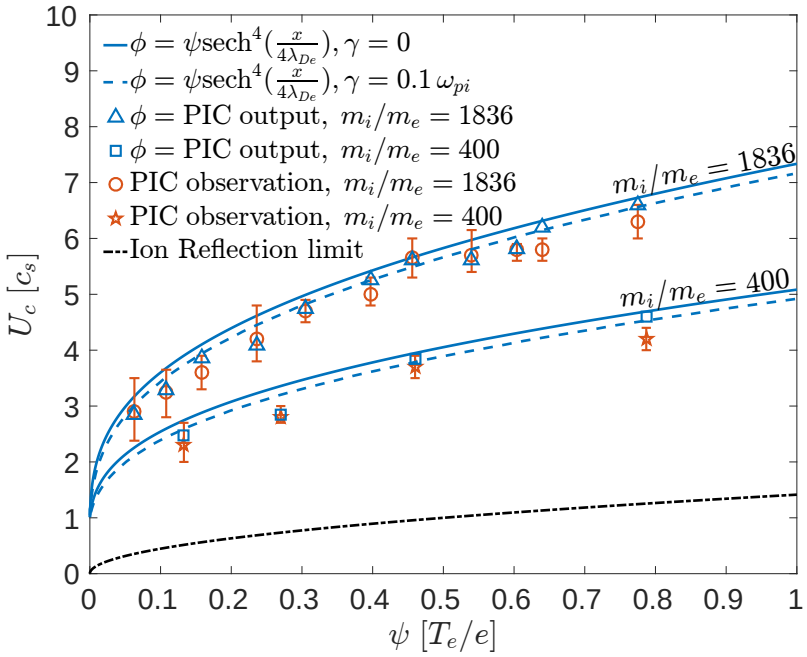

Figure 4-5: The critical values of hole speed in the ion frame below which the instability occurs for different sized EHs and two different mass ratios. The theoretical stability boundaries ($\gamma = 0$) and the $\gamma = 0.1$ growth rate boundaries for Schamel type of EHs $\phi(x) = \psi\,\mathrm{sech}^4(x/4)$ are plotted as reference lines. The observational data point and the numerical calculation of the same ψ correspond to the same run. The ion reflection limit is much lower than the instability threshold, hence our approximation $U^2 \gg 2\psi$ is well satisfied. All the PIC runs have $T_e/T_i = 20$.

tained by solving the Nyquist stability problem numerically using the $\phi(x)$ right before the instability onset from the same run. The electrostatic potential output $\phi(x)$ from our PIC simulation is used to construct the F contour numerically from Eqn. (4.24) and find its crossing point $C(\tilde{\phi})$. We use the formula for U_c in Eqn. (4.29) to calculate its predicted value. This method takes into account the exact potential shape of the EH in our PIC simulation which is different from one run to another [2]. The results are presented in Figure 4-5. The solid lines are obtained using Eqn. (4.29) assuming a Schamel type of

[2]Our hole-tracking PIC simulation produces relatively low-noise and highly resolved EH potential. We applied some post processing to the PIC potential output to make the numerical calculation more accurate. In our analysis, $\phi(x)$ is considered to fall to zero far away from the hole center. However, there is always some non-zero intrinsic statistical noise in the PIC simulation. In post processing, we find the positions where the electric field first becomes zero outside the hole center and consider them to be the limits of the hole spatial extent. The values of $\phi(x)$ beyond these limits are forced to decay to zero by multiplying a Debye decaying exponential to them. We use this slightly smoothed $\phi(x)$ in our numerical calculation of U_c.

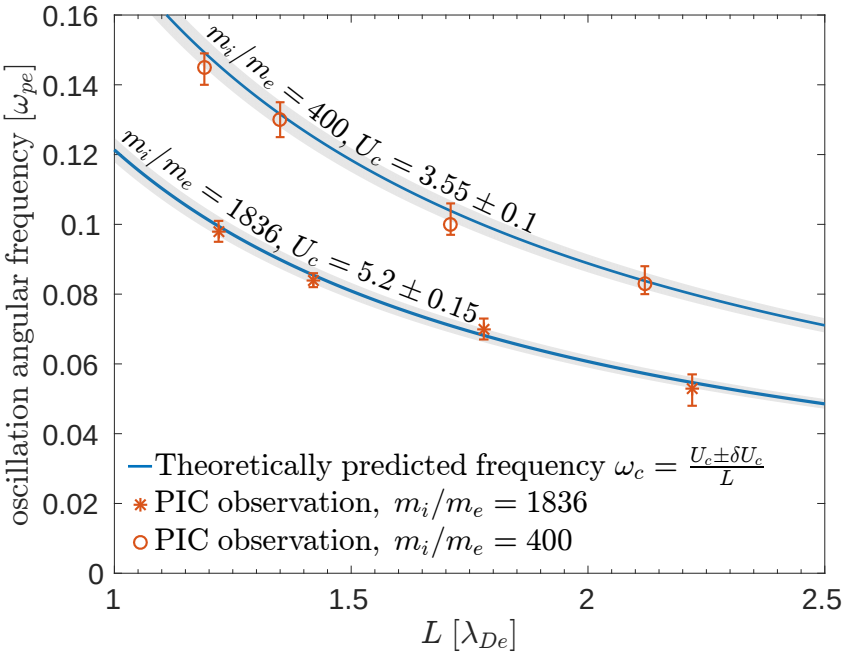

Figure 4-6: The oscillations seen in our simulation are Fourier analyzed to extract its main frequency for the first few periods of unstable oscillations. The uncertainty in the theoretically predicted frequency due to the uncertainty of U_c used in Eqn. (4.36) is shown by the gray uncertainty bands. Notice that the unstable oscillation frequency is in general a few times the ion plasma frequency.

EH potential. This solution's asymptotic behavior comes from the special function $h(\chi)$ [80]: $h(\chi) \to \chi^2 - \frac{8}{3\sqrt{\pi}}\chi^3$ as $\chi \to 0$ and $h(\chi) \to 1 - \frac{2}{\sqrt{\pi}\chi}$ as $\chi \sim 1$. For shallow holes $\psi \ll 1$, we have $U_c \simeq 1 + \mathcal{O}(\psi)$ and for deep holes $\psi \sim 1$, $U_c \sim (m_i/m_e)^{1/4}\psi^{1/2}$. The slight deviation of our data points from the solid curves represents the deviation of the hole potential in our PIC simulation from the Schamel type. The full calculation using the exact hole potential yields a good agreement with the observation. We have runs with two different mass ratios and our results show the $(m_i/m_e)^{1/4}$ scaling of U_c with the mass ratio as predicted by the theory. The linear growth rate $\gamma = \mathrm{Im}(\omega)$ of the instability when $|U| < U_c$ can be evaluated by solving the equation $\dot{P}_i/\dot{P}_e(\omega) + 1 = 0$ numerically for given $\phi(x)$, U and the mass ratio. In Figure 4-5, we show in dashed lines the EH velocity calculated as a function of ψ for $\gamma = 0.1$ and Schamel type of EH potential as a useful reference line. We shall give a detailed analysis of the growth rate in II.3.

In Figure 4-6, we show the frequencies of the unstable velocity oscillations seen in our

simulation. The EH position and hence velocity U is obtained from the hole-tracking module for each PIC time step of $0.3/\omega_{pe}$. A discrete Fourier transform of U during the first few unstable periods gives a sharp peak centered at the oscillation frequency. The error bar is given by the frequency range above half peak power. They are plotted against the characteristic hole width L defined in Eqn. (4.35) calculated using the potential $\phi(x)$ right before the oscillation onset from our PIC simulations. $\phi(x)$ gives numerically the F contour and it crosses the positive real axis at $F(1/L)$. EH initialization is adjusted in our PIC code to give EHs of different width L and a narrow range of potential height $\psi \sim 0.45$, hence U_c. The oscillation frequency predicted by our theory is inversely proportional to the hole width L: $\omega_c = U_c/L$. Good quantitative agreement is achieved between the observations and our theory. Our analysis captures the correct scaling with the mass ratio, which highlights the importance of ion dynamics for this instability.

The instability threshold U_c is scale invariant. If we apply a change of scale $x \to \lambda x$, the Eqn. (4.28) giving the critical speed U_c is invariant under this change of scale as each term is multiplied by the same factor $1/\lambda$. This property is obvious for the first two terms in Eqn. (4.28). For the third term, it can be shown that

$$F_\lambda(\frac{\omega}{U}) = \frac{1}{\lambda} F(\frac{\omega}{U\lambda}). \tag{4.37}$$

Hence the crossing point satisfies the same scaling relation $C_\lambda(\tilde{\phi}) = (1/\lambda)C(\tilde{\phi})$ and U_c remains invariant. However, the oscillation frequency scales linearly with λ: $\omega_{c,\lambda} = \lambda\omega_c$. For example, two different EH potentials $\phi(x) = \psi\,\mathrm{sech}^4(x)$ and $\phi(x) = \psi\,\mathrm{sech}^4(x/4)$ have the same threshold U_c, while the unstable oscillation frequency for the first potential profile is four times as high. This argument explains why the runs in Figure 4-6 have a similar U_c but different oscillation frequencies.

II.2 Counter-streaming ions

We have shown an example of the instability observed in a plasma with counter propagating ions in Figure 4-2. If the EH potential $\phi(x)$ is symmetric, then the counter-streaming

situation with an EH at rest $U = 0$ and two ion streams traveling at $\pm v_i$ is equivalent to having one single ion stream at rest and the EH traveling at $U = v_i$ for the described instability mechanism. The sign convention is our analysis is such that the ions enter from $-\infty$ and exit at $+\infty$. The change of hole velocity from U to $-U$ in the ion frame results in flipping the sign convention thus x_a and x_b. When the potential $\phi(x)$ is symmetric so that $\phi'(-x) = -\phi'(x)$ and $\phi''(-x) = \phi''(x)$, Eqns. (4.16) (4.18) show that the resulting $\dot{P}_i$ is exactly the opposite as $\dot{U}$ has an opposite sign under the two sign conventions. Therefore, the contribution to the total $\dot{P}_i$ from the two ion streams, evaluated with the same sign convention, should be exactly equal and add up. More concretely, an ion particle arriving from the left sees the same potential as an ion particle arriving from the right. However, the same EH acceleration $\dot{U}$ works in an opposite way for them. This argument explains why the instability threshold observed in the counter-streaming ion plasma is identical to the threshold value for the single ion stream case. The two situations are equivalent in terms of linear stability. Once the instability has fully grown, the nonlinear stage of the instability can be different for the two cases.

II.3 Linear growth rate

The linear growth rate of the instability is obtained by solving the eigenmode equation $\frac{\dot{P}_i}{\dot{P}_e}(\omega, U) + 1 = 0$, where $\dot{P}_i/\dot{P}_e$ is given by Eqn. (4.21). The growth rate γ is the imaginary part of the solution ω: $\gamma = \mathrm{Im}(\omega)$. Although analytic solution for arbitrary U is too difficult, we can obtain γ by an expansion near marginal instability. Recall that at marginal instability, we have

$$\frac{\dot{P}_i}{\dot{P}_e}(\omega_c = \frac{U_c}{L}, -U_c) = -1. \tag{4.38}$$

If the hole velocity is $U = -U_c + \Delta U$ such that $|\Delta U/U_c| \ll 1$. We need to find $\omega = \omega_c + \Delta\omega$ with $|\Delta\omega/\omega_c| \ll 1$ that satisfies the eigenmode equation $\dot{P}_i/\dot{P}_e(\omega, U) = -1$. A linear expansion gives

$$\Delta\omega \frac{\partial(\dot{P}_i/\dot{P}_e)}{\partial\omega}\bigg|_{\omega_c, -U_c} + \Delta U \frac{\partial(\dot{P}_i/\dot{P}_e)}{\partial U}\bigg|_{\omega_c, -U_c} = 0. \tag{4.39}$$

Substituting $\dot{P}_i/\dot{P}_e(\omega, U) = -F(\omega/U)/G(U)$, the two partial derivatives in Eqn. (4.39) can be evaluated with functions F and G

$$\left.\frac{\partial(\dot{P}_i/\dot{P}_e)}{\partial\omega}\right|_{\omega_c,-U_c} = \frac{F'(-\omega_c/U_c)}{U_c G(-U_c)}, \tag{4.40}$$

$$\left.\frac{\partial(\dot{P}_i/\dot{P}_e)}{\partial U_c}\right|_{\omega_c,-U_c} = \frac{F'(-\omega_c/U_c)G(-U_c)(\omega_c/U_c^2) + F(-\omega_c/U_c)G'(-U_c)}{G(-U_c)^2}. \tag{4.41}$$

Hence

$$\begin{aligned}\Delta\omega &= \Delta U\left\{ -\frac{\omega_c}{U_c} - U_c\frac{F(-\omega_c/U_c)}{G(-U_c)}\frac{G'(-U_c)}{F'(-\omega_c/U_c)}\right\}\\ &= \Delta U\left\{ -\frac{\omega_c}{U_c} - U_c\frac{G'(-U_c)}{F'(-\omega_c/U_c)}\right\},\end{aligned} \tag{4.42}$$

where we used $F(-\omega_c/U_c)/G(-U_c) = 1$. G is an even polynomial function defined in Eqn. (4.25) and $-U_cG'(-U_c) \equiv U_cG'(U_c)$ can be evaluated as

$$U_cG'(U_c) = 4F(\frac{\omega_c}{U_c}) + 2U_c^2\frac{m_e}{m_i}\frac{1}{\psi^2}\int_{x_a}^{x_b}\phi(x)\,dx. \tag{4.43}$$

Hence the final expression for $\Delta\omega$ is

$$\Delta\omega = \Delta U\left\{ -\frac{\omega_c}{U_c} + \frac{4F(\omega_c/U_c)}{F'(-\omega_c/U_c)} + 2U_c^2\frac{m_e}{m_i}\frac{1}{F'(-\omega_c/U_c)}\frac{1}{\psi^2}\int_{x_a}^{x_b}\phi(x)\,dx\right\}. \tag{4.44}$$

The growth rate γ is the imaginary part of $\Delta\omega$. The real part of $\Delta\omega$ gives a small correction to the oscillation frequency ω_c when U is different from U_c. We also have $\omega_c/U_c = 1/L$, a constant only depending on the hole shape, and $F(\omega_c/U_c) = F(1/L) = C(\tilde{\phi})$. While $F(\omega_c/U_c)$ is a real number, the derivative $F'(-\omega_c/U_c)$ is complex and γ is given by

$$\gamma = \Delta U\,\mathrm{Im}\left\{\frac{4F(1/L)}{F'(-1/L)} + 2U_c^2\frac{m_e}{m_i}\frac{1}{F'(-1/L)}\frac{1}{\psi^2}\int_{x_a}^{x_b}\phi(x)\,dx\right\}. \tag{4.45}$$

The first term is only a function of the hole shape $\tilde{\phi}$ while the second term depends on hole size ψ and the mass ratio m_i/m_e. However, this second term is not important except for extremely shallow EHs such that $\psi \ll 1$. For example, for a Schamel type of EH of size $\psi = 0.1$ and $m_i/m_e = 1836$, the magnitude of the second term is about 4% of the

first one. It is thus a good approximation that for not too shallow EHs we have

$$\gamma \simeq \Delta U \,\mathrm{Im}\left\{\frac{4F(1/L)}{F'(-1/L)}\right\} = \Delta U \,\mathrm{Im}\left\{\frac{4F(1/L)}{F'(1/L)}\right\} = -\Delta|U|\,\mathrm{Im}\left\{\frac{4F(1/L)}{F'(1/L)}\right\}. \quad (4.46)$$

We define $\Delta|U| = |U| - U_c$ and the imaginary part of F is odd so its derivative is even: $\mathrm{Im}(F'(-1/L)) = \mathrm{Im}(F'(1/L))$. This growth rate scales linearly with $\Delta|U|$. If the hole potential shape is of Schamel type, a numerical evaluation of the constants gives $\gamma \simeq -\Delta|U|/1.74$ for $|U|$ evaluated in c_s and γ evaluated in ω_{pi}. The instability grows fast once $|U|$ is slower than U_c.

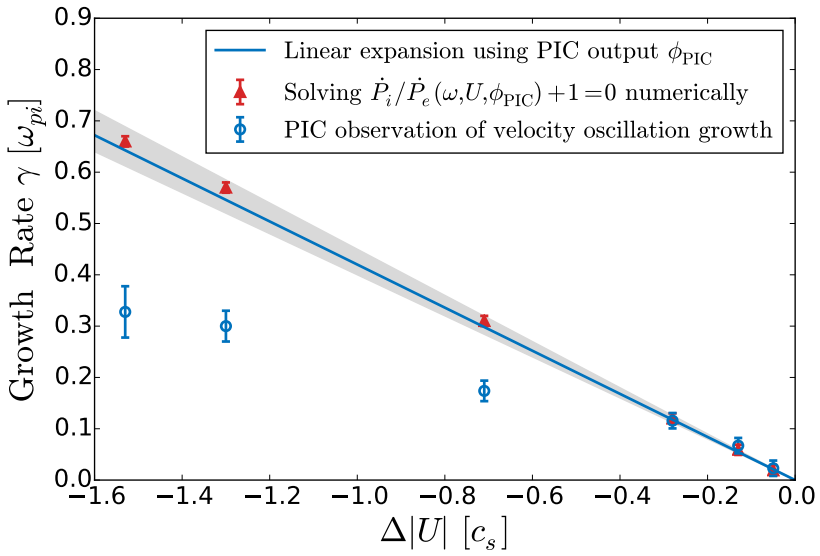

Figure 4-7: Instability growth rate γ as a function of ΔU. The linear relation represents Eqn. (4.46) for fixed hole shape. Its uncertainty bands represent the small variation of shape from one run to another, giving uncertainty in the comparison. The triangles are obtained from solving numerically the full eigenmode equation $\dot{P}_i/\dot{P}_e + 1 = 0$ using the PIC potential output. Circles are the growth rate observed in PIC runs.

In the PIC simulations, we measured the growth rate of unstable velocity oscillations by fitting an exponential growth model to it. We used the unstable runs with different counter-streaming ion velocity and $\psi \sim 0.8$, in which $\Delta|U|$ can be precisely measured. The growth rates and the error bars are obtained from the regression. They are compared with the expanded linear solution in Eqn. (4.46) and numerical solutions of the full eigenmode equation. The results are shown in Figure 4-7. Our analytic theory agrees with the

observed instability growth rate for the weakly unstable cases up to $\gamma \sim 0.1$ and the linear expansion gives a very good approximation to the solution of the full eigenmode equation. The growth rates for strongly unstable cases are smaller than the predicted values. The sign of discrepancy is two-fold: First, it is difficult to observe the instability in its true linear stage when the growth rate is important. Second, the approximations used in our analytic theory break down when we are deeply below the stability boundary. We are going to discuss the nonlinear aspects of the instability in Section IV.

II.4 Finite ion temperature

So far, we have treated the ions as a cold beam. In reality, they have a thermal velocity spread. For an ion of velocity v, the EH has a velocity $U - v$ in its frame. Let us consider the ion thermal speed to be small compared to $|U|$ such that $v_{\rm th,i} \ll |U|$ and there are no reflected ions by the hole potential. As U_c is several times c_s, this assumption holds approximately even when $T_i \geq T_e$. We can integrate the contributions from ions of different velocities to get the total $\dot{P}_i$

$$\dot{P}_i(\omega, U, \phi, v_{\rm th,i}) \;=\; m_i \dot{U} \int_{-\infty}^{\infty} f_{\infty,i}(v) \frac{\psi^2}{(U-v)^4} F(\frac{\omega}{U-v})\, dv. \tag{4.47}$$

We apply a Taylor series expansion to Eqn. (4.47) assuming $|v| \ll |U|$. Consider $f_{\infty,i}(v)$ to be a Maxwellian and only the even order moments of v survive after the integration over velocity. This expansion gives

$$\begin{aligned} \dot{P}_i(\omega, U, \phi, v_{\rm th,i}) \;&=\; n_\infty m_i \dot{U} \frac{\psi^2}{U^4} \left\{ F(\frac{\omega}{U}) + F_2(\frac{\omega}{U})(\frac{v_{\rm th,i}}{U})^2 + \mathcal{O}\left((\frac{v_{\rm th,i}}{U})^4\right) \right\} \\ &=\; n_\infty m_i \dot{U} \frac{\psi^2}{U^4} \left\{ F_{\rm th,i}(\frac{\omega}{U}) + \mathcal{O}\left((\frac{v_{\rm th,i}}{U})^4\right) \right\}, \end{aligned} \tag{4.48}$$

where

$$F_2(\frac{\omega}{U}) \;=\; 10F(\frac{\omega}{U}) + 5F'(\frac{\omega}{U})(\frac{\omega}{U}) + \frac{1}{2}F''(\frac{\omega}{U})(\frac{\omega}{U})^2. \tag{4.49}$$

We have right now $\dot{P}_i/\dot{P}_e(\omega, U, \phi, v_{\rm th,i}) = -F_{\rm th,i}(\omega/U)/G(U)$ to leading order in $|v_{\rm th,i}/U|$. It suffices to substitute F with $F_{\rm th,i}$ in our previous analysis and everything follows as

before.

The leading order term of the finite ion temperature correction is second order in $|v_{\mathrm{th,i}}/U|$. The effect of finite ion temperature can be visualized through the $F_{\mathrm{th,i}}$ contours. In Figure 4-8, we show the $F_{\mathrm{th,i}}$ contours evaluated on the real axis for different values of $|v_{\mathrm{th,i}}/U|$ using Schamel type of EH potential. The most salient effect is that the finite ion temperature moves the crossing point $C(\tilde{\phi})$ outwards, resulting in a higher value for U_c. Because of the leading U^4 term in $G(U)$, the resulting change in U_c is actually relatively small. In terms of U_c, this correction is $\sim 5\%$ when $|U| = 5v_{\mathrm{th,i}}$, it grows to $\sim 10\%$ for $|U| = 4v_{\mathrm{th,i}}$ and $\sim 20\%$ when $|U| = 3v_{\mathrm{th,i}}$. This property holds similarly for other EH potential models such as the Gaussian. The same trend is noticed in our PIC simulation. A higher ion temperature T_i leads to a slightly higher threshold velocity U_c.

When $|U| < 3v_{\mathrm{th,i}}$, the ion reflection from the EH potential becomes important and can no longer be neglected in the global momentum balance. The unbalanced scattering of ions tends to accelerate the EH to a higher velocity in the ion frame [80]. With the hole pushing technique, we were able to explore the situation with the presence of mild ion reflection from the hole potential, the instability is still observed in these cases. After the onset of instability, we stopped hole pushing and observed the hole velocity to oscillate while its mean velocity accelerates due to the ion reflection. Resonant ion effects such as ion Landau damping or reflection only become important when $|U| \sim v_{\mathrm{th,i}}$, which requires the ions to be extremely hot. Our analysis holds well for the usual range of T_e/T_i in space plasmas.

III Eigenmode ansatz derived from linearized Vlasov-Poisson system

This section serves as a supplement to the previous hole kinematics approach. It is inspired by the comments from an anonymous referee that we have received. We will justify the Goldstone mode ansatz (the hole changes its velocity while maintaining its shape) from the linearized Vlasov-Poisson system. We shall see that this mode stems from a low-frequency

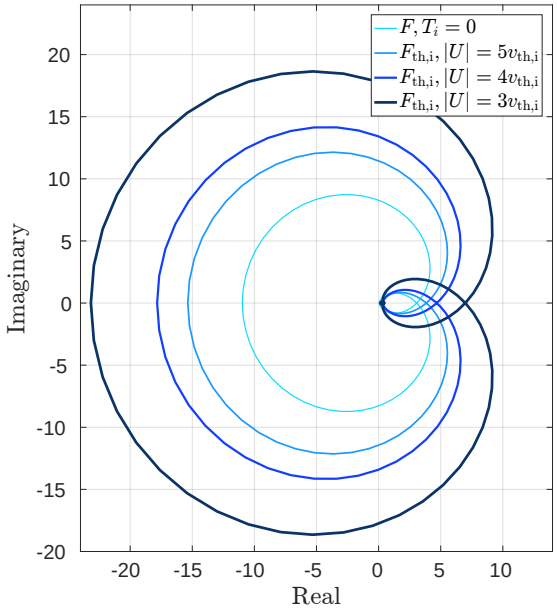

Figure 4-8: Finite ion temperature effect on the F contour for a Schamel type of EH. The contour shape is approximately preserved while its size grows with a larger T_i.

adiabatic assumption for the electrons and a negligible ion response. This section also establishes some connection between the method we have presented so far and the more "traditional" kinetic theory approach.

First, we linearize the Vlasov-Poisson system about an EH equilibrium. The Vlasov equation in coordinate system $(t, x, \mathcal{E})$ with $\mathcal{E} = m_q v^2/2 + q\phi(x,t)$ is given by $df_q/dt = 0$ as

$$\left(\frac{\partial}{\partial t} + v\frac{\partial}{\partial x} + q\frac{\partial \phi}{\partial t}\frac{\partial}{\partial \mathcal{E}}\right) f_q = 0, \tag{4.50}$$

where $\mathcal{E}$ is the instantaneous particle energy and q is the particle charge. The charge density ρ can thus be written as

$$\rho = \sum_q q \int \frac{f_q^+ + f_q^-}{m_q|v|}\, d\mathcal{E}, \tag{4.51}$$

where superscripts $+$ and $-$ designate particles having positive and negative velocities. For a particle with positive/negative velocity, we have $v = \pm\sqrt{2(\mathcal{E} - q\phi)/m_q}$. Poisson's

equation can be written as

$$\epsilon_0 \frac{\partial^2 \phi}{\partial x^2} + \sum_q q \int \frac{f_q^+ + f_q^-}{m_q |v|} \, d\mathcal{E} = 0. \tag{4.52}$$

We write $\phi = \phi_0 + \phi_1 + ...$, $f_q^\pm = f_{q,0}^\pm + f_{q,1}^\pm + ...$ and $\rho = \rho_0 + \rho_1 + ...$, with subscript 0 denoting equilibrium quantities and subscript 1 denoting first-order perturbations. The linearized Vlasov-Poisson system in the co-moving frame of the equilibrium EH can be written as

$$\begin{cases} \dfrac{\partial f_{q,1}^\pm}{\partial t} \pm \sqrt{2(\mathcal{E} - q\phi_0(x))/m_q} \dfrac{\partial f_{q,1}^\pm}{\partial x} + q \dfrac{\partial \phi_1}{\partial t} \dfrac{\partial f_{q,0}^\pm}{\partial \mathcal{E}} = 0, \\ \epsilon_0 \dfrac{\partial^2 \phi_1}{\partial x^2} + \phi_1 \dfrac{d\rho_0(\phi_0)}{d\phi_0} + \displaystyle\sum_q q \int \frac{f_{q,1}^+ + f_{q,1}^-}{\sqrt{2m_q(\mathcal{E} - q\phi_0(x))}} \, d\mathcal{E} = 0. \end{cases} \tag{4.53}$$

We look for localized eigenmodes that vanish far away from the hole center when $x \to \pm\infty$. Also we look for perturbed quantities that depend on t as $\exp(-i\omega t)$ such that $\partial/\partial t$ can be replace by $-i\omega$ while taking the Fourier transform. The linearized Vlasov equation is a first-order ordinary differential equation about variable x after taking the Fourier transform in time. It can be solved to give an expression for $f_{q,1}^\pm$ with vanishing boundary conditions:

$$f_{q,1}^\pm(x, \mathcal{E}) = \frac{\pm i\omega q \displaystyle\int_{x_a}^{x} \frac{1}{|v_0|} \phi_1(x_1) \frac{\partial f_{q,0}^\pm}{\partial \mathcal{E}} \exp(\mp i\omega \int_{x_a}^{x_1} \frac{1}{|v_0|} \, dx') \, dx_1}{\exp(\mp i\omega \displaystyle\int_{x_a}^{x} \frac{1}{|v_0|} \, dx')}. \tag{4.54}$$

We use v_0 to express $\pm\sqrt{2(\mathcal{E} - q\phi_0)/m_q}$. It is easy to notice that $f_{q,1}^\pm$ will vanish when $\omega \to 0$. In this limit, the linearized Poisson's equation becomes

$$\epsilon_0 \frac{d^2 \phi_1}{dx^2} + \phi_1 \frac{d\rho_0(\phi_0)}{d\phi_0} = 0. \tag{4.55}$$

The eigenvalue problem associated with this equation and vanishing boundary conditions can be solved with $\phi_1 = C \dfrac{d\phi_0}{dx}$, where C is a constant. Use this expression in the left

hand side of Equation (4.55) and we have

$$\begin{aligned}
\epsilon_0 \frac{d^2\phi_1}{dx^2} + \phi_1 \frac{d\rho_0(\phi_0)}{d\phi_0} &= \epsilon_0 C \frac{d^2}{dx^2}\left(\frac{d\phi_0}{dx}\right) + C\frac{d\phi_0}{dx}\frac{d\rho_0(\phi_0)}{d\phi_0} \\
&= C\frac{d}{dx}\left(\epsilon_0 \frac{d^2\phi_0}{dx^2}\right) + C\frac{d\phi_0}{dx}\frac{d\rho_0(\phi_0)}{d\phi_0} \\
&= C\frac{d}{dx}\left(-\rho_0(\phi_0)\right) + C\frac{d\phi_0}{dx}\frac{d\rho_0(\phi_0)}{d\phi_0} \\
&= -C\frac{d\phi_0}{dx}\frac{d\rho_0(\phi_0)}{d\phi_0} + C\frac{d\phi_0}{dx}\frac{d\rho_0(\phi_0)}{d\phi_0} = 0. \qquad (4.56)
\end{aligned}$$

The eigenmode $\phi_1 = C\dfrac{d\phi_0}{dx}$ corresponds to a displacement of the steady-state equilibrium. This zero-frequency shift mode is the so-called Goldstone mode, resulting from the soliton solution breaking the continuous translational symmetry of the system. We shall see that when the frequency ω is much lower than some time scales of the system, the Goldstone mode is still the valid eigenmode to the lowest order at the onset of instability. For passing species, we introduce a time of flight function $\tau_\pm(x, \mathcal{E})$:

$$\tau_+(x, \mathcal{E}) = \int_{x_a}^{x} \frac{1}{|v_0|}\, dx', \qquad (4.57)$$

$$\tau_-(x, \mathcal{E}) = \int_{x}^{x_b} \frac{1}{|v_0|}\, dx'. \qquad (4.58)$$

Equation (4.54) can then be expressed as

$$f^+_{q,1}(x, \mathcal{E}) = i\omega q \int_{x_a}^{x} \frac{1}{|v_0|}\phi_1(x_1)\frac{\partial f^+_{q,0}}{\partial \mathcal{E}} \exp(i\omega(\tau_+(x) - \tau_+(x_1)))\, dx_1, \qquad (4.59)$$

$$f^-_{q,1}(x, \mathcal{E}) = i\omega q \int_{x}^{x_b} \frac{1}{|v_0|}\phi_1(x_1)\frac{\partial f^-_{q,0}}{\partial \mathcal{E}} \exp(i\omega(\tau_-(x) - \tau_-(x_1)))\, dx_1. \qquad (4.60)$$

An estimate of these integrals gives for passing species $f^\pm_{q,1} \sim i(\omega\tau_\pm)q\dfrac{\partial f^\pm_{q,0}}{\partial \mathcal{E}}\phi_1$. Thus the last term in the linearized Poisson's equation of Equation (4.53) is of order $\mathcal{O}(\omega\tau_\pm)$ compared to the second term, which is an adiabatic contribution. For the bulk of passing electrons, we have $\omega\tau_\pm \ll 1$. Therefore this contribution can be ignored to the lowest order. Recall that we used the same argument in the beginning of Section II while

discussing the electron response. Passing electron orbits violating this short-transit-time approximation are the ones near separatrices, it is only a small fraction of the total passing electron population. We can therefore neglect the contributions from these marginally passing electrons. However, the short-transit-time argument does not hold for ions. We have seen that the unstable oscillation frequency is the order of inverse ion transit time such that $\omega\tau_i \sim 1$. Another ordering of the system helps us here. We know that the ion contribution to the total charge density is of order $\psi/U^2 \ll 1$ at the onset of instability. Hence the ion correction to ϕ_1 is of order $\mathcal{O}(\psi/U^2)$ smaller than the electron term.

Now we treat the trapped electrons. Trapped electrons have bounded orbits but they all go through $x = 0$, which is the center of the electron hole. We introduce a time τ

$$\tau(x, \mathcal{E}) = \int_0^x \frac{1}{|v_0|} |dx'|. \tag{4.61}$$

τ takes its value between $-T/4$ and $T/4$. T is the period of a trapped orbit of energy $\mathcal{E}$. ϕ_1 is a function of x and thus a function of τ defined between $-T/4$ and $T/4$. We extend its definition to the entire real axis by completing it as a periodic function of τ with a period T where $x(\tau)$ for $\tau \in [T/4, 3T/4]$ is obtained by reflection with axis $T/4$. In this way, we can define a Fourier series expansion for $\phi_1(\tau)$. Plugging in the trial eigen-function $\phi_1 = C\dfrac{d\phi_0}{dx}$ which is an odd function of x and hence τ, we have

$$\phi_1 = C\frac{d\phi_0}{dx} = C\sum_{n=1}^{+\infty} S_n \sin(\omega_n \tau), \tag{4.62}$$

where S_n is the Fourier coefficient of $d\phi_0/dx$ associated with frequency $\omega_n = 2n\pi/T$. The linearized Vlasov equation Fourier transformed in time can be written with τ

$$-i\omega f_{e,1}^{\pm} \pm \frac{\partial f_{e,1}^{\pm}}{\partial \tau} - i\omega q C \frac{d\phi_0}{dx}\frac{\partial f_{e,0}^{\pm}}{\partial \mathcal{E}} = 0. \tag{4.63}$$

Now expand $f_{e,1}^{\pm}$ in Fourier series of τ: $f_{e,1}^{\pm} = \sum_{n=-\infty}^{n=+\infty} C_n^{\pm} \exp(i\omega_n \tau)$. The steady state distribution is only a function of the energy, $\partial f_{e,0}^{\pm}/\partial \mathcal{E}$ is thus independent of x hence τ.

The coefficients $C_n^{\pm}$ can be identified from Equation (4.63) as

$$\begin{cases} C_n^{\pm} &= \dfrac{\omega q C S_n}{2i(\pm\omega_n - \omega)} \dfrac{\partial f_{e,0}^{\pm}}{\partial \mathcal{E}} \text{ for } n > 0, \\ C_0^{\pm} &= 0, \\ C_n^{\pm} &= \dfrac{-\omega q C S_n}{2i(\pm\omega_n - \omega)} \dfrac{\partial f_{e,0}^{\pm}}{\partial \mathcal{E}} \text{ for } n < 0. \end{cases} \tag{4.64}$$

We can expand $f_{e,1}^{\pm}$ only with sinusoidal functions

$$f_{e,1}^{\pm} = \sum_{n=1}^{n=\infty} \frac{\omega q C S_n}{\pm\omega_n - \omega} \frac{\partial f_{e,0}^{\pm}}{\partial \mathcal{E}} \sin(\omega_n \tau). \tag{4.65}$$

The non-adiabatic contribution due to trapped electrons in the linearized Poisson's equation is evaluated using $f_{e,1}^{+} + f_{e,1}^{-}$ as

$$\begin{aligned} &(-e) \int_{\text{trapped}} \frac{f_{e,1}^{+} + f_{e,1}^{-}}{\sqrt{2m_e(\mathcal{E} + e\phi_0(x))}}\, d\mathcal{E} \\ &= \sum_{n=1}^{n=\infty} \text{P.V.} \int_{\mathcal{E}<0} \frac{2\omega^2}{\omega_n^2 - \omega^2} \frac{e^2 C S_n}{\sqrt{2m_e(\mathcal{E} + e\phi_0(x))}} \frac{\partial f_{e,0}}{\partial \mathcal{E}} \sin(\omega_n \tau)\, d\mathcal{E} + i\pi \mathcal{O}\left(\frac{\partial f_{e,0}}{\partial \mathcal{E}}|_{\omega_n = \omega} \right) \end{aligned} \tag{4.66}$$

In an EH, the trapped electrons have bounce frequencies ω_1 as low as zero. No matter how low the frequency of the mode ω is, there is always finite number of resonant particles such that $\omega_n = \omega$. This is the reason why we need to take the Cauchy principal value of the resonant integral in Equation (4.66) and add back the damping term. Like in the case for passing particles, these resonant orbits cluster near the separatrix and constitute a small fraction of the electron phase-space. The resonant effect is proportional to $\partial f_{e,0}/\partial \mathcal{E}$. We shall neglect the resonant particle effect and focus on deeply trapped electrons. Deeply trapped electrons have a bounce frequency on the order of $\sqrt{\psi}/L$, where L is the width of the EH. Expressed with the normalization in this chapter, this frequency is measured in ω_{pe}. We also know that the frequency of the unstable mode we consider is $\omega = U/L$, which is measured in ω_{pi}. In the parameter regime we are interested in, we have $\frac{m_i}{m_e}\psi \gg U^2$.

Therefore for deeply trapped electrons we have $\omega_1 \gg \omega$ and this ordering holds even better for higher-order harmonics ω_n. The lowest order non-adiabatic contribution from trapped electrons is of order $\mathcal{O}\left(\omega^2/\omega_n^2\right)$, which can be seen from Equation (4.66).

The Goldstone mode ansatz (the EH oscillates in velocity while maintaining its shape) we have used in our momentum balance calculation is therefore a very good one when the frequency of the mode is significantly lower than average electron transit frequency and the bounce frequency for deeply trapped electrons. The electrons approximately maintain an adiabatic behavior and the ion contribution to ϕ_1 is small.

Now if we multiply the linearized Poisson's equation by $d\phi_0/dx$ and integrate it between x_a and x_b using integration by parts and the boundary conditions, we get

$$\int_{x_a}^{x_b} \frac{d\phi_0}{dx} \sum_q q \int \frac{f_{q,1}^+ + f_{q,1}^-}{\sqrt{2m_q(\mathcal{E} - q\phi_0(x))}}\, d\mathcal{E} = 0. \tag{4.67}$$

This is the momentum conservation condition that we have used in the hole kinematics approach.

IV Discussion

The deformation of hole potential during oscillation has been neglected in our analysis. It is a next order correction for the "jetting" effect we have calculated. We now show that the ion momentum change due to the hole potential variation can be ignored in the parameter regime we are interested in. When an ion transits through the EH potential, its momentum changes when there is a temporal variation of the hole potential height. We call this the hole growth "jetting" effect and a formula is given in Chapter 2

$$(v_{bf} - v_{as})_{\text{growth}} \simeq -\frac{1}{U} \int_{x_a}^{x_b} \frac{1}{v} \frac{\partial \phi}{\partial t}\, dx, \tag{4.68}$$

where $\partial\phi/\partial t$ represents the temporal variation of the hole potential in its rest frame. It is related to the change in charge density by Poisson's equation. To a first approximation, we assume that the frequency of velocity oscillation is low so that the electron density

remains the same in the hole frame. Therefore, the only density variation comes from the ions and we have approximately $\delta\phi/\phi \sim \delta n_i/n_i$. Using $n_i\partial\phi/\partial t \sim \phi\partial n_i/\partial t$, we get

$$\begin{aligned}(v_{bf} - v_{as})_{\text{growth}} &\sim \frac{1}{U}\int_{x_a}^{x_b} \frac{\phi}{vn_i}\frac{\partial n_i}{\partial t}\,dx \\ &\sim \frac{1}{U}\int_{x_a}^{x_b} \frac{\phi}{vn_i}\frac{n_i\dot{U}}{v}\,dx \\ &\sim \frac{\psi}{U^2}(v_{bf} - v_{as})_{\text{accel}}.\end{aligned} \tag{4.69}$$

The $(v_{bf} - v_{as})_{\text{accel}}$ is the "jetting" effect due to hole acceleration. It was shown in Eqn. (4.8). The ion momentum change due to self-consistent EH potential variation is on the order of a factor $\psi/U^2 \ll 1$ smaller than the momentum change due to EH acceleration. Thus we can ignore it in the momentum balance.

In our analysis, the trapped electrons are assumed to move with the hole potential while remaining on their trapped orbits in an oscillating hole. However, there are always shallowly trapped electrons whose slow orbits will resonate with the oscillation frequency. The fraction of these resonant particles is small and they do not much affect the linear stability analysis. Once the instability has fully developed, some resonant particles become detrapped, causing the EH to shrink in size. This is the nonlinear stage of the instability. Trapped electrons in a steady-state EH are tagged in our simulations to follow their motion [81]. The detrapping of trapped electrons by the instability is shown in Figure 4-9. It is observed that the instability can be nonlinearly saturated by the shrinking of the EH. In some other cases, the oscillation amplitude in the hole velocity grows until the EH velocity is in the close vicinity of the ion velocity. The EH is then disrupted by the ions through the mechanism described by Saeki *et al.* [75] The presence of a parallel electric field can slow down the EHs in the ion frame and lead to the instability. Happening in space, this instability can cause ion heating by ion Landau damping and drive anomalous resistivity [76]. The EHs are considered to stem from phase-space instability and they are reservoirs of wave energy. The described instability provides a mechanism to couple the stored wave energy in the EH to the ion and electron plasma energy.

Our solitary wave velocity stability theory is generic and appears to apply to ion-

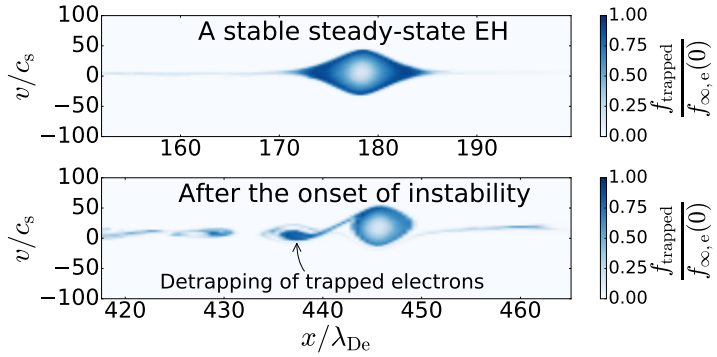

Figure 4-9: Phase-space density of trapped electrons in our hole-tracking PIC simulation before and after the instability onset. The EH is broken into smaller pieces by this instability.

acoustic solitons. Why are ion-acoustic solitary waves, propagating at a velocity slightly higher than c_s in the ion frame, stable? $\dot{P}_e$ goes to 0 when $|U|$ approaches c_s for small wave amplitude ψ. Hence, for a solitary wave propagating around this velocity, solutions of our dispersion relation, $\dot{P}_i/\dot{P}_e + 1 = 0$, exist only at very high frequencies where the short-transit-time approximation for electrons break down. So it is possible to have a stable propagation region for the solitary wave at a speed around c_s. For a solitary wave in this regime, $|\dot{P}_i/\dot{P}_e(\omega)| \gg 1$ for all physical frequencies of the system. The ion dynamics therefore dominates over the electron dynamics inside the solitary wave and it propagates like a Korteweg-de Vries-type ion-acoustic soliton even though an electron phase-space structure might be attached to it.

In contrast, a solitary wave propagating much faster than U_c is dominated by electron dynamics: $|\dot{P}_i/\dot{P}_e(\omega)| \ll 1$ for all physical ω, and can be considered a pure electron hole. When the ion dynamics and electron dynamics are comparable inside a propagating solitary wave, our stability theory predicts that the propagation can be driven unstable by positive dynamical feedback between the two species. The velocity instability reported in this chapter naturally separates these two major types of plasma electrostatic solitary waves. We will address this point in greater detail in Chapter 5

V Conclusion

In this chapter, we have reported a new kind of instability for an EH propagating with the presence of heavier ions and we have presented the theoretical understanding behind it. An EH at low speed in the ion frame experiences unstable velocity oscillations that can be understood treating it as a holistic object. Our analytic treatment is in full agreement with the PIC simulation observations for instability thresholds and frequencies, partial agreement is achieved for instability growth rates. The "slow" EHs that are observed in space might be susceptible to this instability. We demonstrated that the velocity oscillations initially take place at the critical ion transit frequency through the hole potential and it grows quickly to a noticeable level once the speed is below the threshold. The instability happens when the electron and ion dynamics are 180 degrees out of phase. Our discovery is a type of solitary wave instability driven by the different inertial scales of the two constituent species of the plasma.

Chapter 5

Slow electron hole coupled to an ion-acoustic soliton

Electrostatic Solitary Waves (ESWs) traveling in the ion frame at velocities on the order of ion sound speed c_s measured by Cluster satellites have been reported by Khotyaintsev et al. [91] at a magnetic reconnection site. The authors have also reported non-Maxwellian electron distribution suggesting the existence of electron phase-space structures. Since the first discovery of such kind, more ESW observations have been reported with velocities in a similar range [92, 99]. These velocities are significantly slower than what was previously observed in space plasma for ESWs, which are considered to be electron phase-space holes created by kinetic micro-instabilities in a highly collisionless plasma. There have been different explanations for the slow velocities of these ESWs. Some authors argued that slow electron holes are generated by Buneman instability from an electron beam interacting with bulk ions [92]. Others are hinting at ion-acoustic solitons in a multi-species plasma to account for these slow ESWs [100].

The current chapter explores slow electron holes using one-dimensional fully kinetic PIC simulation. Our study shows that in order to travel at a slow velocity in the ion frame on the order of c_s, an electron phase-space hole must form a stable coupling with an ion density perturbation, which is a hybrid of an electron hole with an ion-acoustic soliton (IAS). In this stable coupling, the electron phase-space hole is dragged along by

the compressional ion pulse and its dynamics deviates significantly from its free state. We demonstrate that this Coupled Hole Soliton (CHS) exhibits behavior that is intermediate between a BGK electron hole and an ion-acoustic soliton. They survive collisions instead of merging even with a small velocity difference. However, the collision process of two such solitary waves differ from what is described by KdV equation or the modified KdV equation obtained by Schamel for an ion acoustic soliton with resonant electrons [40, 67]. These results suggest that strong electron dynamics during collision of two CHS violates the simple electron equation of state $p_e(\phi)$ that is used to derive the canonical nonlinear partial differential equations.

Furthermore, we demonstrate that there is a velocity gap between a stable CHS and a "free" electron hole. This gap in the velocity of an ESW is set by the electron hole velocity oscillatory instability studied in Chapter 4.

We further show that transition between these two states is possible. Ion Landau damping damps the ion-acoustic soliton of the CHS and triggers the oscillatory velocity instability that eventually releases the electron hole from the CHS. An electron hole may become stably trapped in an ion-acoustic soliton excited by its potential when it is experiencing fast growth. We demonstrate this in a plasma with rising background density, mimicking the plasma wake of an object. If the background density growth rate is not high enough, the electron phase-space hole collapses as a result of the oscillatory velocity instability. However, with enough growth rate from the rising density, a phase-space hole may go through the unstable stage and become stably coupled to an ion density perturbation.

We performed simulations of Buneman instability, showing the production of both types of electron phase-space density holes with distinct velocities. Electron holes that are coupled to an ion-acoustic soliton are more likely to be produced with a cold ion population during Buneman instability.

This study is important for better understanding the distinct velocities and dynamics of electron phase-space holes observed in space and computer simulations [101]. Two species of electron phase-space holes exist; fast electron holes are not significantly inter-

acting with ions and therefore have electron-like dynamics; in a stable CHS, the electron hole is trapped and is dominated by ion scale dynamics. The velocity gap separating these two species can potentially be verified using space measurement data for ESWs.

I Coupling an electron phase space hole to an IAS

In Chapter 3, we have demonstrated uniform density initialization of an electron phase-space hole in our PIC simulation. Transient acceleration from the initial hole growth propels the formed electron hole to a velocity of several times c_s. In this section, we are going to introduce a different initialization scheme to stably embed an electron phase-space hole into an ion density compressional pulse. For this study, we use the one dimension electrostatic PIC code ESPIC that we have introduced in Chapter 3 with open boundaries. Its hole tracking function is turned off if not stated otherwise. A Gaussian perturbation is applied to the ion density, creating localized accumulation of ion density. An initial velocity perturbation is applied to the entire ion population with the same spatial width as the density perturbation. The ion distribution function generated with this method is

$$f_i(x,v) = \frac{n_\infty}{\sqrt{2\pi}v_{\mathrm{th,i}}}\left[1+\frac{\delta n}{n_\infty}\exp\left(\frac{-x^2}{2L_{\delta n}^2}\right)\right]\exp\left(-\frac{\left(v-\delta v\exp\left(-x^2/2L_{\delta n}^2\right)\right)^2}{2v_{\mathrm{th,i}}^2}\right), \quad (5.1)$$

where δn is the amplitude of the initial density perturbation; δv is the amplitude of the initial ion velocity perturbation; $L_{\delta n}$ is the half width of the initial perturbations and $v_{\mathrm{th,i}} = \sqrt{T_i/m_i}$. The need to have both density and velocity perturbation is motivated by an ion-acoustic soliton having perturbations in both density and velocity. In order to achieve "quiet" start-up, the same density perturbation is applied to the bulk electron distribution, creating effectively zero net charge for the initialization. In this way, we eliminate the long wave length oscillations resulting from initial charge imbalance, making the simulation significantly less noisy. The same rejection scheme as the one described in Chapter 3 is used to create the initial electron phase space density perturbation that self-consistently evolves into a phase-space hole. The initial electron distribution is thus

given by

$$f_e(x,v) = n_\infty \frac{\tilde{f}_{e,0}(1-f_d)}{1-\int_{-\infty}^{+\infty} \tilde{f}_{e,0} f_d \, dv}, \tag{5.2}$$

where

$$\tilde{f}_{e,0}(x,v) = \frac{1}{\sqrt{2\pi} v_{\mathrm{th,e}}} \left[1 + \frac{\delta n}{n_\infty} \exp\left(\frac{-x^2}{2L_{\delta n}^2}\right)\right] \exp\left(-\frac{v^2}{2v_{\mathrm{th,e}}^2}\right), \tag{5.3}$$

and the dimple function f_d is given by

$$f_d = h_d \exp\left(\frac{-(v-v_d)^2}{2\sigma_d^2}\right) \exp\left(\frac{-x^2}{2\lambda_d^2}\right). \tag{5.4}$$

Recall that h_d is the dimple depth which is smaller than 1; σ_d is the dimple velocity width; v_d is the dimple initial velocity and λ_d is the dimple spatial width.

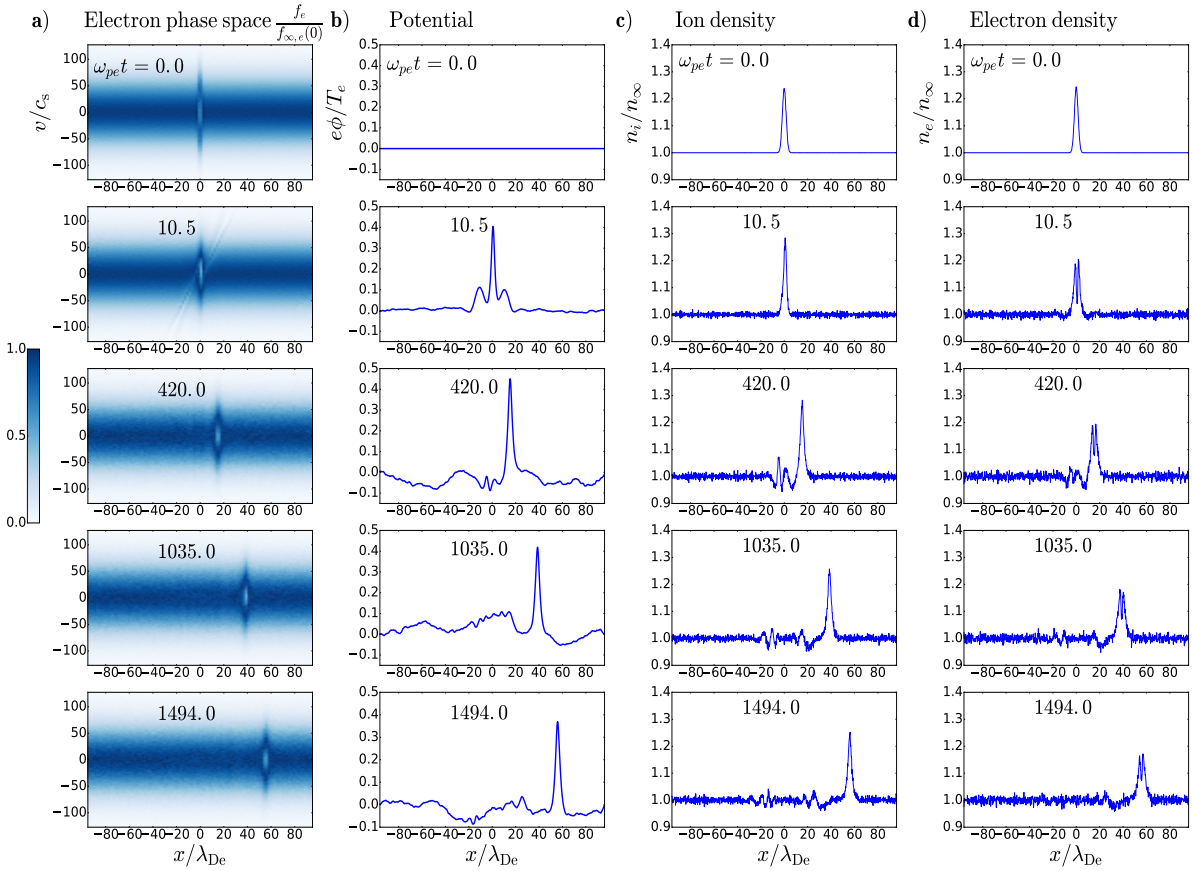

Figure 5-1: a) Normalized electron phase space density contours b) Potential, c) Ion density, d) Electron density. The plots shown on the same row are from the same time step in the simulation.

An example of an electron hole coupled to an IAS generated by this method is shown in Figure 5-1. At initialization ($t = 0$), the charge density is uniformly zero across the simulation domain. There is localized density perturbation in both ions and electrons around $x = 0$. The simulation was performed with $\delta n/n_\infty = 0.24$, $\delta v = 0.5c_s$, $L_{\delta n} = 1.6\lambda_{\mathrm{De}}$. 6.4×10^6 computing particles with 1000 spatial cells are used in this simulation and the time step is $\Delta t = 0.3/\omega_{pe}$. A "dimple" perturbation is seeded into the initial electron distribution with following parameters: $h_d = 1$, $\sigma_d = 0.95v_{\mathrm{th,e}}$, $v_d = 0$, $\lambda_d = 8\lambda_{\mathrm{De}}$. Physical mass ratio $m_i/m_e = 1836$ was used and $T_e/T_i = 20$ so the ions are a cold beam. The second row shows that shortly after the initialization, an electron phase-space hole forms self-consistently and a positive pulse appears in the electrostatic potential. Later in time ($\omega_{pe}t = 420$, third row), the initial ion density pulse breaks into a chain of ion-acoustic perturbations, with a leading compressional ion density pulse which is an ion-acoustic soliton. The initial positive Gaussian perturbation to the ion velocity makes the leading ion-acoustic soliton propagate with a positive velocity. The formed electron phase space hole is trapped in the soliton and propagates with it. The characteristic dip in the electron density associated with a hole can be seen. However, the electron density inside the solitary wave is still higher than the background density even at its lowest point. The positive charge in this newly formed solitary wave is provided by the compressional ion pulse rather than the electron phase-space hole. The solitary wave propagates with a steady velocity of $1.6c_s$ in the plasma frame and has a wave amplitude of $0.4T_e/e$, leaving behind the slower trailing ion-acoustic perturbations. The formed solitary wave is a few Debye lengths wide and stably propagates in the bulk plasma, resembling an ESW observed in space.

The final solitary wave is formed as a stable coupled state of an ion-acoustic soliton and an electron phase-space hole. This kind of nonlinear wave phenomenon in plasma has been previously documented in literature through simulations [75, 78] (though generated via different methods). The terminology differs from author to author because of the admittedly unsolved ambiguity [78] between a soliton that is described by KdV type of equation and an electron hole that emerges from Vlasov-Poisson system. We will be

addressing their key differences later in this chapter. We use the term *Coupled Hole Soliton* or CHS to refer to this coupled state in our PIC simulation. This term, first coined by Saeki and Genma [75], better portrays the nature of this nonlinear structure as we shall see later in this chapter.

It is worth pointing out that without the dimple in the initial electron distribution, the initial ion density perturbations tend to form an ion-acoustic wave train rather than the distinct soliton in Figure 5-1. The existence of an electron phase-space hole helps with the formation of the ion-acoustic soliton. These resonant trapped electrons change the dispersion relation of the wave so that it travels faster than the bulk ion-acoustic perturbations.

Study of the structure or the nonlinear dispersion relation of a steady-state CHS solution using Sagdeev's pseudo potential approach has been performed by previous authors. Saeki and Genma [75] assumed the water bag model[1] for the electron hole and Schamel [67] used Maxwell-Boltzmann distribution for the trapped electrons. In this chapter, we focus on the time dependent dynamics of these CHSs and their connections to both electron holes and ion-acoustic solitons.

II Collision of Coupled Hole Soliton (CHS) pairs

The CHS has different dynamical properties than a pure BGK mode electron hole. One characteristic that is often cited to differentiate an electron hole from a soliton is that holes merge [102, 89] during collisions when the velocity difference is small (some criterion uses the term "overlap in velocity range"), while solitons, by definition, survive collisions with other solitons unchanged. In this section, we show evidence that these CHSs have soliton-like behavior and emerge from head-on collisions that would otherwise cause electron holes to merge. Furthermore, the detailed process of their collision shows deviation from that of ion-acoustic solitons described by the KdV equation or Schamel's modified KdV

[1] The water bag model is a simplified kinetic model of a plasma. In a water bag model, the distribution function $f(x, v)$ can only take two discreet values: either $f(x, v) = A > 0$ when there are particles in the phase space volume centered around (x, v) or $f = 0$ when there are no particles.

equation [67] with resonant electrons. A hybrid behavior between a BGK mode electron hole collision and an ion-acoustic soliton collision is observed for collisions between CHSs.

To perform a collision test, we initialized two counter-propagating CHSs at locations separated by $128\lambda_{\mathrm{De}}$, using the initialization method described in the previous section. Different perturbations are applied to generate CHSs of different sizes. Four time slices of this simulation are shown in Figure 5-2. In the top two rows, two positive potential pulses representing two CHSs are propagating towards one another. Solitary ion density compressional pulses can be seen in these CHSs. Row three shows the moment when they collide. Before the two ion-acoustic solitons completely merge, the wave amplitude has already risen. This behavior is not described by the KdV type of equations for ion-acoustic solitons, in which the potential has the same shape as the ion density perturbation. At a later time step (row four), the two solitary waves re-emerge from the collision, with some distortions to their shape. The wave amplitudes are damped after collision but their velocities remain approximately unchanged. Each CHS encounters the trailing ion-acoustic perturbations behind the other after collision, contributing to their shape distortion.

For comparison, we studied the head-on collision of pure electron phase space holes with negligible ion response. We apply no density perturbations to ions nor electrons ($\delta n = 0$). The ions have no initial velocity perturbations ($\delta v = 0$) and are initialized with a drift velocity of $-10c_s$ to minimize their influence on electron holes (cf. Chapter 3). Electron distribution function is initialized with similar phase-space perturbations as we used in the previous experiment, the only difference being that now the dimples have a nonzero initial velocity in order to produce counter-propagating electron holes (previously the velocity of a CHS was determined by the initial ion velocity perturbation). Two counter propagating electron holes of similar size as before are produced and their collision is shown in Figure 5-3. The wave amplitudes are smaller because of the lack of ion contribution. The velocity difference between the two pulses is approximately $3c_s$, comparable to the value used in the previous experiment. With this velocity difference, the two electron holes have significant overlap in velocity range and theory [102] predicts

that they will merge during a head-on collision. In Figure 5-3, the last two rows show clearly that these electron holes alone don't survive a collision and they merge forming a bigger electron hole.

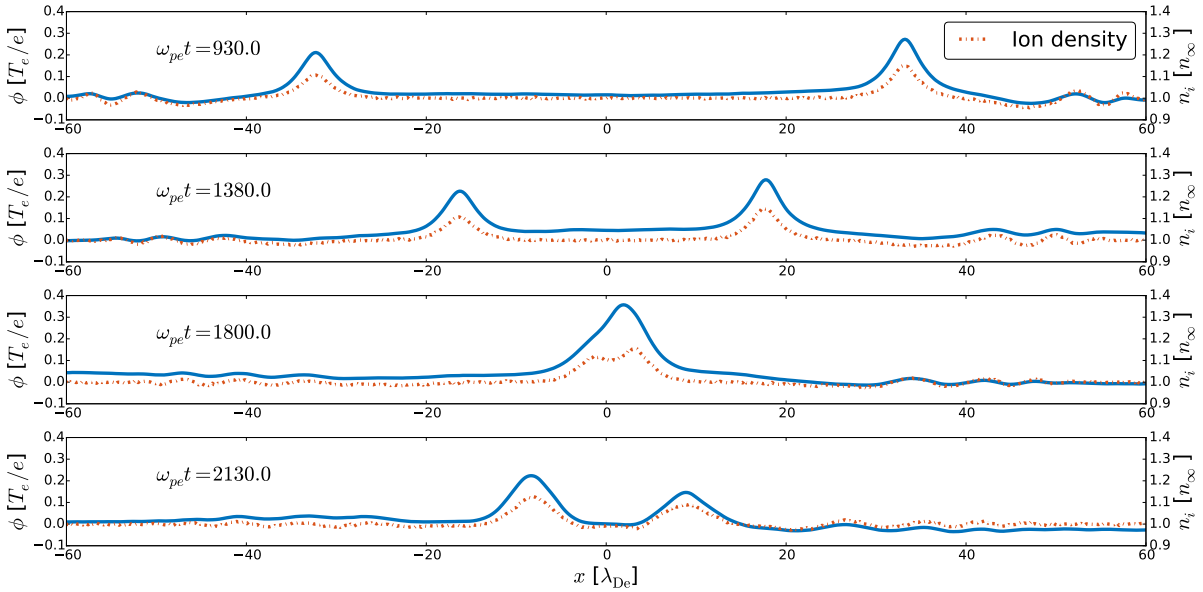

Figure 5-2: Head-on collision of two CHSs, the left CHS travels at $1.5c_s$ and the right CHS travels at $-1.5c_s$. Both electrostatic potential (solid line) and ion density (dashed line) are shown in this plot.

The collision test demonstrates a crucial difference between a CHS and a pure BGK mode electron hole. A collision of two CHSs is also different from a collision of two ion-acoustic solitons. During a collison between two typical ion-acoustic solitons described by the KdV or mKdV equation, the amplitude of the merged solitary wave follows the ion density perturbation. Wayne *et al.* [103] showed that the head-on collision of two KdV solitons can be well approximated by their linear superposition. Row three of Figure 5-2 shows a deviation from this linear superposition and an early rise in the merged waved amplitude during a CHS collision. A CHS collision exhibits important contributions from electron phase space dynamics, resulting in kinetic effects not captured by the KdV type of approach.

Electron phase space density contours are plotted to illustrate the kinetic aspect of such a collision. In Figure 5-4, we show the electron phase space and ion density side by

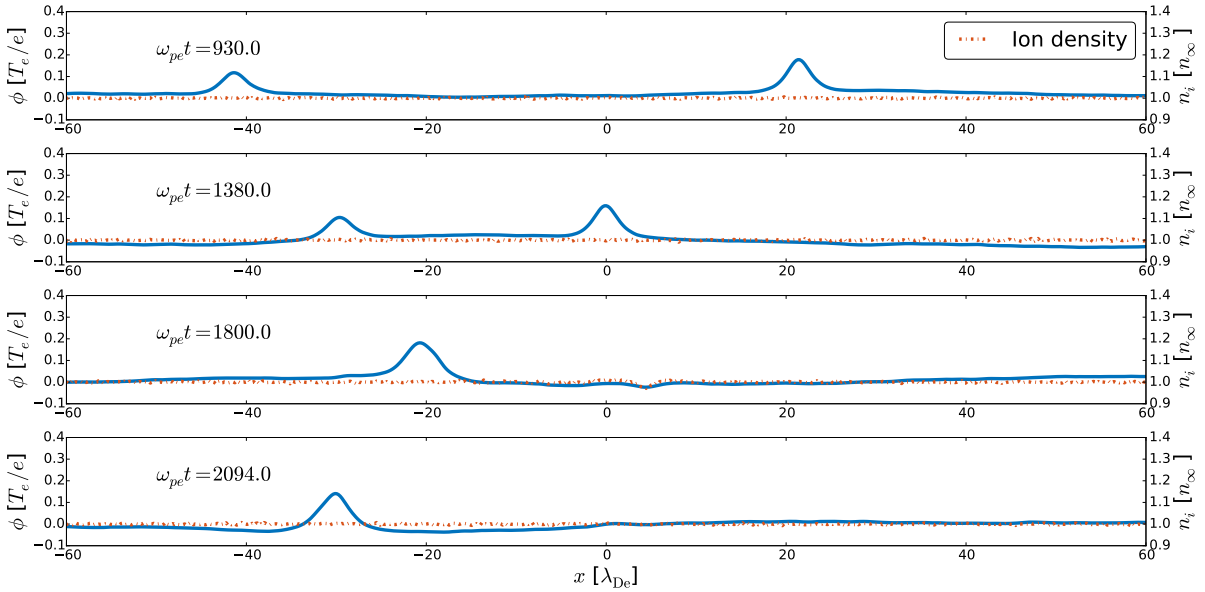

Figure 5-3: Head-on collision of similar-sized electron phase space holes with comparable velocity difference as in Figure 5-2 without ion-acoustic solitons attached, the left electron hole travels at $1.2c_s$; the right electron hole travels at $-2c_s$ and the merged hole travels at $-1.2c_s$. The electrostatic potential is shown in solid line.

side during a CHS collision. The complete picture of this collision can be decomposed into the following stages:

First, two counter-propagating CHSs encounter one another as shown in the first row of Figure 5-4. During the collision, before the two ion-acoustic solitons completely merge, the two electron holes are seen rotating around one another, which is shown in the second row. This rotation is a standard precursor of two electron holes merging [102]. Similar behavior is also observed during the merging of fluid vortices [104]. Electron holes are effectively vortices of the electron phase-space fluid. During the CHS collision, the ion dynamics are lagging behind that of the electrons due to their heavier mass. Two electron holes interact with each other and merge on a time scale faster than the ion-acoustic soliton collision can fully happen. The merged electron hole is a significant deficit of electron density between the two ion density peaks, causing a faster growth in wave amplitude during the collision. By growing the wave amplitude, the merged hole also stabilizes itself in the wave trough between the two ion density peaks. The merged electron hole can be seen in row three of Figure 5-4. By this time, the two ion-acoustic

solitons have fully merged, causing further compression in ion density as predicted by the KdV equation behavior. Ion momentum effect eventually prevails in this collision, splitting the newly formed electron hole into two parts. The hole splitting process can be seen in row four. The last row shows that each ion-acoustic soliton re-emerging from the collision then carries a part of the merged electron hole and moves away from each other. Each ion-acoustic soliton may have different resonant electrons trapped in their wave trough and the detailed trapped electron distribution is different from before the collision. This redistribution of trapped electron phase-space is entirely determined by the complex and nonlinear process of hole merging and splitting. Electron phase mixing can be clearly seen in the electron phase-space holes re-emerging from the collision, which is reminiscent of Alfvénic MHD turbulence arising from the collision of nonlinear Alfvén wave packets [105]. These effects contribute to the distortion of emerging CHS solitary waves. In this sense, the two CHSs have lost a part of their identity during this collision.

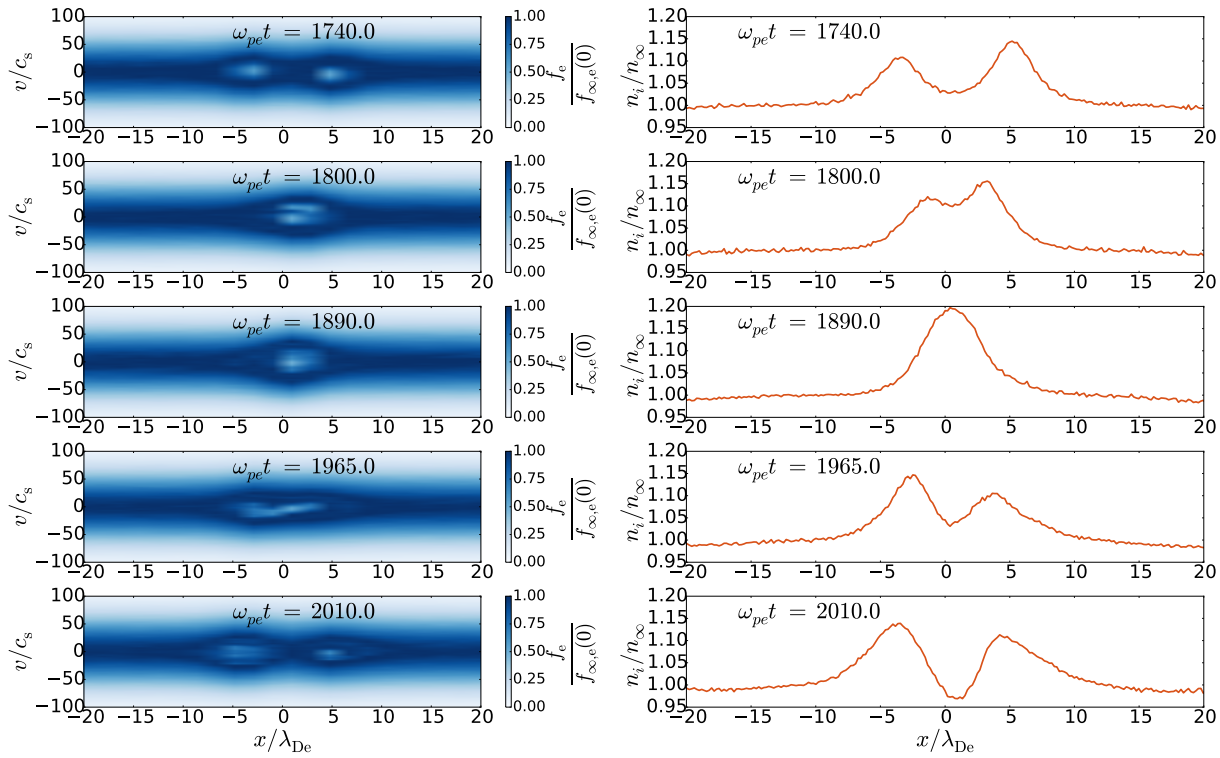

Figure 5-4: Left: electron phase space density during a CHS head-on collision. Right: ion density during the collision at the same time slices.

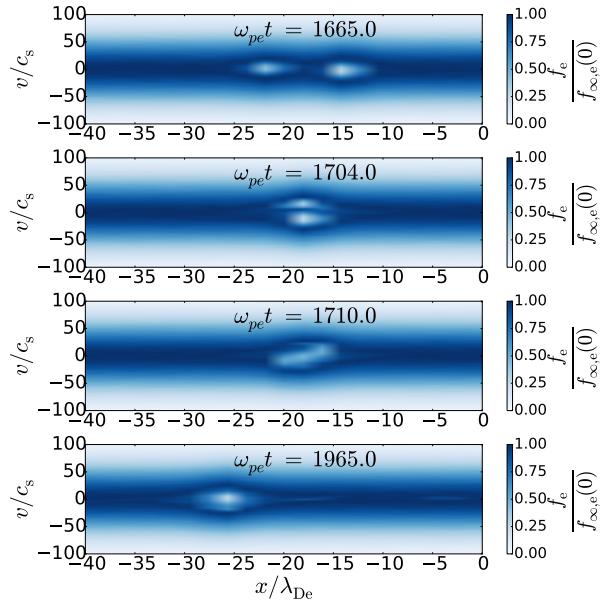

Figure 5-5: Pure electron holes not coupled to ion-acoustic solitons merging during a head-on collision.

The derivation of KdV or mKdV equations for ion-acoustic solitons generally assumes an electron equation of state $p_e(\phi)$. The electron equation of state corresponds to a quasi-stationary approximation for electrons and is therefore violated during hole interaction or merging. Finer scale electron dynamics have been lost in these derivations, which explains the observed discrepancy.

For comparison, we show two pure electron holes merging during a head-on collision in Figure 5-5. This is the same run as in Figure 5-3. Similar dynamics is observed for the hole merging process. Two holes rotate around each other and then merge. Ions are much less involved in this collision than in the previous case. Only slight ion-acoustic perturbations are noticed after the dwell time of hole merging.

III Velocity gap and transition between two states

III.1 Velocity gap between CHS and BGK states

We have extensively explored the generation of CHSs with different initializations. Our data show that stable CHSs have extensive overlap in wave amplitude with electron holes,

but there is a distinct gap between their velocities in the ion frame. This velocity gap is caused by the oscillatory velocity instability that we discussed in Chapter 4.

In Figure 5-6, we plot the velocity of stationary solitary waves in the ion frame (also the plasma center of mass frame) measured in cold ion sound speed c_s versus the solitary wave amplitude measured in T_e/e. All the data points are from our PIC simulation. Different initial perturbations are applied to generate different sized solitary waves. In general, when the initial ion density and velocity perturbations are reduced, BGK mode electron holes are generated instead of the CHSs. These electron holes only have small ion compressional pulses attached to them as ion response to their potential. Most of the positive charge in these electron holes is provided by the deficit of electrons rather than the compression of ions. Their velocity is determined by the velocity at which they are generated in the electron distribution and the transient acceleration from ions as we discussed in Chapter 2 and 3. For this reason, there is no obvious correlation between their wave amplitude and velocity. Space observations also confirm that electron holes can have a wide range of velocity at similar amplitude [99].

However, when an electron hole forms a stable coupling with an ion-acoustic soliton, the combined CHS has a velocity that is positively correlated to its amplitude as shown by triangles in Figure 5-6. Again this property confirms the soliton-like nature of a CHS. A bigger CHS travels faster like in the case of a soliton. A CHS travels slightly faster than its typical ion-acoustic soliton counterpart, which can be confirmed from the nonlinear dispersion relation [67] taking into account the fewer resonant electrons.

The velocity gap between the CHSs ("coupled state") and BGK mode electron holes ("free state") is clearly shown in Figure 5-6. We know from our analysis in Chapter 4 that when the velocity of an electron hole is slower than a threshold value, it encounters the *oscillatory velocity instability*. This explains why the upper points representing electron holes do not go significantly below the oscillatory velocity stability boundary plotted for Schamel type of hole potential. The existence of another stable branch of CHS deeply beneath the stability boundary was not covered by our analysis, although we hinted at the possibility of its existence in the last section of Chapter 4. The linear stability analysis

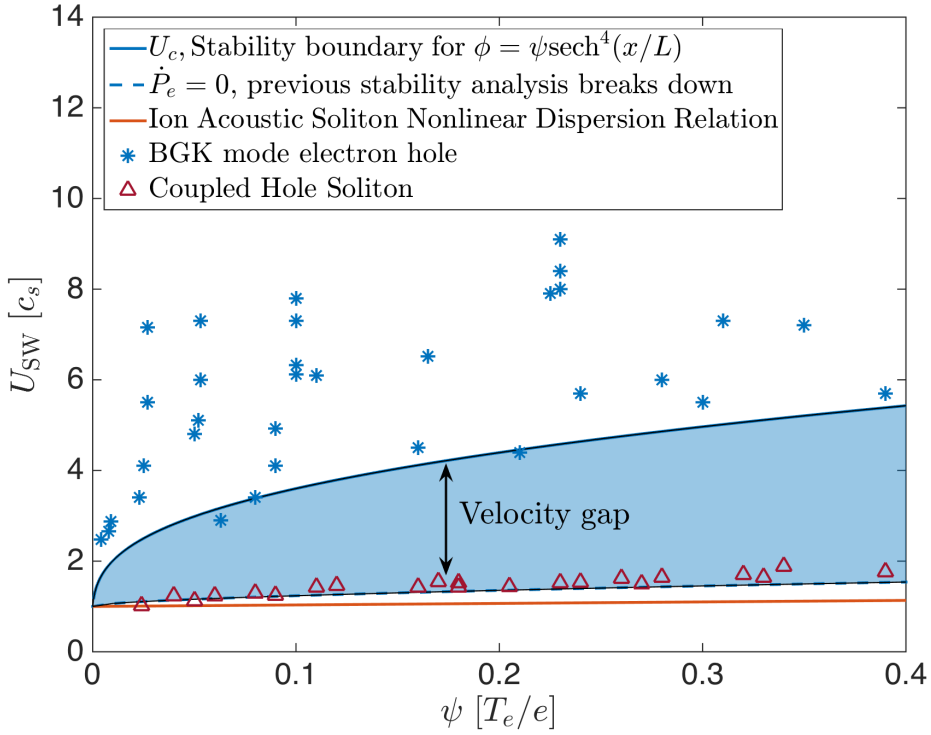

Figure 5-6: Velocity and amplitude of the solitary waves observed in our PIC simulation showing the velocity gap between two different states of electron holes.

we performed was based on approximations that are valid in the vicinity of the stability boundary. However, these assumptions break down when the wave velocity is significantly lower than the threshold value. When we approach the CHS branch, the ion contribution to the total wave potential becomes important and the principal eigenmode is no more the Goldstone mode that we have assumed in our analysis. The approximation $\psi/U^2 \ll 1$ also deteriorates when the wave velocity approaches c_s. We take the singular points where $\dot{P}_e = 0$ for a Schamel type of hole potential in our previous stability analysis to delimit the lower stability boundary. It is plotted by the dashed line in Figure 5-6. Our stability analysis should break down above this line. A mathematically rigorous treatment for the stability of CHSs and the exact lower stability boundary is beyond the scope of this thesis. The lower bound of the shaded gap region in Figure 5-6 should be taken from a qualitative perspective rather than quantitative. Empirically, it is found that these stable CHS solutions indeed cluster around this boundary as shown in Figure 5-6.

This velocity gap is caused by an instability mechanism that involves the dynamics of both species in plasma. It is thus absent from the theory of CHS using Sagdeev's potential by Saeki and Genma [75]. A Sagdeev's potential approach constructs a stationary solution of which the stability is not guaranteed. Furthermore, it is important to perform the simulation with the physical ion-to-electron mass ratio for the clear observation of this velocity gap. As we have demonstrated in Chapter 4, an artificially reduced mass ratio will lower the upper stability boundary because of its mass ratio scaling, reducing the velocity gap. The use of significantly reduced mass ratio as low as $m_i/m_e = 100$ makes it difficult for some previous studies to observe this velocity gap.

When the electron hole happens to be generated in the unstable region of the parameter space, instability is observed and the electron hole eventually settles down to one of the two stable states. Deviation from the oscillatory velocity instability is observed for unstable electron holes that are significantly below the upper stability boundary. Both deformation and shift of the solitary wave are observed during the instability. The details of this instability will be discussed in the following subsections.

III.2 Transition from CHS to BGK by ion Landau damping

In this subsection, we show that the ion-acoustic soliton in a CHS can be significantly damped by ion Landau damping when finite ion temperature effects are important. The CHS becomes unstable with damping and the electron phase-space hole breaks the coupling during instability, becoming a "free" BGK electron hole.

Ion-acoustic solitons are known to be subject to ion Landau damping [106]. A CHS travels at a velocity slightly higher than the ion acoustic velocity. When the ion temperature becomes comparable to or higher than the electron temperature, there is a non-negligible number of ions traveling at the same phase velocity as the wave. These ions damp the ion compressional pulse of the CHS. With a disappearing ion-acoustic soliton, the CHS gradually becomes unstable as shown in Figure 5-7. The first row shows an initially stable CHS. The ion density accumulation inside the CHS diminishes over time. Eventually the ion density peak gets dispersed and a doubled-humped structure forms in

the ion density as shown in row three. The electron hole trapped inside the ion-acoustic soliton begins to have serious excursions, distorting the wave form. The overall ion density perturbation is still moving at a velocity slightly higher than c_s but the electron hole is bouncing inside it from one side to the other with a growing oscillating velocity (row three and row four). Eventually, the electron hole is released from the ion trap by this instability, becoming a free BGK electron hole traveling steadily at a higher velocity than before. The jump in velocity approximately corresponds to the velocity gap between the two states. The wave amplitude shrinks during the damping and subsequent instability.

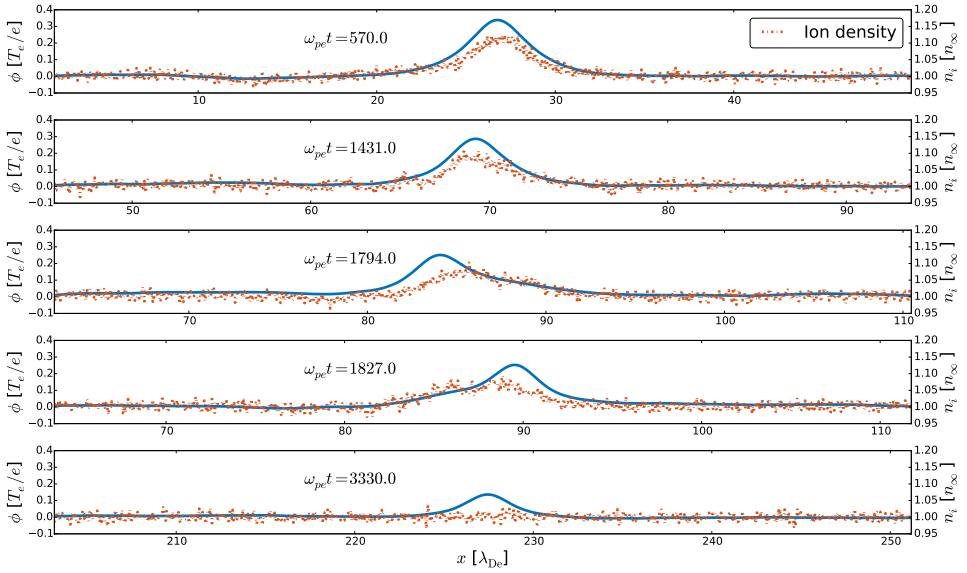

Figure 5-7: Long-term evolution of a CHS in a plasma where $T_e/T_i = 5$ shows instability while the ion density compressional pulse is damped away by ion Landau damping. The electrostatic potential is shown in solid line and the ion density is shown in dashed line. The last row shows the final free electron hole released from the CHS by instability. Hole tracking simulation is used to track the long-term behavior of this solitary wave. The x-coordinate is with respect to the lab frame.

In terms of the (U, ψ) parameter plane we have introduced, the CHS starts at $U = 2c_s$, $e\psi = 0.34\, T_e$, ion Landau damping causes the wave amplitude to shrink while its velocity approximately remains the same. This corresponds to moving horizontally to the left in the (U, ψ) plane until we encounter the instability boundary at $e\psi = 0.29\, T_e$. Eventually the free BGK electron hole stabilizes at $U = 5.6c_s$ and $e\psi = 0.12\, T_e$ after the jump in its velocity. Time evolution of the wave velocity in the ion frame is plotted in Figure 5-8.

The oscillations and the final transition can be clearly viewed from the velocity change.

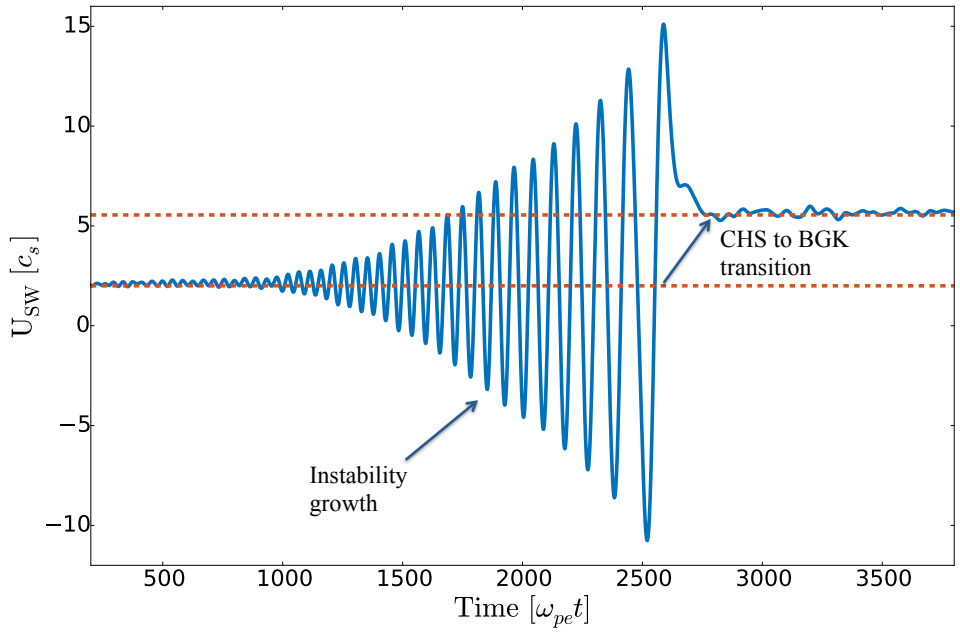

Figure 5-8: Velocity of the solitary wave during and after the instability showing the transition, the velocity is measured by hole tracking algorithm described in Chapter 3. A low-pass filter of cutoff frequency $0.03\omega_{pe}$ is applied to the velocity time series to eliminate high-frequency noise.

The ion Landau-damping-induced instability and transition become more pronounced hotter the ions are. Ion reflection from the solitary wave front also becomes important, accelerating the CHS during instability. All these effects contribute to a faster transition from a CHS to a BGK electron hole in a plasma with warm ions.

III.3 Transition from BGK to CHS by hole growth

Previously, we have demonstrated the transition from a CHS state to a free electron hole by ion Landau damping. Now we show that by growing the amplitude of an electron hole fast enough using a rising background plasma density, an electron hole may go through the unstable region and excite enough ion perturbations to stably couple itself to form a CHS. When an electron hole is placed in rising background density, its effective depth

grows because the passing population density is rising while the trapped distribution remains unchanged. This causes the electron hole to grow, grabbing more phase space volume from the passing orbits. This hole growth mechanism has been treated in detail in the work by Hutchinson *et al.* [107] It explains the growth of electron holes in the plasma wake of an object. We have proved in Chapter 2 that a growing electron hole will accelerate in the ion frame through the growth jetting effect, making it difficult to couple a growing hole to the ions if there is only one ion stream. The way to get around this is to use two counter-propagating ion streams and initialize an electron hole that is between them in the velocity range. So in the hole frame, the two ion streams are coming from opposite directions and the growth jetting effects from the two streams will cancel each other. In this way, we can grow an electron hole that remains relatively stationary in the ion frame. This is the method we adopt to carry out this numerical experiment.

We start the simulation using a domain that is $96\lambda_{\mathrm{De}}$ wide. The ions are composed of two counter-propagating cold beams with $T_e/T_i = 20$ traveling at $\pm 4c_s$ in the simulation frame. An electron hole of amplitude $0.1T_e/e$ is generated in the center of the domain. It is generated at the center of electron distribution such that its velocity is zero in the simulation frame. The velocity of the ion beams and the electron hole size are chosen so that the system is not subject to ion-acoustic or hole velocity oscillatory types of instabilities. We grow the background plasma density in our simulation after the hole forms by injecting a growing number of particles into the simulation domain. The background plasma density grows exponentially as $\sim \exp(\gamma_b t)$, with $\gamma_b = 1 \times 10^{-3}\omega_{pe}$. Like in a plasma wake, the rising electron density fills in the simulation domain faster than the ions, forming an ion-attracting potential well in the simulation domain. The central electron hole climbs up this potential well like an electron. It grows in size upon encountering higher density electron phase space fluid. We show the potential and ion density evolution of this rising density simulation in Figure 5-9. The first two rows show the initial BGK electron hole with little ion response, it moves to the right climbing the density gradient and grows in amplitude. It then encounters the oscillatory velocity instability after its amplitude reaches approximately $0.3\,T_e/e$. The oscillatory velocity

instability creates trailing ion-acoustic perturbations around the electron hole, which can be seen in rows three and four. The background density growth is stopped at $\omega_{pe}t = 1200$ when the background density reaches about 3.2 times its initial value. Because the ions are counter-propagating, the final ion density first establishes at the center of simulation domain so the potential inverts its concavity after the end of density growth, sending the electron hole back to the center. We notice that the instability gradually diminishes after the wave amplitude reaches above $2\,T_e/e$. The final solitary wave grows to about $3\,T_e/e$ in amplitude and propagates steadily at a velocity of $-0.5c_s$. Ion density compressional pulse dominates in this final solitary wave and it is effectively a CHS.

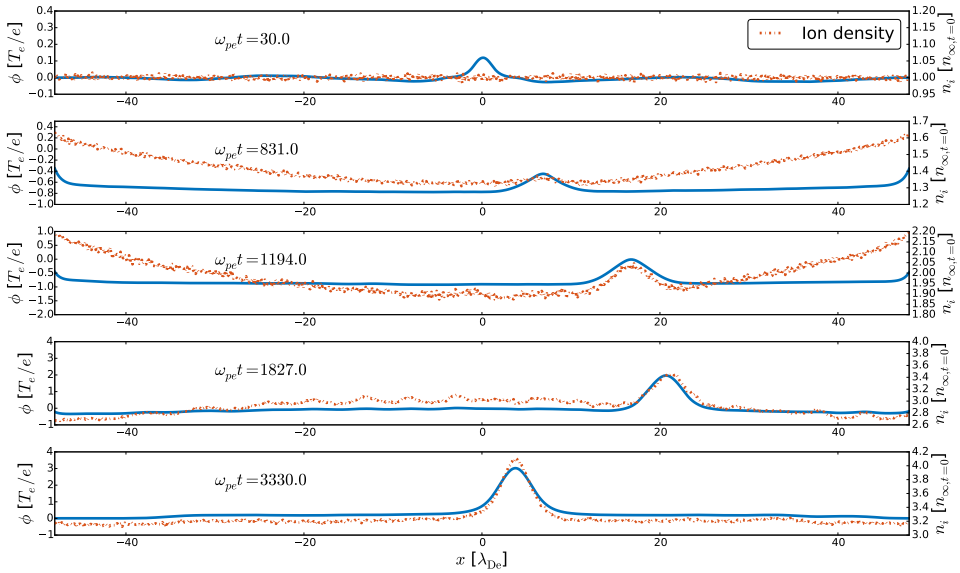

Figure 5-9: Electrostatic potential and ion density during the growing density simulation. Background density growth starts at $\omega_{pe}t = 30$ and ends at $\omega_{pe}t = 1200$.

In a similar way as before, this state transition can be visualized by plotting the velocity evolution of this solitary wave, which is shown in Figure 5-10. The oscillation amplitude grows as well as its frequency. The frequency chirp of unstable oscillations is predicted by our stability analysis in Chapter 4 as the wave amplitude ψ grows bigger. At around $\omega_{pe}t \simeq 1600$, the solitary wave reaches the lower stability boundary in (U, ψ) plane and begins to stabilize itself. The oscillation amplitude shrinks sharply as the wave makes its transition to a stable CHS.

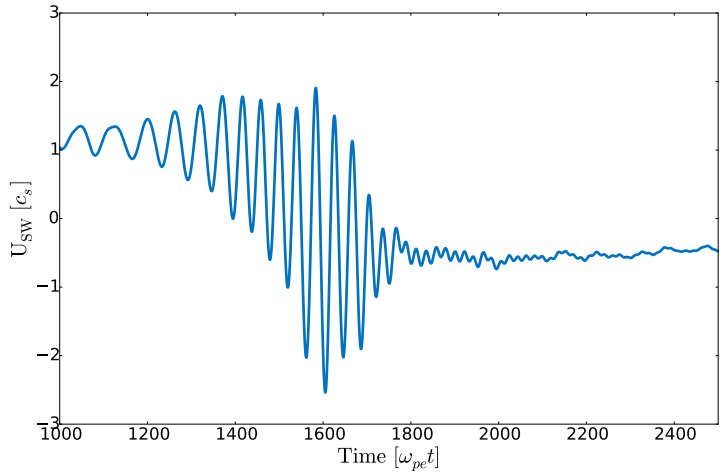

Figure 5-10: Velocity of the solitary wave during the rising density simulation. The wave converges to a stable CHS state. The same low-pass filtering is applied as in Figure 5-8.

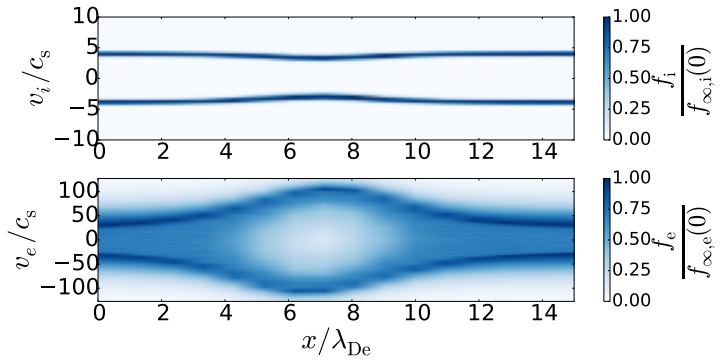

Figure 5-11: Top: ion phase space of the CHS at $\omega_{pe}t = 3330$. Bottom: electron phase space of the CHS at $\omega_{pe}t = 3330$.

The final CHS obtained from the rising density simulation reaches an amplitude of $3\,T_e/e$, a significant amount of the electron phase space is trapped inside this solitary wave. A plot of its phase space structure is shown in Figure 5-11. Perturbations to the two ion streams can be seen in the ion phase space. If the wave grows further, it will eventually disrupt the counter-propagating ion streams as seen in the kinetic plasma wake simulation performed by Haakonsen *et al.* [57] Previously in the kinetic plasma wake simulation, the central big electron hole is observed to have very different dynamics than the smaller ones that are accelerated to a high velocity by the wake electric field. The big electron hole moves at an almost constant velocity, slowly drifting in the wake. The current study

shows that by transitioning into a stable CHS during growth, this big electron phase space vortex is trapped inside an ion density compressional pulse formed by its rising amplitude. Ion scale dynamics dominate inside the CHS, hence it behaves differently than the other smaller electron holes. In Haakonsen's original wake simulation, the ions have the same temperature as the electrons so ion Landau damping is not negligible as we have seen in the previous subsection. However the fast growth from the rising density can completely overwhelm the damping from finite ion temperature effects.

When the density growth rate is not enough to overcome the oscillatory velocity instability, the electron hole is seen torn apart by the instability and leaves the domain fast by strongly interacting with one of the ion streams.

IV Buneman instability and CHS formation

So far we have shown examples where artificial density perturbations are used as seeds to generate electron holes or CHSs. In this section, we show the generation of electron holes and CHSs during Buneman instability simulated with PIC simulation. Buneman instability is driven by the relative velocity drift between electrons and ions in a plasma. It is one of the kinetic instabilities that are often cited to be responsible for the generation of electron holes in space plasma [33]. Let us denote the relative drift velocity of electrons in the ion frame as $v_{d,e}$, a linear stability analysis gives that Buneman instability is excited for a equal temperature $T_i = T_e$ plasma when [12]

$$v_{d,e} > 1.3\sqrt{\frac{T_e}{m_e}}. \tag{5.5}$$

This threshold value is reduced below the electron thermal speed when the ions are cold. Buneman instabilities are simulated with different electron-to-ion temperature ratios using 1D open boundary PIC simulation. It is found that Buneman instability results in formation of CHS-like structures when the ions are cold and only free BGK electron holes are observed when the ion temperature is equal to that of the electrons. A clear example of such observation is shown in Figure 5-12. Ions have zero drift velocity in the simulation

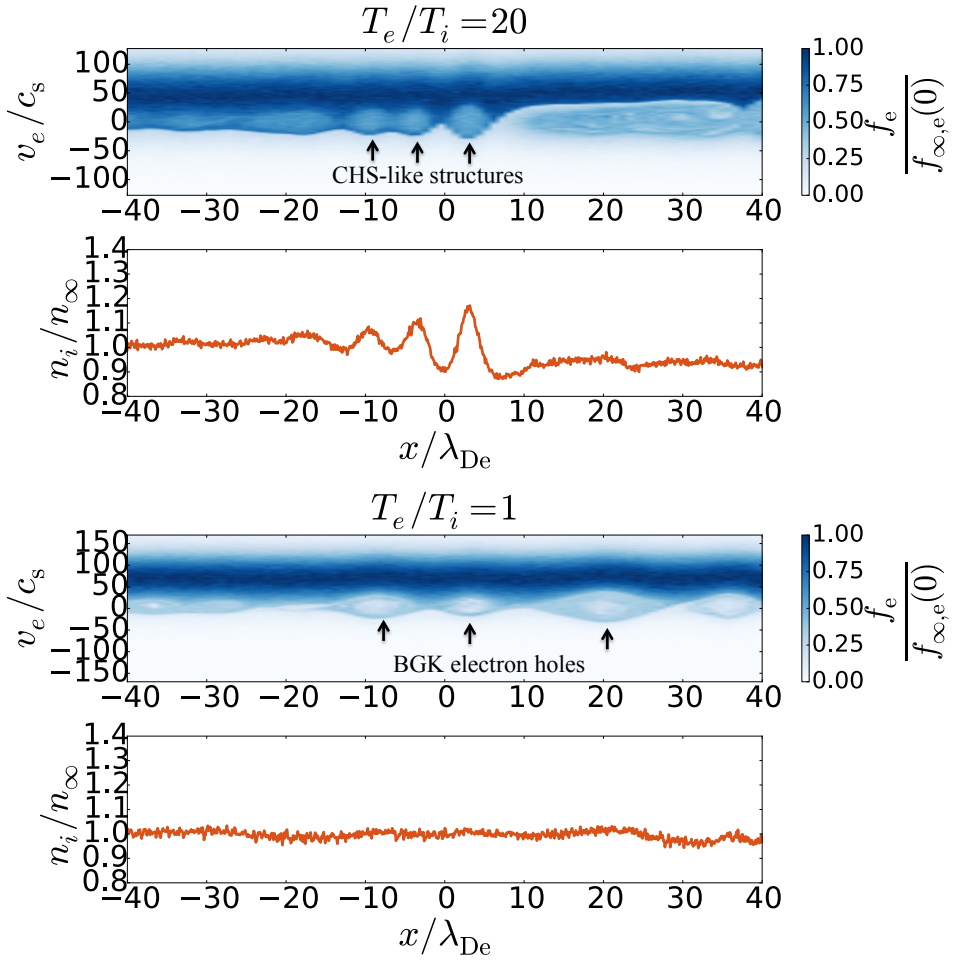

Figure 5-12: Top: Buneman instability simulation with cold ions shows formation of CHS-like structures, traveling slightly above $1c_s$ in the ion frame. Bottom: Buneman instability simulation with a hotter ion population only shows formation of BGK electron holes, traveling between $4c_s$ and $5c_s$ in the ion frame, above the stability threshold velocity.

frame. In the cold ion stream run with $T_e/T_i = 20$, the electrons have a drift velocity of $v_{d,e} = 45c_s$, which is comparable to the electron thermal velocity. A chain of electron holes can be seen forming behind a double-layer like structure in the electron phase space. They are all attached to ion density perturbation peaks. This is shown by the top two panels of Figure 5-12. They travel in the ion frame with a velocity slightly above the ion sound speed and bigger CHSs travel faster than the smaller CHSs, resulting in their separation.

The equal temperature $T_i = T_e$ run was performed with a higher electron drift velocity

$v_{d,e} = 70c_s$ in order to satisfy the more stringent instability criterion set by Equation (5.5). In this case, only BGK type of electron holes are seen forming in the simulation with small ion perturbations as shown by the bottom two panels of Figure 5-12. These electron holes also have a higher velocity (above $4c_s$) in the ion frame as it would be expected from their different nature.

The above results show that Buneman instability with cold ions tends to form electron holes in CHS states while BGK type electron holes are formed for a warmer ion population.

V Implications for space observation

The results we show so far in this chapter have important implications for the observation of ESWs by satellites. Our simulation predicts a velocity gap between two different states of electron holes. It remains to be seen if satellite data can confirm this. The challenge right now is that the ESWs observed are rather weak in amplitude ψ, most often between $0.01\,T_e/e$ and $0.1\,T_e/e$ [99]. The velocity gap shrinks significantly when the wave amplitude approaches zero. Also satellites may observe an unstable non-stationary electron hole. We have seen that in an unstable CHS, the electron hole oscillates in ion density perturbations extending several Debye lengths for an extended period of time, both the spatial scale and time scale of this oscillation may well exceed the distance between sensors and time delay used to infer the wave velocity. The satellites can effectively "see" the instantaneous velocity of an unstable electron hole. It is worth pointing out that the ion temperature is significantly hotter ($5-10$ times hotter) [91, 99] than the electron temperature in the plasma regions where these slow ESWs are observed. The ion Landau damping effect we have discussed indicates that both stable and unstable CHSs can only exist for a short period of time. They may still be observed if born close enough to the satellites. Furthermore, our results provide a way to study quantitatively the coupling strength between an electron hole and the ions with available observational data. Electric field sensors are most often the plasma diagnostic with the highest time resolution available on a satellite [43]. Ion and electron density are measured with much less time precision

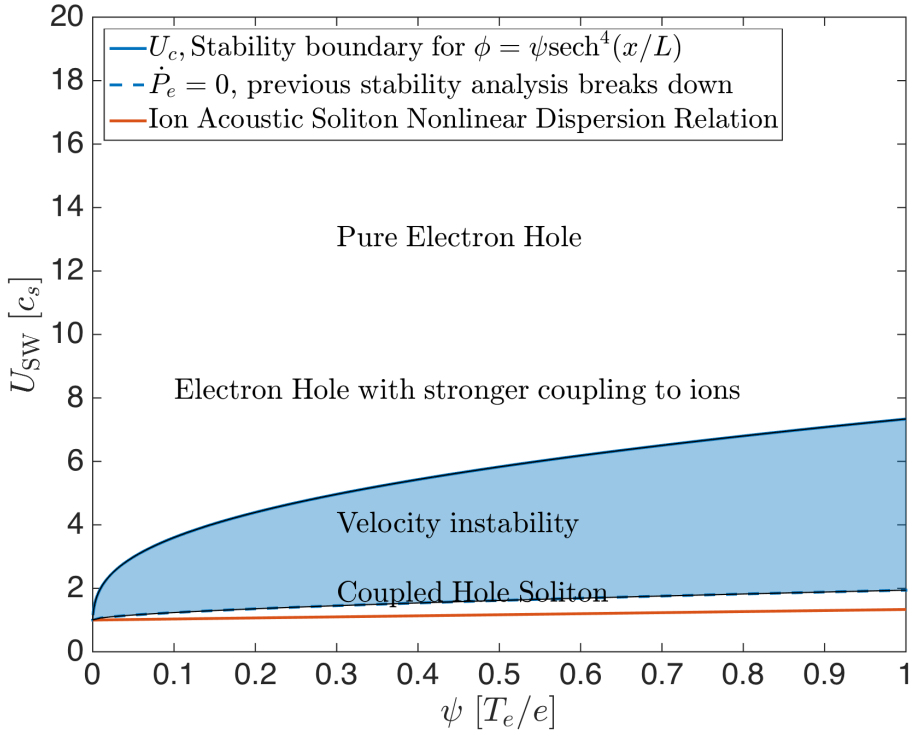

Figure 5-13: The velocity-amplitude parameter plane. The velocity is normalized to cold ion sound speed and the amplitude is normalized to electron temperature. The BGK mode free electron holes are separated from the CHSs by the shaded region, which represents the oscillatory velocity instability.

[92], which is not enough to resolve the density perturbations inside an ESW traveling at several hundred kilometers per second in the satellite frame. Therefore it is difficult to rely on the density data to tell the nature of an ESW. We suggest using the plot shown in Figure 5-13 to classify the coupling between an ESW and the ions. One could simply plot the ESW speed in the ion frame in unit of ion sound speed versus its amplitude in unit of electron temperature in this parameter plane to determine its nature. Different coupling strengths to ions suggest different generation mechanisms. In Figure 5-14, we have plotted the observational data from Cluster spacecraft. More data are required to determine if there is actually a velocity gap between faster and slower ESWs from space observations. However, the ones that are called slow ESWs or slow electron holes indeed cluster near the CHS/IAS branch. A fast moving electron hole with little coupling to the ions is likely to be generated by electron bump-on-tail type of instability while slow

electron holes with stronger ion coupling and CHSs are more likely to be generated by Buneman instability. The ESWs that have stronger coupling to ions are more likely to drive anomalous resistivity in space plasma.

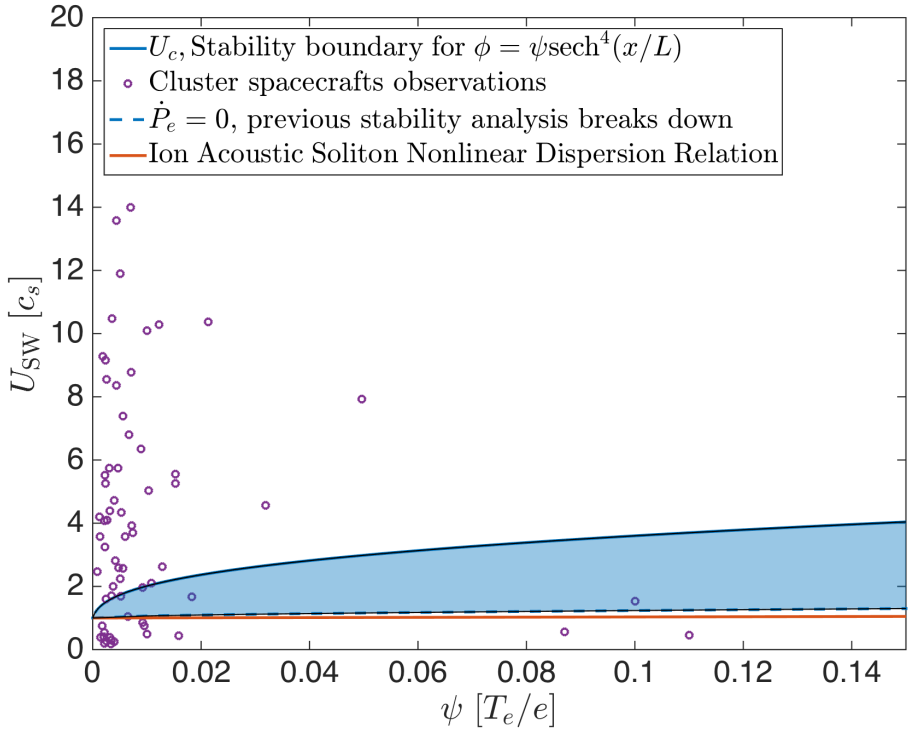

Figure 5-14: The observational data from Cluster spacecraft are plotted in the velocity-amplitude parameter plane. The ones with speed close to c_s are referred to as the "Slow Electrostatic Solitary Waves". These data are published in references [92, 99].

VI Conclusions

In this chapter, we have demonstrated stable embedding of an electron phase-space hole into an ion-acoustic soliton in a one dimensional Particle-In-Cell simulation, forming a stable Coupled Hole Soliton, which is a coupled state of a fluid soliton and a phase-space vortex. We have performed head-on collisions of CHSs in PIC simulation. The collision test shows that CHSs can survive collisions with small relative velocity difference. Its detailed behavior during collision is a hybrid of soliton collision and vortices merging. A statistical study of the velocities of CHSs reveals a velocity gap between CHSs and BGK

electron holes, which can be explained by the oscillatory velocity instability. Transition between a CHS state and a BGK state is possible in both directions. CHSs can be generated by Buneman instability when the ions are a cold stream. Our findings are important for the better understanding of the boundary between electron holes and solitons. Our results are also useful for interpreting satellite data of space observations.

Chapter 6

Conclusions and future work

I Conclusions

The current thesis presents comprehensive original research work on BGK mode electron holes in collisionless plasma. It contributes to the field of plasma physics in both fundamental and more applied aspects. Fundamentally, the new physical understandings conveyed by this thesis are:

- The velocity and dynamics of electron holes are governed by total plasma momentum conservation, hence ions play an important role in determining the velocity of electron holes. The "jetting" effect has important implications for momentum transfer. Slow electron holes have strong momentum coupling to the ions. The strength of this coupling is determined quantitatively in this thesis. This point was discussed in Chapter 2.

- A new type of BGK mode instability is discovered as part of this thesis work. An electron hole traveling slower than a few times the ion sound speed in the ion frame experience unstable oscillations in its velocity. The instability involves interplay of both electron and ion dynamics. A 1-D analytic treatment of the instability is given in this thesis. The analytic treatment can fully explain the instability thresholds and frequencies observed in simulations and the growth rates are explained in the

weakly unstable cases. This instability mechanism can contribute to the anomalous resistivity observed in space plasma. Chapter 4 discussed this point.

- The holistic object treatment of the electron hole yields fruitful outcomes. The Goldstone/shift mode, which is a derivative of the steady state solution, is an important destabilizing eigenmode of an electron hole solution. This point can also be found in Chapter 4.

- The methodology and mathematical techniques developed in this thesis work (Chapter 4) such as the derivation of a dispersion relation/response function for a nonlinear solitary wave can potentially be applied to the study of other nonlinear wave phenomena such as double layers and shock fronts in plasmas.

- An electron hole can form a stable coupled state with an ion-acoustic soliton to travel near the ion sound speed in the ion frame. This coupled state is separated from the classical BGK mode electron hole by the oscillatory velocity instability. The coupled hole soliton pair exhibits more soliton-like properties, though stronger kinetic electron effects make it behave differently than a fluid soliton. This thesis work makes an important step forward in explaining the ambiguity and boundary between an electron hole and a soliton. Chapter 5 discussed this point.

- Transition is possible between a coupled hole soliton state and a classical BGK mode electron hole. This is a demonstration of transition between different nonlinear wave phenomena in a plasma. Chapter 5 covered this point.

This thesis also provides important insight in some more practical aspects:

- A novel Particle-In-Cell code that can self-consistently track and simulate a fast moving electron hole is implemented in this thesis work. It successfully applies the concepts from control theory to numerical simulation of a plasma. The flexibility, reliability and feasibility of this moving-domain feature-tracking simulation technique is demonstrated. Similar methods can be implemented to study the long-time

dynamics of other propagating nonlinear phenomena such as the shock wave. This point was discussed in Chapter 2.

- This thesis introduces a practical parameter plot to study the coupling of an electrostatic solitary wave to ions, which can be readily applied to the analysis of space probes data. This point can be found in Chapter 5.

- The thesis work predicts a new type of electron hole instability and a velocity gap between two different states of electron holes that can be potentially observed and verified. It gives directions to researchers working on the experimental side about where they should be looking at to find these new phenomena. These points were discussed in Chapter 4 and Chapter 5.

II Future directions

This thesis opens up directions for important future work. First, the present work only deals with one-dimensional electrostatic kinetic plasma. Though this choice is justified in the thesis, the natural next step is to go to higher-dimensional and finitely magnetized plasma. We have mentioned the unsolved transverse instability of an electron hole in higher dimensions. This thesis work sheds light on understanding the transverse instability and paves a way to solving it. An example of the hole transverse instability is shown in Figure 6-1. The PIC simulation is two-dimensional in space and three-dimensional in velocity to simulate a magnetized plasma. The ions form a uniform neutralizing background. The electron hole potential can be seen along the magnetic field direction (axis 1). In the two-dimensional case, the electron phase space structure is rather a phase-space tube that extends in the transverse direction. The magnetic field strength is such that $\Omega_e = 0.2\omega_{pe}$. Kinking of an electron hole in the transverse direction happens when the magnetic field strength is weak such that $\Omega_e < \omega_b$, where ω_b is the parallel bounce frequency for the trapped electrons. No analytic treatment so far has obtained the eigenmode consistent with what was observed in numerical simulations [53]. The destabilizing mode is an odd eigenmode with respect to the center of the electron hole, which depends on the transverse

direction y as $\exp(iky)$. This eigenmode appears to be the Goldstone or shift mode that was analyzed in this thesis. When the magnetic field strength is weak and an electron with a transverse velocity $v_\perp$ can have important excursion in the transverse direction, it effectively sees an oscillating hole potential with a frequency $v_\perp k$. There is hole momentum "jetting" effect in the parallel direction resulting from this oscillating hole potential. An analytic treatment showing that the Goldstone mode can be driven unstable under these conditions seems very hopeful. If this intuition turns out to be correct, then the transverse instability is a result of the entire electron distribution, rather than a trapped electron mode suggested by the past literature [53].

As an improvement on the work presented in this thesis, the electron momentum rate of change can be extended to the entire frequency domain, with resonant electron effects taken into account. A low frequency approximation for the electron response is derived in this thesis work which neglects resonant electron effects. These approximations have been justified in the thesis and the good agreement with simulations further strengthens our confidence in these expressions. However, if the transverse instability needs to be pursued in a similar way, then a full expression for the electron response is important. A first attempt at this is shown in Section III of Chapter 4 using a linearized Vlasov-Poisson approach. Another aspect that can be worked upon to make this thesis work more mathematically rigorous is the treatment for electrons near the separatrix where the short-transit-time approximation breaks down. A more mathematically rigorous way to neglect them may be possible.

In this thesis, it is shown that there is a new branch of stable solitary waves deeply beneath the oscillatory velocity instability boundary, which is the Coupled Hole Soliton pair (CHS). Its stability, though demonstrated in PIC simulation, has not been proved using an analytic theory. A possible future direction is to actually derive their stability and the stability boundary. The Goldstone mode can no longer be justifiably used for this calculation as the ion soliton contribution to the potential is important. The non-centering of the electron hole and the ion-acoustic soliton leads to deformation of the hole potential rather than a simple shift.

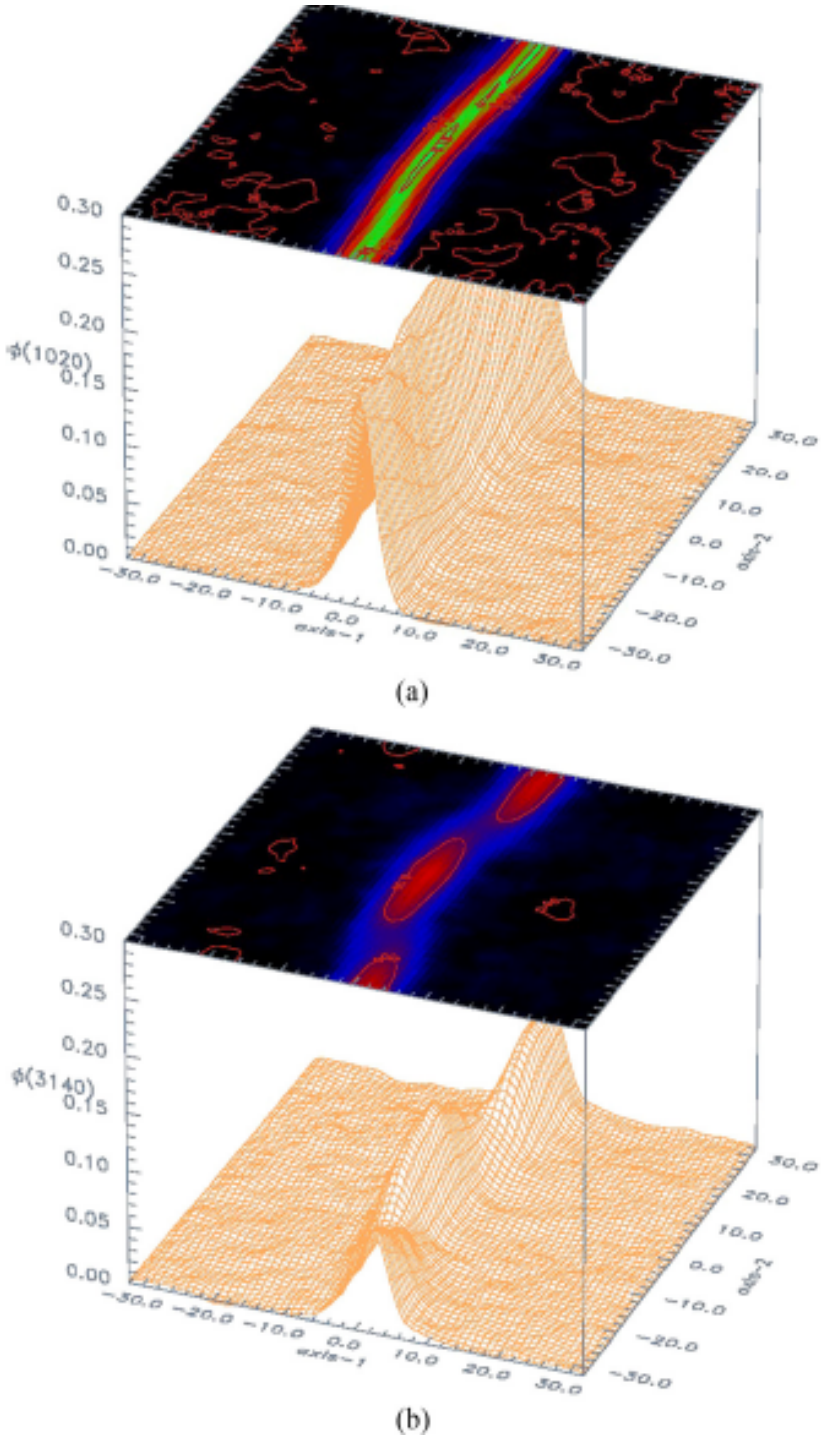

Figure 6-1: Transverse instability of a two-dimensional electron hole. The magnetic field is along axis 1. The top panel (a) shows the simulation at $\omega_{pe}t = 204$, the bottom panel (b) shows the simulation at $\omega_{pe}t = 628$. Courtesy of I. H. Hutchinson

This thesis predicts phenomena that can potentially be observed in the laboratory and in nature. Satellites provide rich data of electrostatic solitary waves encountered in space. Mining these data for the evidence of the phenomena described in this thesis will be interesting future work. Especially finding the velocity gap and classifying different types of electrostatic solitary waves in a big data set will make meaningful use of modern machine learning techniques. It is also possible that the phenomena described in this thesis can be directly observed in the laboratory plasma experiments. Lefebvre *et al.* [37] have demonstrated generation of electron holes using superthermal electron beam injection at the upgraded Large Plasma Device. It is shown in this thesis that Buneman instability is an effective way to generate electron holes that are strongly coupled to the ions and Buneman instability with cold ions tend to generate CHSs. A possible way to excite Buneman-type instability with a similar experimental setting is to inject subthermal electron beam that preferentially interact with the ions. The follow-up experimental work can use these guidelines to generate and explore slow electron holes in the ion frame. This is a rarely explored regime in which the present thesis work predicts interesting physics.

Appendix A

Initial electron distribution generated by rejection method

We give a proof for Eq. (3.7) in this subsection. Consider the infinitesimal phase space area $dxdv$ centered around (x, v). For a given electron density n_0, the number of electrons that are distributed to this phase space area after Step 1 and 2 is $n_0\tilde{f}_{e,0}(v)\,dxdv$. The number of electrons rejected after Step 3 is

$$N_{\text{rejected},1}(x, v) \;=\; n_0\tilde{f}_{e,0}(v)f_d(x, v)\,dxdv. \tag{A.1}$$

And the number of retained electrons is

$$N_{\text{retained},1}(x, v) \;=\; n_0\tilde{f}_{e,0}(v)[1 - f_d(x, v)]\,dxdv. \tag{A.2}$$

With our algorithm, only the velocity of a rejected electron will be updated. The total number of rejected electrons at a position x that are subject to redistribution of velocity is $n_0dx\int \tilde{f}_{e,0}(v)f_d(x, v)\,dv$. So the number of electrons that are redistributed to the phase space area after another Step 2 is $n_0dx(\int \tilde{f}_{e,0}(v)f_d(x, v)\,dv)\tilde{f}_{e,0}(v)\,dv$. The number of

rejected and retained electrons at the second iteration in the same phase space area are

$$N_{\text{rejected},2}(x,v) = \left[\int \tilde{f}_{e,0}(v) f_d(x,v)\, dv\right] n_0 \tilde{f}_{e,0}(v) f_d(x,v)\, dxdv, \tag{A.3}$$

$$N_{\text{retained},2}(x,v) = \left[\int \tilde{f}_{e,0}(v) f_d(x,v)\, dv\right] n_0 \tilde{f}_{e,0}(v)[1 - f_d(x,v)]\, dxdv. \tag{A.4}$$

Compare these expressions at the second iteration to the ones from the first iteration. It is easy to see that n_0 is replaced by $[\int \tilde{f}_{e,0}(v) f_d(x,v)\, dv] n_0$ in the new expressions. As n_0 is arbitrary, this pattern can be generalized to any number of iterations by induction. The total number of retained electrons in that phase space area can be calculated as

$$\begin{aligned}
&N_{\text{retained,total}}(x,v) \\
&= n_0 \tilde{f}_{e,0}(v)[1 - f_d(x,v)]\, dxdv \left\{1 + \left[\int \tilde{f}_{e,0}(v) f_d(x,v)\, dv\right] + \left[\int \tilde{f}_{e,0}(v) f_d(x,v)\, dv\right]^2 + ...\right\} \\
&= n_0 \tilde{f}_{e,0}(v)[1 - f_d(x,v)]\, dxdv \frac{1}{1 - \int \tilde{f}_{e,0}(v) f_d(x,v)\, dv} \\
&= n_0 \frac{\tilde{f}_{e,0}(v) - \tilde{f}_{e,0}(v) f_d(x,v)}{1 - \int \tilde{f}_{e,0}(v) f_d(x,v)\, dv}\, dxdv.
\end{aligned} \tag{A.5}$$

Convergence of the geometric series is guaranteed as $\int \tilde{f}_{e,0}(v) f_d(x,v)\, dv < 1$.
In reality, we need only a few iterations to finish initialization. The total rejection number quickly converges to 0 as for the parameters ($\sigma_d \leq 0.15 v_{th,e}$, $h_d \leq 0.9$) we are using, we have $\int \tilde{f}_{e,0}(v) f_d(x,v)\, dv \sim 0.1$.

Appendix B

Rate of change of contained ion momentum

We calculate the rate of change of inertial-frame ion momentum contained in the control volume from x_a to x_b to the leading order in $t_{ab}\dot{U}/U$

$$\begin{aligned}\dot{P}_{ic} &= \frac{d}{dt}\left(\int_{x_a}^{x_b} m_i n\bar{v}\, dx\right) \\ &= m_i \int_{x_a}^{x_b} \frac{\partial n}{\partial t}(v + U_{\rm ref})\, dx + m_i \int_{x_a}^{x_b} n\frac{\partial (v + U_{\rm ref})}{\partial t}\, dx \\ &= m_i U_{\rm ref} \int_{x_a}^{x_b} \frac{\partial n}{\partial t}\, dx + m_i \int_{x_a}^{x_b} \frac{\partial n}{\partial t} v\, dx + m_i \int_{x_a}^{x_b} n\frac{\partial v}{\partial t}\, dx + m_i \dot{U}_{\rm ref} \int_{x_a}^{x_b} n\, dx. \end{aligned} \tag{B.1}$$

$U_{\rm ref}$ is the hole velocity in the reference frame. $U_{\rm ref}$ is the characteristic of the reference frame and does not depend on x. We have $\dot{U}_{\rm ref} = \dot{U}$. Choose the inertial frame such that $U_{\rm ref} = 0$ (the instantaneous hole rest frame). Then at $t = t_f$

$$\dot{P}_{ic} \;=\; m_i \int_{x_a}^{x_b} \frac{\partial (nv)}{\partial t}\, dx + m_i \dot{U} \int_{x_a}^{x_b} n\, dx. \tag{B.2}$$

We apply the continuity of an ion fluid element from x_a to a position x between x_a and x_b

$$n_{as_x} v_{as_x} \delta t_{as_x} \;=\; nv\delta t_{xf}, \tag{B.3}$$

where the subscript s_x refers to the time t_{s_x} for an ion particle at x when $t = t_f$ to first enter the control volume at x_a, so $t_{s_x} = t_f - \int_{x_a}^{x} \frac{du}{v}$. Using the constancy of the inflow density, we express nv as

$$nv \;=\; \frac{n_\infty v_{as_x} \delta t_{as_x}}{\delta t_{xf}}, \tag{B.4}$$

with

$$\frac{\delta t_{as_x}}{\delta t_{xf}} \;\simeq\; \frac{1}{1 + \left.\dfrac{\partial t_{ax}}{\partial t_{s_x}}\right|_x}. \tag{B.5}$$

$t_{ax} = \int_{x_a}^{x} \frac{dx_1}{v}$ is the ion transit time between x_a and x. The ion velocity is governed by the conservation of its first integral of motion

$$\frac{v^2(t(x_1, x))}{2} + \phi(x_1) = \frac{v^2(t_{s_x})}{2} - \int_{x_a}^{x_1} \dot{U}(t(x_2, x))\, dx_2. \tag{B.6}$$

We can then give an expression for $\frac{\partial t_{ax}}{\partial t_{s_x}}|_x$ to its leading order

$$\begin{aligned}
\left.\frac{\partial t_{ax}}{\partial t_{s_x}}\right|_x \;&=\; \frac{\partial}{\partial t_{s_x}} \left(\int_{x_a}^{x} \frac{dx_1}{v} \right) \\
&= \int_{x_a}^{x} \left.\frac{\partial}{\partial t_{s_x}}\right|_{x_1} \left(\frac{1}{v}\right) dx_1 \\
&= \int_{x_a}^{x} -\frac{1}{v^3} \left.\frac{\partial (v^2/2)}{\partial t_{s_x}}\right|_{x_1} dx_1 \\
&= \int_{x_a}^{x} \frac{1}{v^3} \left[v(t_{s_x}) \dot{U}(t_{s_x}) + \int_{x_a}^{x_1} \left.\frac{\partial \dot{U}}{\partial t_{s_x}}\right|_{x_2} dx_2 \right] dx_1 \\
&\simeq \int_{x_a}^{x} \frac{v(t_{s_x})}{v^3} \left[\dot{U}(t_{s_x}) + \frac{1}{v(t_{s_x})} \int_{x_a}^{x_1} \ddot{U}(t(x_2, x))\, dx_2 \right] dx_1.
\end{aligned} \tag{B.7}$$

We used interchangeably dt and dt_{sx} as $t(x_2, x) = t_f - \int_{x_2}^{x} \frac{du}{v}$ and $t(x) = t_{s_x} + \int_{x_a}^{x} \frac{dx_1}{v_0(x_1) + v_1(x_1, t_{s_x})}$ so that $dt = dt_{s_x}(1 + \mathcal{O}(t_{ab}\dot{U}/U))$ for x fixed. The first term of $\dot{P}_{ic}$ in Eq. (B.2) can be

expressed as

$$
\begin{aligned}
m_i \int_{x_a}^{x_b} \left.\frac{\partial(nv)}{\partial t}\right|_x dx &\simeq m_i \int_{x_a}^{x_b} \left.\frac{\partial(nv)}{\partial t_{s_x}}\right|_x dx \\
&= m_i \int_{x_a}^{x_b} \left.\frac{\partial}{\partial t_{s_x}}\right|_x \left(n_\infty v(t_{s_x}) \frac{\delta t_{as_x}}{\delta t_{xf}} \right) dx \\
&= \underbrace{-m_i n_\infty \int_{x_a}^{x_b} \dot{U}(t_{s_x}) \frac{\delta t_{as_x}}{\delta t_{xf}}\, dx}_{\mathbf{I}} + \underbrace{m_i n_\infty \int_{x_a}^{x_b} v(t_{s_x}) \left.\frac{\partial}{\partial t_{s_x}}\right|_x \left(\frac{\delta t_{as_x}}{\delta t_{xf}} \right) dx}_{\mathbf{II}}.
\end{aligned}
\tag{B.8}
$$

Combining Eqn. (B.7) and Eqn. (B.5), we have an expression for $\frac{\delta t_{as_x}}{\delta t_{xf}}$

$$
\begin{aligned}
\frac{\delta t_{as_x}}{\delta t_{xf}} &\simeq \frac{1}{1 + \int_{x_a}^{x} \frac{v(t_{s_x})}{v^3} \left[\dot{U}(t_{s_x}) + \frac{1}{v(t_{s_x})} \int_{x_a}^{x_1} \ddot{U}(t(x_2, x))\, dx_2 \right] dx_1} \\
&= 1 + \mathcal{O}\left(\frac{t_{ab} \dot{U}}{U} \right).
\end{aligned}
\tag{B.9}
$$

Therefore, to the lowest order, the term **I** in Eq. (B.8) is

$$
-m_i n_\infty \int_{x_a}^{x_b} \dot{U}(t_{s_x})\, dx. \tag{B.10}
$$

To calculate the term **II** in Eq. (B.8), we need

$$
\left.\frac{\partial}{\partial t_{s_x}}\right|_x \left(\frac{\delta t_{as_x}}{\delta t_{xf}} \right) = -\frac{1}{\left(1 + \left.\frac{\partial t_{ax}}{\partial t_{s_x}}\right|_x \right)^2} \left.\frac{\partial^2 t_{ax}}{\partial t_{s_x}^2}\right|_x. \tag{B.11}
$$

We use the results from Eq. (B.7) to get

$$
\begin{aligned}
\left.\frac{\partial^2 t_{ax}}{\partial t_{s_x}^2}\right|_x &= \int_{x_a}^{x} \frac{\partial}{\partial t_{s_x}} \left(-\frac{1}{v^3} \frac{\partial(v^2/2)}{\partial t_{s_x}} \right) dx_1 \\
&\simeq \int_{x_a}^{x} \frac{1}{v^3} \frac{\partial}{\partial t_{s_x}} \left(v(t_{s_x}) \dot{U}(t_{s_x}) + \int_{x_a}^{x_1} \ddot{U}(t(x_2, x))\, dx_2 \right) dx_1 \quad (1^{\text{st}} \text{ order}) \\
&\simeq \int_{x_a}^{x} \frac{v(t_{s_x})}{v^3} \left(\ddot{U}(t_{s_x}) + \frac{1}{v(t_{s_x})} \int_{x_a}^{x_1} \dddot{U}(t(x_2, x))\, dx_2 \right) dx_1.
\end{aligned}
\tag{B.12}
$$

Thus, the term **II** in Eq. (B.8) can be written as

$$-m_i n_\infty \int_{x_a}^{x_b} v^2(t_{s_x}) \int_{x_a}^{x} \frac{1}{v^3} \left(\ddot{U}(t_{s_x}) + \frac{1}{v(t_{s_x})} \int_{x_a}^{x_1} \dddot{U}(t(x_2, x))\, dx_2 \right) dx_1\, dx. \tag{B.13}$$

Combining everything above, we have to the leading order

$$\begin{aligned} \dot{P}_{ic} \;=\; & - m_i n_\infty \int_{x_a}^{x_b} \dot{U}(t_{s_x})\, dx - m_i n_\infty \dot{U}(t_f) \int_{x_a}^{x_b} \frac{U}{v}\, dx \\ & - m_i n_\infty \int_{x_a}^{x_b} v^2(t_{s_x}) \int_{x_a}^{x} \frac{1}{v^3} \left(\ddot{U}(t_{s_x}) + \frac{1}{v(t_{s_x})} \int_{x_a}^{x_1} \dddot{U}(t(x_2, x))\, dx_2 \right) dx_1\, dx. \end{aligned} \tag{B.14}$$

Now we apply integration by parts to the last term in Eq. (B.14) using $\frac{\partial t(x_2,x)}{\partial x_2}|_x = \frac{1}{v(t(x_2,x))}$

$$\begin{aligned} \ddot{U}(t_{s_x}) + \frac{1}{v(t_{s_x})} \int_{x_a}^{x_1} \dddot{U}(t(x_2, x))\, dx_2 \;&=\; \ddot{U}(t_f - \int_{x_a}^{x} \frac{du}{v}) + \frac{1}{v(t_{s_x})} \int_{x_a}^{x_1} \dddot{U}(t_f - \int_{x_2}^{x} \frac{du}{v}) \frac{1}{v} v\, dx_2 \\ &=\; \ddot{U}(t_{s_x}) + \frac{1}{v(t_{s_x})} \left(\left[v\ddot{U} \right]_{x_a}^{x_1} - \int_{x_a}^{x_1} \ddot{U} \frac{\dot{v}}{v}\, dx_2 \right) \\ &=\; \ddot{U}(t(x_1, x)) \frac{v}{v(t_{s_x})} - \frac{1}{v(t_{s_x})} \int_{x_a}^{x_1} \frac{\ddot{U}(t(x_2, x))\dot{v}}{v}\, dx_2 \end{aligned} \tag{B.15}$$

Plug this expression in Eq. (B.14) and remember that $v(t_{s_x}) \simeq -U$, we have

$$\begin{aligned} \dot{P}_{ic} \;=\; & - m_i n_\infty \int_{x_a}^{x_b} \dot{U}(t_{s_x})\, dx - m_i n_\infty \dot{U}(t_f) \int_{x_a}^{x_b} \frac{U}{v}\, dx - m_i n_\infty \int_{x_a}^{x_b} v(t_{s_x}) \int_{x_a}^{x} \frac{\ddot{U}(t(x_1, x))}{v^2}\, dx_1\, dx \\ & + m_i n_\infty \int_{x_a}^{x_b} v(t_{s_x}) \int_{x_a}^{x} \frac{1}{v^3} \int_{x_a}^{x_1} \frac{\ddot{U}(t(x_2, x))\dot{v}}{v}\, dx_2\, dx_1\, dx, \end{aligned} \tag{B.16}$$

where

$$\begin{aligned} \int_{x_a}^{x} \frac{\ddot{U}(t(x_1, x))}{v^2}\, dx_1 \;&=\; \left[\frac{1}{v} \dot{U}(t_f - \int_{x_1}^{x} \frac{du}{v}) \right]_{x_a}^{x} + \int_{x_a}^{x} \frac{\dot{U}(t(x_1, x))\dot{v}}{v^3}\, dx_1 \\ &=\; \frac{\dot{U}(t_f)}{v} - \frac{\dot{U}(t_{s_x})}{v(t_{s_x})} + \int_{x_a}^{x} \frac{\dot{U}(t(x_1, x))\dot{v}}{v^3}\, dx_1 \end{aligned} \tag{B.17}$$

and

$$\int_{x_a}^{x_1} \frac{\ddot{U}(t(x_2,x))\dot{v}}{v}\,dx_2 \;=\; \left[\dot{U}\dot{v}(t(x_2,x))\right]_{x_a}^{x_1} - \int_{x_a}^{x_1} \frac{\dot{U}\ddot{v}}{v}(t(x_2,x))\,dx_2$$
$$\simeq\; \dot{U}\dot{v}(t(x_1,x)) - \int_{x_a}^{x_1} \frac{\dot{U}\ddot{v}}{v}(t(x_2,x))\,dx_2 \;\; (1^{\text{st}} \text{ order}). \tag{B.18}$$

Simplify Eq. (B.16) by replacing the $\ddot{U}$ terms using Eqs. (B.17) (B.18). Most terms cancel out to the relevant order and we are left with only one leading order term

$$\dot{P}_{ic} \;=\; -\,m_i n_\infty \int_{x_a}^{x_b} v(t_{s_x}) \int_{x_a}^{x} \frac{1}{v^3} \int_{x_a}^{x_1} \frac{\dot{U}\ddot{v}}{v}(t(x_2,x))\,dx_2\,dx_1\,dx$$
$$\simeq\; -\,m_i n_\infty \int_{x_a}^{x_b} \int_{x_a}^{x} \frac{U}{v_0^3(x_1)} \int_{x_a}^{x_1} \dot{U}(t(x_2,x))\phi''(x_2)\,dx_2\,dx_1\,dx, \tag{B.19}$$

where we used the equation of motion for a single ion particle

$$\dot{v} + \phi' \;=\; -\dot{U}. \tag{B.20}$$

We combine $\dot{P}_{io}$ and $\dot{P}_{ic}$ to get $\dot{P}_i$

$$\dot{P}_i \;=\; \dot{P}_{io} + \dot{P}_{ic}. \tag{B.21}$$

Appendix C

Leading order expansion of $\dot{P}_i/\dot{P}_e$ in ψ/U^2

First order in ψ/U^2

The full expression of $\dot{P}_i$ is

$$\begin{aligned}\dot{P}_i =& n_\infty m_i \dot{U}\Bigg[\int_{x_a}^{x_b}\left(-1-2\frac{U}{v_0(x)}-\frac{U^2}{v_0^2(x)}\right)\exp\left(i\omega\int_x^{x_b}\frac{dx_3}{v_0(x_3)}\right)\,dx \\ &-\int_{x_a}^{x_b}\frac{U^2}{v_0^3(x)}\int_{x_a}^{x}\frac{\phi'(x_1)}{v_0(x_1)}\exp\left(i\omega\int_{x_1}^{x_b}\frac{dx_3}{v_0(x_3)}\right)\,dx_1\,dx \\ &-\int_{x_a}^{x_b}\int_{x_a}^{x}\frac{U}{v_0^3(x_1)}\int_{x_a}^{x_1}\exp\left(i\omega\int_{x_2}^{x}\frac{dx_3}{v_0(x_3)}\right)\phi''(x_2)\,dx_2\,dx_1\,dx\Bigg].\end{aligned} \tag{C.1}$$

We will begin by expanding the expression of $\dot{P}_i$ to the first order in ψ/U^2. Recall that the equilibrium ion velocity in the hole frame v_0 is

$$\begin{aligned}v_0(x) &= -\frac{U}{|U|}\sqrt{U^2-2\phi(x)} \\ &\simeq -U(1-\frac{\psi}{U^2}\tilde{\phi}(x))\end{aligned} \tag{C.2}$$

And the phase term inside the integral sign of Eqn. (C.1) is

$$\exp(i\omega\int_x^{x_b}\frac{dx_3}{v_0(x_3)}) \simeq \exp(i\frac{\omega(x-x_b)}{U})(1-\frac{i\omega}{U}\frac{\psi}{U^2}\int_x^{x_b}\tilde{\phi}(x_3)\,dx_3). \tag{C.3}$$

The term inside the first integral can be rewritten taking $v_0 \simeq -U$ as

$$-1 - 2\frac{U}{v_0(x)} - \frac{U^2}{v_0^2(x)} \;=\; -\left(\frac{U}{v_0(x)} + 1\right)^2 \;\simeq\; -\frac{\psi^2}{U^4}\tilde{\phi}(x)^2, \tag{C.4}$$

which is already a second order term. The only first order contributions come from the last two integrals. To the first order in ψ/U^2, $\dot{P}_i$ can be written as

$$\begin{aligned}\dot{P}_i \;\simeq n_\infty m_i \dot{U}\frac{\psi}{U^2}\Bigg[&- \int_{x_a}^{x_b}\int_{x_a}^{x} \tilde{\phi}'(x_1)\exp\left(i\frac{\omega}{U}(x_1 - x_b)\right)\, dx_1\, dx \\ &+ \int_{x_a}^{x_b}\int_{x_a}^{x}\int_{x_a}^{x_1} \tilde{\phi}''(x_2)\exp\left(i\frac{\omega}{U}(x_2 - x)\right)\, dx_2\, dx_1\, dx\Bigg].\end{aligned} \tag{C.5}$$

We first apply integration by parts to the triple integral term in Eqn. (C.5)

$$\begin{aligned}\int_{x_a}^{x_b}\int_{x_a}^{x}\int_{x_a}^{x_1} \tilde{\phi}''(x_2)\exp\left(i\frac{\omega}{U}(x_2 - x)\right)\, dx_2\, dx_1\, dx \;=\; &\int_{x_a}^{x_b}\int_{x_a}^{x} \tilde{\phi}'(x_1)\exp\left(i\frac{\omega}{U}(x_1 - x)\right)\, dx_1\, dx \\ - \int_{x_a}^{x_b}\int_{x_a}^{x}\int_{x_a}^{x_1} &\tilde{\phi}'(x_2)\exp\left(i\frac{\omega}{U}(x_2 - x)\right)\left(\frac{i\omega}{U}\right)\, dx_2\, dx_1\, dx.\end{aligned} \tag{C.6}$$

We interchange the order of integration to integrate the triple integral. The integration domain of this triple integral is

$$\mathcal{D} \;=\; \left\{(x, x_1, x_2) \in \mathbb{R}^3 | x_a \le x_2 \le x_1 \le x \le x_b\right\}. \tag{C.7}$$

We define an indicator function $\mathbb{1}_{\mathcal{D}}$ associated with this measurable subset of $\mathbb{R}^3$ and we have

$$\begin{aligned}
&\int_{x_a}^{x_b}\int_{x_a}^{x}\int_{x_a}^{x_1}\tilde{\phi}'(x_2)\exp\left(i\frac{\omega}{U}(x_2-x)\right)\left(\frac{i\omega}{U}\right)\,dx_2\,dx_1\,dx\\
&=\int_{x_a}^{x_b}\int_{x_a}^{x_b}\int_{x_a}^{x_b}\tilde{\phi}'(x_2)\exp\left(i\frac{\omega}{U}(x_2-x)\right)\left(\frac{i\omega}{U}\right)\mathbb{1}_{\mathcal{D}}\,dx_2\,dx_1\,dx\\
&=\int_{x_a}^{x_b}\int_{x_a}^{x_b}\int_{x_a}^{x_b}\tilde{\phi}'(x_2)\exp\left(i\frac{\omega}{U}(x_2-x)\right)\left(\frac{i\omega}{U}\right)\mathbb{1}_{\mathcal{D}}\,dx\,dx_2\,dx_1\ \text{(Interchange integration order)}\\
&=\int_{x_a}^{x_b}\int_{x_a}^{x_1}\left[\tilde{\phi}'(x_2)\exp\left(i\frac{\omega}{U}(x_2-x)\right)\left(\frac{i\omega}{U}\right)\left(\frac{U}{-i\omega}\right)\right]_{x=x_1}^{x=x_b}dx_2\,dx_1\\
&=\int_{x_a}^{x_b}\int_{x_a}^{x_1}\tilde{\phi}'(x_2)\exp\left(i\frac{\omega}{U}(x_2-x_1)\right)\,dx_2\,dx_1-\int_{x_a}^{x_b}\int_{x_a}^{x_1}\tilde{\phi}'(x_2)\exp\left(i\frac{\omega}{U}(x_2-x_b)\right)\,dx_2\,dx_1.
\end{aligned}\tag{C.8}$$

Interchanging the order of integration is the mathematical technique we use throughout this derivation to deal with multiple integrals. Since the first term in Eqn. (C.8) cancels the first term in Eqn. (C.6) and

$$\int_{x_a}^{x_b}\int_{x_a}^{x}\int_{x_a}^{x_1}\tilde{\phi}''(x_2)\exp\left(i\frac{\omega}{U}(x_2-x)\right)\,dx_2\,dx_1\,dx\;=\;\int_{x_a}^{x_b}\int_{x_a}^{x_1}\tilde{\phi}'(x_2)\exp\left(i\frac{\omega}{U}(x_2-x_b)\right)\,dx_2\,dx_1.\tag{C.9}$$

Using this result in Eqn. (C.5) and we get the exact cancellation of the two first-order terms. Therefore, we need to push the expansion to the next order, which is ψ^2/U^4.

Second order in ψ/U^2

First, we identify all the terms that are of order ψ^2/U^4 in the expansion of $\dot{P}_i$. We examine each term in Eqn. (C.1). We have for the first term

$$\begin{aligned}
&\int_{x_a}^{x_b}\left(-1-2\frac{U}{v_0(x)}-\frac{U^2}{v_0^2(x)}\right)\exp\left(i\omega\int_x^{x_b}\frac{dx_3}{v_0(x_3)}\right)\,dx\\
&=\int_{x_a}^{x_b}-\left(1+\frac{U}{v_0(x)}\right)^2\exp\left(i\omega\int_x^{x_b}\frac{dx_3}{v_0(x_3)}\right)\,dx\\
&\simeq-\frac{\psi^2}{U^4}\int_{x_a}^{x_b}\tilde{\phi}(x)^2\exp\left(i\frac{\omega}{U}(x-x_b)\right)\,dx.
\end{aligned}\tag{C.10}$$

The second term will give contributions both from v_0 and the phase term

$$\begin{aligned}
&-\int_{x_a}^{x_b}\frac{U^2}{v_0^3(x)}\int_{x_a}^{x}\frac{\phi'(x_1)}{v_0(x_1)}\exp\left(i\omega\int_{x_1}^{x_b}\frac{dx_3}{v_0(x_3)}\right)\,dx_1\,dx\\
\simeq&-\frac{\psi}{U^2}\int_{x_a}^{x_b}\int_{x_a}^{x}\tilde{\phi}'(x_1)\exp\left(i\frac{\omega}{U}(x_1-x_b)\right)\,dx_1\,dx\ \ \text{(First order)}\\
&+\frac{\psi^2}{U^4}\Bigg\{-\int_{x_a}^{x_b}\int_{x_a}^{x}\left(3\tilde{\phi}(x)\tilde{\phi}'(x_1)+\tilde{\phi}'(x_1)\tilde{\phi}(x_1)\right)\exp\left(i\frac{\omega}{U}(x_1-x_b)\right)\,dx_1\,dx\\
&\qquad+\int_{x_a}^{x_b}\int_{x_a}^{x}\int_{x_1}^{x_b}\tilde{\phi}(x_3)\tilde{\phi}'(x_1)\exp\left(i\frac{\omega}{U}(x_1-x_b)\right)\left(\frac{i\omega}{U}\right)\,dx_3\,dx_1\,dx\Bigg\}.
\end{aligned}\tag{C.11}$$

The third term can be expanded as

$$\begin{aligned}
&-\int_{x_a}^{x_b}\int_{x_a}^{x}\frac{U}{v_0^3(x_1)}\int_{x_a}^{x_1}\exp\left(i\omega\int_{x_2}^{x}\frac{dx_3}{v_0(x_3)}\right)\phi''(x_2)\,dx_2\,dx_1\,dx\\
\simeq&\frac{\psi}{U^2}\int_{x_a}^{x_b}\int_{x_a}^{x}\int_{x_a}^{x_1}\tilde{\phi}''(x_2)\exp\left(i\frac{\omega}{U}(x_2-x)\right)\,dx_2\,dx_1\,dx\ \ \text{(First order)}\\
&+\frac{\psi^2}{U^4}\Bigg\{\int_{x_a}^{x_b}\int_{x_a}^{x}\int_{x_a}^{x_1}3\tilde{\phi}(x_1)\tilde{\phi}''(x_2)\exp\left(i\frac{\omega}{U}(x_2-x)\right)\,dx_2\,dx_1\,dx\\
&\qquad+\int_{x_a}^{x_b}\int_{x_a}^{x}\int_{x_a}^{x_1}\int_{x_2}^{x}\tilde{\phi}''(x_2)\tilde{\phi}(x_3)\exp\left(i\frac{\omega}{U}(x_2-x)\right)\left(-i\frac{\omega}{U}\right)\,dx_3\,dx_2\,dx_1\,dx\Bigg\}.
\end{aligned}\tag{C.12}$$

We will deal with these integrals one by one, starting from the simpler double integrals and moving our way to the quadruple integral. The idea is to use integration by parts and interchanging the order of integration to simplify them as much as possible as we showed previously. In the end, we should have simpler integral expressions involving only $\tilde{\phi}$ and not its derivatives. Let's start with the double integral that is multiplying the second

order term in Eqn. (C.11).

$$
\begin{aligned}
&- \int_{x_a}^{x_b}\int_{x_a}^{x} \left(3\tilde{\phi}(x)\tilde{\phi}'(x_1) + \tilde{\phi}'(x_1)\tilde{\phi}(x_1)\right) \exp\left(i\frac{\omega}{U}(x_1 - x_b)\right)\, dx_1\, dx \\
&= - \int_{x_a}^{x_b}\int_{x_a}^{x} 3\tilde{\phi}(x) \exp\left(i\frac{\omega}{U}(x_1 - x_b)\right)\, d\tilde{\phi}(x_1)\, dx - \int_{x_a}^{x_b}\int_{x_a}^{x} \exp\left(i\frac{\omega}{U}(x_1 - x_b)\right)\, d(\tilde{\phi}(x_1)^2/2)\, dx \\
&= -\frac{7}{2}\int_{x_a}^{x_b} \tilde{\phi}(x)^2 \exp\left(i\frac{\omega}{U}(x - x_b)\right)\, dx + 3\left(\frac{i\omega}{U}\right)\int_{x_a}^{x_b}\int_{x_a}^{x} \tilde{\phi}(x)\tilde{\phi}(x_1) \exp\left(i\frac{\omega}{U}(x_1 - x_b)\right)\, dx_1\, dx \\
&\qquad + \left(\frac{i\omega}{U}\right)\int_{x_a}^{x_b}\int_{x_a}^{x} \frac{\tilde{\phi}(x_1)^2}{2} \exp\left(i\frac{\omega}{U}(x_1 - x_b)\right)\, dx_1\, dx \\
&= -\frac{7}{2}\int_{x_a}^{x_b} \tilde{\phi}(x)^2 \exp\left(i\frac{\omega}{U}(x - x_b)\right)\, dx + 3\left(\frac{i\omega}{U}\right)\int_{x_a}^{x_b}\int_{x_a}^{x} \tilde{\phi}(x)\tilde{\phi}(x_1) \exp\left(i\frac{\omega}{U}(x_1 - x_b)\right)\, dx_1\, dx \\
&\qquad + \frac{1}{2}\left(\frac{i\omega}{U}\right)\int_{x_a}^{x_b}\int_{x_1}^{x_b} \tilde{\phi}(x_1)^2 \exp\left(i\frac{\omega}{U}(x_1 - x_b)\right)\, dx\, dx_1 \\
&= -\frac{7}{2}\int_{x_a}^{x_b} \tilde{\phi}(x)^2 \exp\left(i\frac{\omega}{U}(x - x_b)\right)\, dx + 3\left(\frac{i\omega}{U}\right)\int_{x_a}^{x_b}\int_{x_a}^{x} \tilde{\phi}(x)\tilde{\phi}(x_1) \exp\left(i\frac{\omega}{U}(x_1 - x_b)\right)\, dx_1\, dx \\
&\qquad + \frac{1}{2}\left(\frac{i\omega}{U}\right)\int_{x_a}^{x_b} \tilde{\phi}(x_1)^2 \exp\left(i\frac{\omega}{U}(x_1 - x_b)\right)(x_b - x_1)\, dx_1.
\end{aligned}
\tag{C.13}
$$

The triple integral in Eqn. (C.11) is

$$
\begin{aligned}
&\int_{x_a}^{x_b}\int_{x_a}^{x}\int_{x_1}^{x_b} \tilde{\phi}(x_3)\tilde{\phi}'(x_1) \exp\left(i\frac{\omega}{U}(x_1 - x_b)\right)\left(\frac{i\omega}{U}\right)\, dx_3\, dx_1\, dx \\
&= \int_{x_a}^{x_b}\int_{x_a}^{x_3}\int_{x_1}^{x_b} \tilde{\phi}(x_3)\tilde{\phi}'(x_1) \exp\left(i\frac{\omega}{U}(x_1 - x_b)\right)\left(\frac{i\omega}{U}\right)\, dx\, dx_1\, dx_3 \\
&= \int_{x_a}^{x_b}\int_{x_a}^{x_3} \tilde{\phi}(x_3) \exp\left(i\frac{\omega}{U}(x_1 - x_b)\right)(x_b - x_1)\left(\frac{i\omega}{U}\right)\, d\phi(x_1)\, dx_3 \\
&= \left(\frac{i\omega}{U}\right)\int_{x_a}^{x_b} \tilde{\phi}(x_3)^2(x_b - x_3) \exp\left(i\frac{\omega}{U}(x_3 - x_b)\right)\, dx_3 \\
&\qquad + \left(\frac{i\omega}{U}\right)\int_{x_a}^{x_b}\int_{x_a}^{x_3} \tilde{\phi}(x_3)\tilde{\phi}(x_1) \exp\left(i\frac{\omega}{U}(x_1 - x_b)\right)\, dx_1\, dx_3 \\
&\qquad - \left(\frac{i\omega}{U}\right)^2\int_{x_a}^{x_b}\int_{x_a}^{x_3} \tilde{\phi}(x_3)\tilde{\phi}(x_1)(x_b - x_1) \exp\left(i\frac{\omega}{U}(x_1 - x_b)\right)\, dx_1\, dx_3.
\end{aligned}
\tag{C.14}
$$

Now we simplify the triple integral in Eqn. (C.12) using twice integration by parts and interchanging the order of integration

$$
\begin{aligned}
&\int_{x_a}^{x_b}\int_{x_a}^{x}\int_{x_a}^{x_1} 3\tilde{\phi}(x_1)\tilde{\phi}''(x_2)\exp\left(i\frac{\omega}{U}(x_2-x)\right)\,dx_2\,dx_1\,dx \\
=&\,3\int_{x_a}^{x_b}\int_{x_a}^{x}\tilde{\phi}(x_1)\tilde{\phi}'(x_1)\exp\left(i\frac{\omega}{U}(x_1-x)\right)\,dx_1\,dx \\
&\qquad -3\int_{x_a}^{x_b}\int_{x_a}^{x}\int_{x_a}^{x_1}\tilde{\phi}(x_1)\tilde{\phi}'(x_2)\exp\left(i\frac{\omega}{U}(x_2-x)\right)\left(\frac{i\omega}{U}\right)\,dx_2\,dx_1\,dx \\
=&\,\frac{3}{2}\int_{x_a}^{x_b}\tilde{\phi}(x)^2\,dx-\frac{9}{2}\int_{x_a}^{x_b}\int_{x_a}^{x}\tilde{\phi}(x_1)^2\exp\left(i\frac{\omega}{U}(x_1-x)\right)\left(\frac{i\omega}{U}\right)\,dx_1\,dx \\
&\qquad +3\int_{x_a}^{x_b}\int_{x_a}^{x_1}\int_{x_1}^{x_b}\tilde{\phi}(x_1)\tilde{\phi}(x_2)\exp\left(i\frac{\omega}{U}(x_2-x)\right)\left(\frac{i\omega}{U}\right)^2\,dx\,dx_2\,dx_1 \\
=&\,\frac{3}{2}\int_{x_a}^{x_b}\tilde{\phi}(x)^2\,dx-\frac{9}{2}\left(\frac{i\omega}{U}\right)\int_{x_a}^{x_b}\left[\tilde{\phi}(x_1)^2\exp\left(i\frac{\omega}{U}(x_1-x)\right)\left(\frac{-U}{i\omega}\right)\right]_{x=x_1}^{x=x_b}dx_1 \qquad \text{(C.15)} \\
&\qquad -3\left(\frac{i\omega}{U}\right)\int_{x_a}^{x_b}\int_{x_a}^{x_1}\tilde{\phi}(x_1)\tilde{\phi}(x_2)\exp\left(i\frac{\omega}{U}(x_2-x_b)\right)\,dx_2\,dx_1 \\
&\qquad +3\left(\frac{i\omega}{U}\right)\int_{x_a}^{x_b}\int_{x_a}^{x_1}\tilde{\phi}(x_1)\tilde{\phi}(x_2)\exp\left(i\frac{\omega}{U}(x_2-x_1)\right)\,dx_2\,dx_1 \\
=&\,-3\int_{x_a}^{x_b}\tilde{\phi}(x)^2\,dx+\frac{9}{2}\int_{x_a}^{x_b}\tilde{\phi}(x_1)^2\exp\left(i\frac{\omega}{U}(x_1-x_b)\right)\,dx_1 \\
&\qquad -3\left(\frac{i\omega}{U}\right)\int_{x_a}^{x_b}\int_{x_a}^{x_1}\tilde{\phi}(x_1)\tilde{\phi}(x_2)\exp\left(i\frac{\omega}{U}(x_2-x_b)\right)\,dx_2\,dx_1 \\
&\qquad +3\left(\frac{i\omega}{U}\right)\int_{x_a}^{x_b}\int_{x_a}^{x_1}\tilde{\phi}(x_1)\tilde{\phi}(x_2)\exp\left(i\frac{\omega}{U}(x_2-x_1)\right)\,dx_2\,dx_1.
\end{aligned}
$$

Now we deal with the only term left, which is the quadruple integral in the Eqn. (C.12). We will try to relate it to the integrals we've already calculated. Observing the integrand, we notice that it is easy to integrate with respect to the variable x_1. We interchange the order of integration as we did before

$$
\begin{aligned}
&\int_{x_a}^{x_b}\int_{x_a}^{x}\int_{x_a}^{x_1}\int_{x_2}^{x}\tilde{\phi}''(x_2)\tilde{\phi}(x_3)\exp\left(i\frac{\omega}{U}(x_2-x)\right)\left(-i\frac{\omega}{U}\right)\,dx_3\,dx_2\,dx_1\,dx \\
=&\int_{x_a}^{x_b}\int_{x_a}^{x}\int_{x_2}^{x}\int_{x_2}^{x}\tilde{\phi}''(x_2)\tilde{\phi}(x_3)\exp\left(i\frac{\omega}{U}(x_2-x)\right)\left(-i\frac{\omega}{U}\right)\,dx_1\,dx_3\,dx_2\,dx \qquad \text{(C.16)} \\
=&\int_{x_a}^{x_b}\int_{x_a}^{x}\int_{x_2}^{x}\tilde{\phi}''(x_2)\tilde{\phi}(x_3)\exp\left(i\frac{\omega}{U}(x_2-x)\right)\left(\frac{i\omega}{U}\right)(x_2-x)\,dx_3\,dx_2\,dx.
\end{aligned}
$$

Notice that the above integral can be expressed with the derivative w.r.t. $(i\omega/U)$ of another integral that we've calculated previously in the beginning of Eqn. (C.15)

$$\begin{aligned}
&\int_{x_a}^{x_b}\int_{x_a}^{x}\int_{x_2}^{x}\tilde{\phi}''(x_2)\tilde{\phi}(x_3)\exp\left(i\frac{\omega}{U}(x_2-x)\right)\left(\frac{i\omega}{U}\right)(x_2-x)\,dx_3\,dx_2\,dx \\
&=\left(\frac{i\omega}{U}\right)\frac{d}{d\,(i\omega/U)}\left[\int_{x_a}^{x_b}\int_{x_a}^{x}\int_{x_2}^{x}\tilde{\phi}''(x_2)\tilde{\phi}(x_3)\exp\left(i\frac{\omega}{U}(x_2-x)\right)\,dx_3\,dx_2\,dx\right] \\
&=\left(\frac{i\omega}{U}\right)\frac{d}{d\,(i\omega/U)}\left[\int_{x_a}^{x_b}\int_{x_a}^{x}\int_{x_a}^{x_3}\tilde{\phi}''(x_2)\tilde{\phi}(x_3)\exp\left(i\frac{\omega}{U}(x_2-x)\right)\,dx_2\,dx_3\,dx\right].
\end{aligned} \tag{C.17}$$

Therefore, the quadruple integral can be simplified using the final result of Eqn. (C.15)

$$\begin{aligned}
&\int_{x_a}^{x_b}\int_{x_a}^{x}\int_{x_a}^{x_1}\int_{x_2}^{x}\tilde{\phi}''(x_2)\tilde{\phi}(x_3)\exp\left(i\frac{\omega}{U}(x_2-x)\right)\left(-i\frac{\omega}{U}\right)\,dx_3\,dx_2\,dx_1\,dx \\
&=\left(\frac{i\omega}{U}\right)\frac{d}{d\,(i\omega/U)}\left[\int_{x_a}^{x_b}\int_{x_a}^{x}\int_{x_a}^{x_3}\tilde{\phi}''(x_2)\tilde{\phi}(x_3)\exp\left(i\frac{\omega}{U}(x_2-x)\right)\,dx_2\,dx_3\,dx\right] \\
&=\left(\frac{i\omega}{U}\right)\frac{d}{d\,(i\omega/U)}\Bigg[-\int_{x_a}^{x_b}\tilde{\phi}(x)^2\,dx+\frac{3}{2}\int_{x_a}^{x_b}\tilde{\phi}(x_1)^2\exp\left(i\frac{\omega}{U}(x_1-x_b)\right)\,dx_1 \\
&\qquad-\left(\frac{i\omega}{U}\right)\int_{x_a}^{x_b}\int_{x_a}^{x_1}\tilde{\phi}(x_1)\tilde{\phi}(x_2)\exp\left(i\frac{\omega}{U}(x_2-x_b)\right)\,dx_2\,dx_1 \\
&\qquad+\left(\frac{i\omega}{U}\right)\int_{x_a}^{x_b}\int_{x_a}^{x_1}\tilde{\phi}(x_1)\tilde{\phi}(x_2)\exp\left(i\frac{\omega}{U}(x_2-x_1)\right)\,dx_2\,dx_1\Bigg] \\
&=\frac{3}{2}\left(\frac{i\omega}{U}\right)\int_{x_a}^{x_b}\tilde{\phi}(x_1)^2\exp\left(i\frac{\omega}{U}(x_1-x_b)\right)(x_1-x_b)\,dx_1 \\
&\qquad-\left(\frac{i\omega}{U}\right)\int_{x_a}^{x_b}\int_{x_a}^{x_1}\tilde{\phi}(x_1)\tilde{\phi}(x_2)\exp\left(i\frac{\omega}{U}(x_2-x_b)\right)\,dx_2\,dx_1 \\
&\qquad-\left(\frac{i\omega}{U}\right)^2\int_{x_a}^{x_b}\int_{x_a}^{x_1}\tilde{\phi}(x_1)\tilde{\phi}(x_2)\exp\left(i\frac{\omega}{U}(x_2-x_b)\right)(x_2-x_b)\,dx_2\,dx_1 \\
&\qquad+\left(\frac{i\omega}{U}\right)\int_{x_a}^{x_b}\int_{x_a}^{x_1}\tilde{\phi}(x_1)\tilde{\phi}(x_2)\exp\left(i\frac{\omega}{U}(x_2-x_1)\right)\,dx_2\,dx_1 \\
&\qquad+\left(\frac{i\omega}{U}\right)^2\int_{x_a}^{x_b}\int_{x_a}^{x_1}\tilde{\phi}(x_1)\tilde{\phi}(x_2)\exp\left(i\frac{\omega}{U}(x_2-x_1)\right)(x_2-x_1)\,dx_2\,dx_1.
\end{aligned} \tag{C.18}$$

Now we add up all the second order contributions using Eqns. (C.10) (C.13) (C.14) (C.15) (C.18). The majority of terms cancel out and we are left with

$$\begin{aligned}\dot{P}_i \simeq n_\infty m_i \dot{U} \frac{\psi^2}{U^4} \Bigg[&- 3 \int_{x_a}^{x_b} \tilde{\phi}(x)^2 \, dx + 4 \left(\frac{i\omega}{U} \right) \int_{x_a}^{x_b} \int_{x_a}^{x_1} \tilde{\phi}(x_1) \tilde{\phi}(x_2) \exp\left(i \frac{\omega}{U} (x_2 - x_1) \right) \, dx_2 \, dx_1 \\ &+ \left(\frac{i\omega}{U} \right)^2 \int_{x_a}^{x_b} \int_{x_a}^{x_1} \tilde{\phi}(x_1) \tilde{\phi}(x_2) \exp\left(i \frac{\omega}{U} (x_2 - x_1) \right) (x_2 - x_1) \, dx_2 \, dx_1 \Bigg].\end{aligned} \tag{C.19}$$

The expansion of $\dot{P}_e$ in ψ/U^2 is trivial

$$\begin{aligned}\dot{P}_e &= -m_e \dot{U} n_\infty \int_{x_a}^{x_b} h(\sqrt{\phi(x)}) + 1 - \frac{|U|}{\sqrt{U^2 - 2\phi(x)}} \, dx \\ &\simeq -m_e \dot{U} n_\infty \int_{x_a}^{x_b} h(\sqrt{\phi(x)}) - \frac{\psi}{U^2} \tilde{\phi}(x) \, dx.\end{aligned} \tag{C.20}$$

We introduce the constant I_0 and a new function I

$$I_0 = \int_{x_a}^{x_b} \tilde{\phi}(x)^2 \, dx, \tag{C.21}$$

$$I(\frac{\omega}{U}) = \int_{x_a}^{x_b} \int_{x_a}^{y} \tilde{\phi}(x) \tilde{\phi}(y) \exp(i \frac{\omega(x-y)}{U}) \, dx \, dy. \tag{C.22}$$

We thus get the final leading order expansion of $\dot{P}_i/\dot{P}_e$ as it appears in Eqn. (4.21)

$$\frac{\dot{P}_i}{\dot{P}_e}(\omega, U, \phi) \simeq -\frac{m_i}{m_e} \frac{\psi^2}{U^4} \frac{4i\frac{\omega}{U} I(\frac{\omega}{U}) + i\frac{\omega^2}{U^2} I'(\frac{\omega}{U}) - 3I_0}{\int_{x_a}^{x_b} h(\sqrt{\phi(x)}) - \frac{\phi(x)}{U^2} \, dx}. \tag{C.23}$$

Bibliography

[1] May-Britt Kallenrode. *Space physics: an introduction to plasmas and particles in the heliosphere and magnetospheres*. Springer Science, 2013.

[2] Christophe Cardinaud, Marie-Claude Peignon, and Pierre-Yves Tessier. Plasma etching: principles, mechanisms, application to micro-and nano-technologies. *Applied Surface Science*, 164(1):72–83, 2000.

[3] J Richard Hall, Carolyn AL Westerdahl, Andrew T Devine, and Michael J Bodnar. Activated gas plasma surface treatment of polymers for adhesive bonding. *Journal of Applied Polymer Science*, 13(10):2085–2096, 1969.

[4] Jen-Shih Chang. Recent development of plasma pollution control technology: a critical review. *Science and Technology of Advanced Materials*, 2(3):571–576, 2001.

[5] Edgar Y Choueiri. New dawn for electric rockets. *Scientific American*, 300(2):58–65, 2009.

[6] Allen Caldwell, Konstantin Lotov, Alexander Pukhov, and Frank Simon. Proton-driven plasma-wakefield acceleration. *Nature Physics*, 5(5):363–367, 2009.

[7] Jeffrey P Freidberg. *Plasma physics and fusion energy*. Cambridge university press, 2008.

[8] Walter Schimmerling. The space radiation environment: An introduction. *The Health Risks of Extraterrestrial Environments*, 2011.

[9] Michael C Kelley. *The Earth's ionosphere: plasma physics and electrodynamics*, volume 96. Academic press, 2009.

[10] Louis J Lanzerotti. Space weather effects on technologies. *Space Weather*, pages 11–22, 2001.

[11] Donald A Gurnett and Amitava Bhattacharjee. *Introduction to plasma physics*. Cambridge University Press, 2005.

[12] Nicholas A. Krall and Alvin W. Trivelpiece. *Principles of plasma physics*. McGraw-Hill, 1973.

[13] Mehran Kardar. *Statistical physics of particles*. Cambridge University Press, 2007.

[14] Gerhard Rein. Non-linear stability for the Vlasov–Poisson system—the energy-Casimir method. *Mathematical methods in the applied sciences*, 17(14):1129–1140, 1994.

[15] Lev Davidovich Landau. On the vibrations of the electronic plasma. *Zh. Eksp. Teor. Fiz.*, 10:25, 1946.

[16] John Dawson. On Landau Damping. *The Physics of Fluids*, 4(7):869–874, 1961.

[17] JH Malmberg and CB Wharton. Collisionless damping of electrostatic plasma waves. *Physical Review Letters*, 13(6):184, 1964.

[18] RW Gould, TM O'Neil, and JH Malmberg. Plasma wave echo. *Physical Review Letters*, 19(5):219, 1967.

[19] Clément Mouhot and Cédric Villani. On Landau damping. *Acta mathematica*, 207(1):29–201, 2011.

[20] Jeffrey P Freidberg. *Ideal Magnetohydrodynamics*. Plenum Press, New York, NY, 1987.

[21] Chio-Zong Cheng and Georg Knorr. The integration of the Vlasov equation in configuration space. *Journal of Computational Physics*, 22(3):330–351, 1976.

[22] Gilbert Strang. On the construction and comparison of difference schemes. *SIAM Journal on Numerical Analysis*, 5(3):506–517, 1968.

[23] AJ Klimas and WM Farrell. Splitting algorithm for Vlasov simulation with filamentation filtration. *Journal of computational physics*, 110(1):150–163, 1994.

[24] C K Birdsall and A B Langdon. *Plasma Physics via Computer Simulation*. IOP Publishing, Bristol, 1991.

[25] I.B. Bernstein, J.M. Greene, and M.D. Kruskal. Exact Nonlinear Plasma Oscillations. *Physical Review*, 108(4), 1957.

[26] Hans Schamel. Electrostatic Phase Space Structures in Theory and Experiment. *Physics Reports*, 3(3):161–191, 1986.

[27] Giovanni Manfredi. Long-time behavior of nonlinear Landau damping. *Physical Review Letters*, 79(15):2815, 1997.

[28] William Bertsche, J Fajans, and L Friedland. Direct excitation of high-amplitude chirped bucket-BGK modes. *Physical Review Letters*, 91(26):265003, 2003.

[29] I. H. Hutchinson. Electron holes in phase space: What they are and why they matter. *Physics of Plasmas*, 24(5):055601, 2017.

[30] R. E. Ergun, C. W. Carlson, J. P. McFadden, F. S. Mozer, L. Muschietti, I. Roth, and R. J. Strangeway. Debye-Scale Plasma Structures Associated with Magnetic-Field-Aligned Electric Fields. *Physical Review Letters*, 81(4):826–829, 1998.

[31] J Pickett, L Chen, S Kahler, O Santolík, D Gurnett, B Tsurutani, and A Balogh. Isolated electrostatic structures observed throughout the Cluster orbit: relationship to magnetic field strength. *Ann. Geophys.*, 22:2515–2523, 2004.

[32] David M. Malaspina, David L. Newman, Lynn B. Willson, Keith Goetz, Paul J. Kellogg, and Kris Kerstin. Electrostatic solitary waves in the solar wind: Evidence for instability at solar wind current sheets. *Journal of Geophysical Research: Space Physics*, 118(2):591–599, 2013.

[33] J. F. Drake, M. Swisdak, C. Cattell, M. A. Shay, B. N. Rogers, and A. Zeiler. Formation of electron holes and particle energization during magnetic reconnection. *Science*, 299(1987):873–877, 2003.

[34] F S Mozer, O A Agapitov, A Artemyev, J L Burch, R E Ergun, B L Giles, D Mourenas, R B Torbert, T D Phan, and I Vasko. Magnetospheric Multiscale Satellite Observations of Parallel Electron Acceleration in Magnetic Field Reconnection by Fermi Reflection from Time Domain Structures. *Physical Review Letters*, 116(April):145101, 2016.

[35] L. B. Wilson, C. A. Cattell, P. J. Kellogg, K. Goetz, K. Kersten, J. C. Kasper, A. Szabo, and M. Wilber. Large-amplitude electrostatic waves observed at a supercritical interplanetary shock. *Journal of Geophysical Research: Space Physics*, 115(12):1–14, 2010.

[36] W Fox, M Porkolab, J Egedal, N Katz, and A Le. Laboratory Observation of Electron Phase-Space Holes during Magnetic Reconnection. *Physical Review Letters*, 255003(December):1–4, 2008.

[37] Bertrand Lefebvre, Li-jen Chen, Walter Gekelman, Paul Kintner, Jolene Pickett, Patrick Pribyl, Stephen Vincena, Franklin Chiang, and Jack Judy. Laboratory Measurements of Electrostatic Solitary Structures Generated by Beam Injection. *Physical Review Letters*, 115001(September):1–4, 2010.

[38] George B Arfken and Hans J Weber. *Mathematical methods for physicists*. Academic press, 4th edition, 1995.

[39] RZ Sagdeev. Cooperative phenomena and shock waves in collisionless plasmas. *Rev plasma phys*, 4:23, 1966.

[40] H Schamel. Stationary solitary, snoidal and sinusoidal ion acoustic waves. *Plasma Physics*, 14:905–924, 1972.

[41] W. Fox, M. Porkolab, J. Egedal, N. Katz, and A. Le. Observations of electron phase-space holes driven during magnetic reconnection in a laboratory plasma. *Physics of Plasmas*, 19(3), 2012.

[42] FL Scarf, LA Frank, KL Ackerson, and RP Lepping. Plasma wave turbulence at distant crossings of the plasma sheet boundaries and the neutral sheet. *Geophysical Research Letters*, 1(5):189–192, 1974.

[43] JW Bonnell, FS Mozer, GT Delory, AJ Hull, RE Ergun, CM Cully, V Angelopoulos, and PR Harvey. The Electric Field Instrument (EFI) for THEMIS. *Space Science Reviews*, pages 303–341, 2008.

[44] Cecilia Norgren, Mats André, Andris Vaivads, and Yuri V Khotyaintsev. Slow electron phase space holes: Magnetotail observations. *Geophysical Research Letters*, 42(6):1654–1661, 2015.

[45] Martin V. Goldman, David L. Newman, and André Mangeney. Theory of weak bipolar fields and electron holes with applications to space plasmas. *Physical Review Letters*, 99(14):2–5, 2007.

[46] C Cattell, J Dombeck, J Wygant, JF Drake, M Swisdak, ML Goldstein, W Keith, A Fazakerley, M André, E Lucek, et al. Cluster observations of electron holes in association with magnetotail reconnection and comparison to simulations. *Journal of Geophysical Research: Space Physics*, 110(A1), 2005.

[47] H Matsumoto, XH Deng, H Kojima, and RR Anderson. Observation of electrostatic solitary waves associated with reconnection on the dayside magnetopause boundary. *Geophysical Research Letters*, 30(6), 2003.

[48] SD Bale, PJ Kellogg, DE Larsen, RP Lin, K Goetz, and RP Lepping. Bipolar

electrostatic structures in the shock transition region: Evidence of electron phase space holes. *Geophysical Research Letters*, 25(15):2929–2932, 1998.

[49] Shiyou Li, Shifeng Zhang, Hong Cai, and Sufang Yu. Concentration of electrostatic solitary waves around magnetic nulls within magnetic reconnection diffusion region: single-event-based statistics. *Earth, Planets and Space*, 66(1):161, 2014.

[50] L Andersson, RE Ergun, J Tao, A Roux, O LeContel, V Angelopoulos, J Bonnell, JP McFadden, DE Larson, S Eriksson, et al. New features of electron phase space holes observed by the themis mission. *Physical Review Letters*, 102(22):225004, 2009.

[51] DM Malaspina, L Andersson, RE Ergun, JR Wygant, JW Bonnell, C Kletzing, Geoffrey D Reeves, Ruth M Skoug, and Brian Arthur Larsen. Nonlinear electric field structures in the inner magnetosphere. *Geophysical Research Letters*, 41(16):5693–5701, 2014.

[52] V. L. Krasovsky, H. Matsumoto, and Y. Omura. Effect of trapped-particle deficit and structure of localized electrostatic perturbations of different dimensionality. *Journal of Geophysical Research: Space Physics*, 109(A4):1–9, 2004.

[53] L. Muschietti, I. Roth, C. W. Carlson, and R. E. Ergun. Transverse instability of magnetized electron holes. *Physical Review Letters*, 85(1):94–97, 2000.

[54] QM Lu, Bertrand Lembège, JB Tao, and S Wang. Perpendicular electric field in two-dimensional electron phase-holes: A parameter study. *Journal of Geophysical Research: Space Physics*, 113(A11), 2008.

[55] Mingyu Wu, Quanming Lu, Can Huang, and Shui Wang. Transverse instability and perpendicular electric field in two-dimensional electron phase-space holes. *Journal of Geophysical Research: Space Physics*, 115(A10), 2010.

[56] David L Newman, Martin V Goldman, M Spector, and F Perez. Dynamics and

Instability of Electron Phase-Space Tubes. *Physical Review Letters*, 86(7):1239–1242, 2001.

[57] Christian Bernt Haakonsen, Ian H. Hutchinson, and Chuteng Zhou. Kinetic electron and ion instability of the lunar wake simulated at physical mass ratio. *Physics of Plasmas*, 22(3), 2015.

[58] I. H. Hutchinson. Electron velocity distribution instability in magnetized plasma wakes and artificial electron mass. *Journal of Geophysical Research: Space Physics*, 117(A3), 2012.

[59] Ronald Davidson. *Methods in nonlinear plasma theory*. Academic Press, 1972.

[60] J Douglas Wright. Corrections to the KdV approximation for water waves. *SIAM Journal on Mathematical Analysis*, 37(4):1161–1206, 2005.

[61] Bertrand Kibler, Julien Fatome, Christophe Finot, Guy Millot, Frédéric Dias, Goëry Genty, Nail Akhmediev, and John M Dudley. The Peregrine soliton in nonlinear fibre optics. *Nature Physics*, 6(10):790–795, 2010.

[62] Diederik Johannes Korteweg and Gustav De Vries. On the change of form of long waves advancing in a rectangular canal, and on a new type of long stationary waves. *The London, Edinburgh, and Dublin Philosophical Magazine and Journal of Science*, 39(240):422–443, 1895.

[63] Norman J Zabusky and Martin D Kruskal. Interaction of "solitons" in a collisionless plasma and the recurrence of initial states. *Physical Review Letters*, 15(6):240, 1965.

[64] Clifford S Gardner, John M Greene, Martin D Kruskal, and Robert M Miura. Method for solving the Korteweg-de Vries equation. *Physical Review Letters*, 19(19):1095, 1967.

[65] L Faddeev. Instructive history of the quantum inverse scattering method. In *Fifty Years of Mathematical Physics: Selected Works of Ludwig Faddeev*, pages 354–369. World Scientific, 2016.

[66] Michael D Montgomery, JR Asbridge, and SJ Bame. Vela 4 plasma observations near the Earth's bow shock. *Journal of Geophysical Research*, 75(7):1217–1231, 1970.

[67] Hans Schamel. A modified Korteweg-de Vries equation for ion acoustic waves due to resonant electrons. *Journal of Plasma Physics*, 9:377–387, 1973.

[68] J P Lynov, P Michelsen, H L Pécseli, J Juul Rasmussen, and S H Sørensen. Phase-Space Models of Solitary Electron Holes. *Physica Scripta*, 31(6):596–605, 1985.

[69] Koichi Saeki and J Juul Rasmussen. Stationary solution of coupled electron hole and ion soliton in a collisionless plasma. *Journal of the Physical Society of Japan*, 60(3):735–738, 1991.

[70] T. H. Dupree. Growth of phase-space density holes. *Physics of Fluids*, 26(9):2460, 1983.

[71] H Ralph Lewis and Keith R Symon. Linearized analysis of inhomogeneous plasma equilibria: General theory. *Journal of Mathematical Physics*, 20:413–436, 1979.

[72] H. Schamel. Stability of Electron Vortex Structures in Phase Space. *Physical Review Letters*, 48(7):481–483, 1981.

[73] D. Jovanović and H. Schamel. The stability of propagating slab electron holes in a magnetized plasma. *Physics of Plasmas*, 9:5079–5087, December 2002.

[74] B. Eliasson and P. K. Shukla. Dynamics of electron holes in an electron-oxygen-ion plasma. *Physical Review Letters*, 93(4):045001, 2004.

[75] Koichi Saeki and Hitoshi Genma. Electron-Hole Disruption due to Ion Motion and Formation of Coupled Electron Hole and Ion-Acoustic Soliton in a Plasma. *Physical Review Letters*, 80(6):1224–1227, 1998.

[76] Lars P. Dyrud and Meers M. Oppenheim. Electron holes, ion waves, and anomalous resistivity in space plasmas. *Journal of Geophysical Research: Space Physics*, 111(1):1–12, 2006.

[77] M Lesur, P H Diamond, and Y Kosuga. Nonlinear current-driven ion-acoustic instability driven by phase-space structures. *Plasma Physics and Controlled Fusion*, 56(7):075005, jul 2014.

[78] S M Hosseini Jenab and F Spanier. Simulation study of overtaking of ion-acoustic solitons in the fully kinetic regime. *Physics of Plasmas*, 032305, 2017.

[79] Amar Kakad, Bharati Kakad, and Yoshiharu Omura. Formation and interaction of multiple coherent phase space structures in plasma. *Physics of Plasmas*, 24(6):060704, 2017.

[80] I. H. Hutchinson and C. Zhou. Plasma electron hole kinematics . I . Momentum conservation. *Physics of Plasmas*, 23(8):082101, 2016.

[81] C. Zhou and I. H. Hutchinson. Plasma electron hole kinematics. II. Hole tracking Particle-In-Cell simulation. *Physics of Plasmas*, 23(8):082102, 2016.

[82] Chuteng Zhou and Ian H. Hutchinson. Plasma electron hole oscillatory velocity instability. *Journal of Plasma Physics*, 83(5), 2017.

[83] Stephen Butterworth. On the theory of filter amplifiers. *Wireless Engineer*, 7(6):536–541, 1930.

[84] James E. Gentle. *Random Number Generation and Monte Carlo Methods*. Springer, NY, second edition, 2003.

[85] O Buneman. Instability, Turbulence, and Conductivity in Current-Carrying Plasma. *Physical Review Letters*, 1(1):8–9, 1958.

[86] T E Stringer. Electrostatic instabilities in current-carrying and counterstreaming plasmas. *Journal of Nuclear Energy. Part C, Plasma Physics, Accelerators, Thermonuclear Research*, 6(3):267–279, 1964.

[87] B. D. Fried and S. D. Conte. *The Plasma Dispersion Function*. New York: Academic Press, 1961.

[88] K Saeki, P. Michelsen, H. L. Pécseli, and J. Juul Rasmussen. Formation and Coalescence of Electron Solitary Holes. *Physical Review Letters*, 42(8):501–504, 1979.

[89] H. L. Berk. Phase Space Hydrodynamics of Equivalent Nonlinear Systems: Experimental and Computational Observations. *Physics of Fluids*, 13(4):980, 1970.

[90] J P Lynov, P Michelsen, H L Pecseli, and J. Juul Rasmussen. Interaction between electron holes in a strongly magnetized plasma. *Physical Letters A*, 80(1):10–12, 1980.

[91] Yu V. Khotyaintsev, A. Vaivads, M. André, M. Fujimoto, A. Retinò, and C. J. Owen. Observations of slow electron holes at a magnetic reconnection site. *Physical Review Letters*, 105(16):165002, 2010.

[92] C. Norgren, M. André, D. B. Graham, Yu V. Khotyaintsev, and A. Vaivads. Slow electron holes in multicomponent plasmas. *Geophysical Research Letters*, 42(18):7264–7272, 2015.

[93] Hans Schamel and V. I. Karpman. Evolution of Langmuir soliton caused by resonant emission of ion sound wave. *Physics of Plasmas*, 3487:10–13, 1998.

[94] A Luque and H Schamel. Electrostatic trapping as a key to the dynamics of plasmas, fluids and other collective systems. *Physics Reports*, 415(5-6):261–359, aug 2005.

[95] Kyunghwan Dokgo, Minho Woo, Cheong-rim Choi, Kyoung-wook Min, and Junga Hwang. Generation of coherent ion acoustic solitary waves in inhomogeneous plasmas by an odd eigenmode of electron holes. *Physics of Plasmas*, 092107, 2016.

[96] H-G Purwins, HU Bödeker, and AW Liehr. Dissipative solitons in reaction-diffusion systems. In *Dissipative solitons*, pages 267–308. Springer, 2005.

[97] H. Nyquist. Regeneration theory. *The Bell System Technical Journal*, 11(1):126–147, Jan 1932.

[98] Yitzhak Katznelson. *An Introduction to Harmonic Analysis*. Cambridge University Press, 3rd edition, 2002.

[99] D B Graham, Yu V Khotyaintsev, A Vaivads, and M André. Electrostatic solitary waves and electrostatic waves at the magnetopause. *Journal of Geophysical Research: Space Physics*, pages 3069–3092, 2016.

[100] Amar Kakad, Bharati Kakad, Chandrasekhar Anekallu, Gurbax Lakhina, and Yoshiharu Omura. Slow electrostatic solitary waves in Earth's plasma sheet boundary layer. *Journal of Geophysical Research : Space Physics*, 121(May):4452–4465, 2016.

[101] H Che, JF Drake, M Swisdak, and PH Yoon. Electron holes and heating in the reconnection dissipation region. *Geophysical Research Letters*, 37(11), 2010.

[102] VL Krasovsky, H Matsumoto, and Y Omura. Electrostatic solitary waves as collective charges in a magnetospheric plasma: Physical structure and properties of Bernstein–Greene–Kruskal (BGK) solitons. *Journal of Geophysical Research: Space Physics*, 108(A3), 2003.

[103] C Eugene Wayne and J Douglas Wright. Higher order modulation equations for a Boussinesq equation. *SIAM Journal on Applied Dynamical Systems*, 1(2):271–302, 2002.

[104] Ch Josserand and M Rossi. The merging of two co-rotating vortices: a numerical study. *European Journal of Mechanics-B/Fluids*, 26(6):779–794, 2007.

[105] P Goldreich and S Sridhar. Toward a theory of interstellar turbulence. II: Strong Alfvénic turbulence. *The Astrophysical Journal*, 438:763–775, 1995.

[106] Yoshifumi Saitou and Yoshiharu Nakamura. Ion-acoustic soliton-like waves undergoing Landau damping. *Physics Letters A*, 343(5):397–402, 2005.

[107] I. H. Hutchinson, C. B. Haakonsen, and C. Zhou. Non-linear plasma wake growth of electron holes. *Physics of Plasmas*, 22(3), 2015.